

PRETARGETED CANCER RADIOIMMUNOTHERAPY AND RADIOIMAGING  
USING ANTIBODIES AND ANTIBODY FRAGMENTS

---

A Dissertation

Presented to

The Faculty of the Graduate School

At the University of Missouri

---

In Partial Fulfillment

of the Requirements for the Degree

Doctor of Philosophy

---

By

MANANKUMAR SHAH

Dr. Thomas P. Quinn, Dissertation Supervisor

December 2018

The undersigned, appointed by the dean of the Graduate School,  
have examined the dissertation entitled

PRETARGETED CANCER RADIOIMMUNOTHERAPY AND RADIOIMAGING  
USING ANTIBODIES AND ANTIBODY FRAGMENTS

Presented by Manankumar Shah

A candidate for the degree of

Doctor of Philosophy in Biochemistry

And hereby certify that, in their opinion, it is worthy of acceptance.

---

Dr. Thomas P. Quinn

---

Dr. Susan Deutscher

---

Dr. George Smith

---

Dr. Silvia Jurisson

---

Dr. Frank Schmidt

## ACKNOWLEDGMENTS

First and foremost, I would like to convey my deepest gratitude to my research advisor Dr. Thomas Quinn. I am immensely thankful for his guidance, support, and mentorship. Tom has been instrumental in my development as a scientist, and I would not be where I am today without him. I cannot thank him enough for the constant encouragement and his willingness to allow me to pursue scientific projects of my interests. Tom has been extremely patient with me throughout the course of my study and at the same time pushed me just enough and on the right moments to keep me on track, and for that I will be forever grateful. I would also like to thank my committee members Dr. Susan Deutscher, Dr. George Smith, Dr. Silvia Jurisson, and Dr. Frank Schmidt for providing valuable feedbacks and direction for my research. I would like to especially thank Dr. Susan Deutscher for all of her guidance and encouragement for last five and half years.

I would like to thank and dedicate this dissertation to my parents, Anilkumar and Darshnaben Shah. They have been incredible role models and have instilled me with great life lessons to make me a better person. Throughout my whole life, they have been incredibly supportive and have encouraged me to chase my dreams. No amount of words can express how indebted I am to them. I am also thankful to my brother, Zubin Shah, who has always given me his honest opinions on everything in life and has inspired me to work hard with dedication and passion. I would like to say a big thank you to my cousin Parag Shah and my

sister in-law Arpita Shah. They are the bedrock of my life away from India. I cannot imagine my life in the United States without their love and support.

I would like to thank everyone in the lab as well. Xiuli has played an integral role in my training in radiochemistry, while Marie has provided invaluable help with tissue culture and other day to day lab activities. I have to give a shout out to Austin Prater. Austin has been a great company in the lab to share the highs and the lows of the graduate school. I will miss our conversations on sports, politics, and pretty much on any topic! Last but not least, I am extremely thankful to my fellow graduate students Ryan Harvey, Dr. Widler Casey, Dr. Megan Sheridan, Dr. Erica LaMontagne, and Emily Armbruster. Thank you for being an awesome bunch of friends. I will always cherish the memories we shared including group lunches, study sessions and even studying for 20 questions! I am glad I got to share my graduate school experience with you all.

# TABLE OF CONTENTS

<b>ACKNOWLEDGEMENTS</b> .....	ii
<b>LIST OF TABLES</b> .....	vi
<b>LIST OF FIGURES</b> .....	vii
<b>LIST OF ABBREVIATIONS</b> .....	ix
<b>ABSTRACT</b> .....	xi

## Chapter 1

<b>Introduction</b> .....	1
Molecular Imaging .....	2
Pretargeting .....	5
Alpha Particle Based Therapy .....	9
Single-Chain Antibody Fragments (scFvs).....	12
Phage Display of Antibodies .....	15
Matrix Metalloproteinases (MMPs) .....	21

## Chapter 2

<b>Metal-Free      Cycloaddition      Chemistry      Driven      Pretargeted</b>	
<b>Radioimmunotherapy Using <math>\alpha</math>-Particle Radiation</b> .....	23
Introduction .....	24
Materials and Methods.....	29
Results.....	36
Discussion .....	50

Conclusions .....	54
<b>Chapter 3</b>	
<b>MMP-12 As a Novel Tumor Target for PET/CT Imaging Using Phage Display Derived Antibody Fragments and Ultrasmall Silica Nanoparticles .....</b>	<b>55</b>
Introduction .....	56
Materials and Methods.....	61
Results.....	71
Discussion .....	88
Conclusions .....	94
Future Studies .....	95
<b>Chapter 4</b>	
<b>Phage Display Selection of Single-Chain Antibody Fragments Against Thomsen-Friedenreich Antigen (TF-Antigen) .....</b>	<b>96</b>
Introduction.....	97
Materials and Methods .....	100
Results .....	106
Discussion .....	118
<b>References .....</b>	<b>122</b>
<b>VITA .....</b>	<b>151</b>

## LIST OF TABLES

<b>Table</b>		<b>Page</b>
<b>Chapter 2</b>		
Table 2.1	Biodistribution of $^{212}\text{Pb}$ -DOTA-Tz and $^{212}\text{Pb}$ -TCMC-Tz in LS174T tumor bearing nude mice pretargeted with CC49-TCO mAb.....	40
Table 2.2	Absorbed radiation doses from $^{212}\text{Pb}$ -DOTA-Tz and $^{212}\text{Pb}$ -TCMC-Tz in mice bearing LS174T colon carcinoma tumors .....	42
<b>Chapter 3</b>		
Table 3.1	Sequence analysis of MMP-12 specific antibody fragments .....	74
<b>Chapter 4</b>		
Table 4.1	Stability of $^{99\text{m}}\text{Tc}$ -labeled 9C-scFv .....	115

## LIST OF FIGURES

Chapter	Page
<b>Chapter 1</b>	
Figure 1.1 Schematics of full length IgG monoclonal antibody and single-chain fragment (scFv).....	16
Figure 1.2 Schematic of phage display selection process.....	20
Figure 1.3 Principle of trypsin based elution.....	22
<b>Chapter 2</b>	
Figure 2.1 Structures of pretargeting reagents used in the study. A) TCO-NHS, B) DOTA-PEG <sub>10</sub> -Tetrazine and, C) TCMC-Bn-SCN-PEG <sub>10</sub> -Tetrazine, and D) Galactose-albumin-Tetrazine based clearing agent.....	35
Figure 2.2 Pharmacokinetics of <sup>212</sup> Pb-labeled tetrazines (without the pretargeted mAb) in mice bearing LS174T human colon carcinoma xenograft.....	46
Figure 2.3 Schematic of the pretargeting protocol used in this study.....	48
Figure 2.4 Plots of average tumor volumes and average body weights of each group of mice during first 21 days of the PRIT studies.....	54
Figure 2.5 Kaplan-Meier survival curves.....	56
Figure 2.6 The effects of radiation-induced toxicity on white blood cell counts, and platelet counts.....	57
Figure 2.7 Kidney histology sections from untreated mice (PBS), and pretargeted mice treated with 200 μCi, and 75 μCi of <sup>212</sup> Pb-DOTA-Tz. ...	58

### **Chapter 3**

Figure 3.1	Phage ELISA.....	73
Figure 3.2	Expression vectors.....	76
Figure 3.3	Expression and Purification of H-12 scFv .....	77
Figure 3.4	Soluble scFv ELISA .....	79
Figure 3.5	Binding affinity of H12 scFv towards MMP-12 protein was determined by microscale thermophoresis (MST).....	80
Figure 3.6	Flow cytometric analysis of H12-scFv .....	81
Figure 3.7	Fluorescence microscopy analysis of cell binding.....	83
Figure 3.8	A schematic of the Cornell prime (C' dot) nanoparticles .....	84
Figure 3.9	In vivo SPECT/CT imaging .....	87
Figure 3.10	In vivo PET/CT imaging .....	88

### **Chapter 4**

Figure 4.1	Phage ELISA .....	107
Figure 4.2	Expression and purification of 9C-scFv.....	109
Figure 4.3	Soluble scFv ELISA .....	110
Figure 4.4	Binding affinity determination of the TF-specific 9C-scFv .....	111
Figure 4.5	Flow cytometry analysis of 9C-scFv .....	114
Figure 4.6	In vitro cell binding assay .....	115
Figure 4.7	In vivo SPECT/CT imaging .....	117

## LIST OF ABBREVIATIONS

%ID/g: Percent injected dose/gram

BSA: Bovine serum albumin

EDTA: Ethylenediaminetetraacetic acid

C' dot: Cornell prime ultrasmall silica nanoparticles

CDR: Complementarity Determining Regions

DBCO: Dibenzocyclooctyne

DOF: Desferoxamine

DOTA: 1,4,7,10-tetraazacyclododecane-1,4,7,10-tetraacetic acid

ECM: Extra Cellular Matrix

EDTA: Ethylenediaminetetraacetic acid

ELISA: Enzyme-linked immunosorbent assay

IEDDA: Inverse Electron Demand Diels-Alder

ITLC: Instant Thin Layer Chromatography

mAb: Monoclonal Antibody

MFI: Mean Fluorescence Intensity

MMP: Matrix Metalloproteinases

MST: Microscale thermophoresis

NOTA: 1,4,7-triazacyclononane-1,4,7-triacetic acid

PBS: Phosphate Buffer Solution

PET: Positron Emission Tomography

PRIT: Pretargeted Radioimmunotherapy

RIT: Radioimmunotherapy

scFv: Single-chain variable antibody fragment

SDS-PAGE: Sodium dodecyl sulfate polyacrylamide gel electrophoresis

SPECT: Single-Photon Emission Computed Tomography

T/NT: Tumor-to-Non-tumor ratio

TBS: Tris buffer saline

TBST: Tris buffer saline with tween-20

TCMC: 1,4,7,10-tetra-(2-carbamonyl methyl)-cyclododecane

TCO: trans-cyclooctene

TF: Thomsen-Friedenreich

Tz: Tetrazine

VH: Variable Heavy chain

VL: Variable Light chain

**PRETARGETED CANCER RADIOIMMUNOTHERAPY AND  
RADIOIMAGING USING ANTIBODIES AND ANTIBODY  
FRAGMENTS**

By: Manankumar Shah

Dr. Thomas P. Quinn, Dissertation Advisor

**ABSTRACT**

Over the last few decades, antibodies have become the mainstay of cancer diagnosis and therapeutics. In traditional radioimmunotherapy (RIT), tumor targeting antibodies are directly conjugated with radioisotopes and depending on the radionuclides's properties, the direct labeled antibodies can be used for diagnostic or therapeutic purposes. However, one of the major challenges of using radiolabeled antibodies for therapy is their long serum half-lives. It generally takes 5-7 days for antibodies to achieve maximum tumor binding. This slow blood clearance results in high normal tissue irradiation and a poor therapeutic index. This is exemplified by the fact that to date, only two radiolabeled antibodies have been approved by the FDA for radioimmunotherapy

of cancer. In order to overcome this obstacle, several pretargeting strategies have been developed and investigated. The pretargeted radioimmunotherapy approach (PRIT) decouples the administration of tumor targeting monoclonal antibodies (mAbs) from that of the radiolabeled ligand. This multi-step strategy allows delivery of high doses of radiation to tumor cells while minimizing non-specific normal tissue irradiation. In this study, we evaluated the potential of pretargeted  $\alpha$ -particle radioimmunotherapy based on inverse electron demand Diels-Alder reaction (IEDDA) between *trans*-cyclooctene (TCO) and tetrazine (Tz). Two tetrazine based chelators, DOTA-Tz and TCMC-Tz, were synthesized and compared for their radiolabeling efficiency with  $^{212}\text{Pb}$ , radiochemical stability and in vivo pharmacokinetics. Dosimetry was determined from pretargeted biodistribution studies. The PRIT study was carried out in LS174T tumor bearing mice pretargeted with CC49-TCO mAbs. After removing unbound mAbs from the blood using two doses of clearing agent, mice were treated with various doses of (0, 75, 125, 200, and 2 x 75  $\mu\text{Ci}$ ) of  $^{212}\text{Pb}$ -DOTA-Tz.  $^{212}\text{Pb}$ -DOTA-Tz displayed better in vivo biodistribution than  $^{212}\text{Pb}$ -TCMC-Tz and was selected for PRIT study. All the mouse groups receiving treatment displayed dose dependent reduction in tumor size, while the control groups showed exponential tumor growth. Groups receiving 200  $\mu\text{Ci}$  of  $^{212}\text{Pb}$ -DOTA-Tz and 15  $\mu\text{Ci}$  of direct labeled CC49 exhibited acute radiation associated toxicity. Treatment with 75, 125, and 2 x 75  $\mu\text{Ci}$  of  $^{212}\text{Pb}$ -DOTA-Tz resulted in statistically significant improvement in median survival (26, 35 and 39 days respectively). This study successfully demonstrated that pretargeted  $^{212}\text{Pb}$   $\alpha$ -particle therapy resulted in reduced tumor

growth rates and improved survival with minimal normal tissue toxicity, as detailed in Chapter 2.

Lung cancer is the leading cause of the cancer related deaths in the United States and world-wide. In 2018, it is estimated that about 234,030 new patients will be diagnosed and 154,050 will die of lung cancer in the United States. Once the cancer is metastasized, the 5-year survival rate is reduced to less than 5%. Matrix metalloproteinase-12 (MMP-12) is a member of family of zinc dependent endopeptidase enzymes that are involved in extracellular matrix (ECM) remodeling. MMP-12 is generally expressed by macrophages and is associated with degradation of elastin in ECM. A growing body of evidence suggests that MMP-12 plays a key role in lung cancer proliferation and metastasis. Single-chain antibody fragments (scFv) were selected against MMP-12 using phage display methodology to develop target vectors for lung cancer radioimaging. The McCafferty scFv library was screened to isolate MMP-12 specific antibodies. Two rounds of selection against purified MMP-12 resulted in 8 unique scFv clones which showed MMP-12 specific binding. The selected clones were successfully expressed in E.coli and their binding to MMP-12 was confirmed by ELISA assay. Flow-cytometry and fluorescence microscopy demonstrated the specific binding of the selected scFv clone to the MMP-12 on human lung adenocarcinoma cells A549. The selected scFv was conjugated with ultrasmall silica nanoparticles and the resulting nano-conjugate was radiolabeled with  $^{89}\text{Zr}$ . The  $^{89}\text{Zr}$ -labeled scFv-nanoparticles were injected in mice bearing A549 tumors for in vivo PET/CT imaging. The whole-body images revealed a tumor

specific uptake of  $^{89}\text{Zr}$ -labeled scFv-nanoparticles with minimum non-target accumulation. The data from this study clearly demonstrated the potential of MMP-12 as a novel diagnostic marker for lung adenocarcinoma and that MMP-12 specific scFv-nanoparticle conjugates can be used for non-invasive in vivo imaging. This project is detailed in Chapter 3.

Thomsen-Friedenreich (TF) is a disaccharide (Galactose  $\beta$ 1-3 N-acetylgalactosamine) antigen, which is present on about ~90% of carcinomas. The TF expression on the tumor cell is correlated with poor prognosis and tumor propagation. TF antigen is also involved in cell to cell adhesion and metastasis, making it a very good target for cancer imaging and therapy. Using phage display technology, TF binding scFv fragments were selected from the McCafferty antibody library. The selected scFv clones were characterized in vitro for their TF specificity and cell binding properties by ELISA and flow-cytometry assay. The selected TF specific clone (9C-scFv) was radiolabeled with  $^{99\text{m}}\text{Tc}$  by directly conjugating  $^{99\text{m}}\text{Tc}$  to the C-terminal 6x His-tag. The  $^{99\text{m}}\text{Tc}$ -labeled 9C-scFv was injected in mice bearing MDA-MB-231 human breast cancer xenografts. The SPECT/CT images, acquired 4 hours post injection, revealed a moderate tumor uptake of radiolabeled scFvs with significant accumulation in the liver and kidneys. The phage display derived single-chain scFv fragments against the TF antigen demonstrated potential for development as an imaging agent but requires more work to achieve favorable pharmacokinetics.

# **CHAPTER 1**

## **INTRODUCTION**

## Molecular Imaging

Molecular imaging not only provides means for non-invasive cancer diagnosis and staging but also plays an important role for treatment planning, treatment response assessment, surgical management, and post treatment evaluation for cancer relapse.(1) Traditionally, physicians have relied upon the classical imaging modalities like X-ray tests, computed topography (CT) scans, ultrasound, and magnetic resonance imaging (MRI). Even though these techniques are the backbone of current diagnostic medicine, they are largely restricted to providing anatomical and physiological information.(2) With the advent of the personalized medicine, there is a growing need to analyze specific targets and biomarkers in vivo. Nuclear imaging methodologies like single-photon emission computed tomography (SPECT) and positron emission tomography (PET) allow detection and functional evaluation of specific targets via the use of radioactive probes. Tumor targeting vectors such as various antibody forms, peptides, and nanoparticles can be conjugated with radioisotopes to provide a powerful tool for imaging specific targets with nanomolar or picomolar affinities.(3,4)

SPECT imaging involves radiolabeling tissue targeting constructs with radionuclides that emit  $\gamma$ -rays. Some of the commonly used SPECT radionuclides include  $^{99m}\text{Tc}$  ( $t_{1/2}=6\text{h}$ ),  $^{67}\text{Ga}$  ( $t_{1/2}=78.3\text{h}$ ),  $^{111}\text{In}$  ( $t_{1/2}=67\text{h}$ ), and  $^{203}\text{Pb}$  ( $t_{1/2}=52\text{h}$ ).(5)  $^{99m}\text{Tc}$  is one of the most widely available and least expensive radioisotopes for SPECT imaging.  $^{99m}\text{Tc}$ -labeled radioimaging agents are thus

the mainstay of nuclear imaging worldwide.(6,7) SPECT has traditionally been regarded as a nonquantitative imaging method. However, advancements in detector cameras, algorithms for image reconstructions, and sophisticated compensation techniques have now made SPECT viable for quantitative imaging.(8)

PET imaging involves the use of positron emitting radionuclides. Positrons emitted from decaying radionuclides collide with electrons in nearby tissue resulting in annihilation and emission of two 511 keV photons oriented at 180 degree from each other. Detectors, arranged in a ring configuration detect the emitted photons and the data are reconstructed into a whole-body image to map the distribution and concentration of the radionuclide in the body.(9) Typical clinical PET scanners have roughly 10-fold greater sensitivity than the SPECT instruments, facilitating the detection of radiotracers at picomolar concentrations. Because of the advances in genomic and proteomic sciences, several new cancer biomarkers were discovered in the last decade. This coupled with more availability of radionuclides and a myriad of different conjugation and chelation strategies have fueled the interest in PET imaging. Positron emitting radiometals such as  $^{18}\text{F}$  ( $t_{1/2} = 1.8 \text{ h}$ ),  $^{64}\text{Cu}$  ( $t_{1/2}=12.7 \text{ h}$ ),  $^{68}\text{Ga}$  ( $t_{1/2}=1.1 \text{ h}$ ),  $^{86}\text{Y}$  ( $t_{1/2}=14.7 \text{ h}$ ), and  $^{89}\text{Zr}$  ( $t_{1/2}=78.4 \text{ h}$ ) are increasingly used for PET imaging due to favorable half-lives and the availability of a number of metal chelators and prosthetic groups.(10-12)

Intact antibodies have long been used for targeted therapeutics due to their specificities and target affinities. However, their long serum half-lives and

poor biodistribution profiles hamper their use as imaging agents.(13) Many of these issues can be overcome by the use of smaller tumor targeting vectors such as peptides, and various antibody fragments like single-chain variable fragments (scFvs), Fab domains, and nanobodies. These constructs display improved pharmacokinetic properties such as better tissue penetration and rapid blood clearance without compromising binding specificities. This allows the imaging studies to be performed on the same day after injection of radiolabeled scFv rather than waiting for 1-3 days in the case of an intact antibody.(14,15) The choice of PET and SPECT imaging can be made based upon the availability of radionuclide, cost, half-life of the isotope and the intended use. Typically, the decay half-life of the radioisotope is matched with the serum half-life of the targeting agent. Both imaging methods provide several options for non-invasive ways for cancer detection and characterization.

## Pretargeting

The success of any cancer diagnostic or therapeutic strategy relies upon the selective uptake of the targeting agent in the tumor. Because of their high binding affinities and specificities, monoclonal antibodies have long been used as targeting vehicles for delivering radionuclides for imaging as well as therapeutic applications. Even though radiolabeled antibodies have been investigated since 1950, to date only  $^{90}\text{Y}$ -labeled ibritumomab and  $^{131}\text{I}$ -labeled tositumomab have been approved by the FDA for non-Hodgkin's lymphoma therapy.(16,17) The major hindrance in the success of the radioimmunotherapy (RIT) is the poor pharmacokinetics of the full length monoclonal antibodies (mAbs). Because of their larger size (150 kDa), mAbs have a long serum half-life and it may take 5-7 days for antibodies to achieve maximum tumor accumulation. The prolonged circulation of radiolabeled antibodies leads to high tumor accumulation, however at the cost of excessive normal tissue irradiation. This is especially detrimental in radioimmunotherapy as it significantly limits the amount of dose administered and reduces the therapeutic effectiveness. To overcome the drawbacks of conventional RIT, several pretargeted radioimmunotherapy (PRIT) strategies have been developed and investigated.(18)

Pretargeting strategies generally involve three steps: 1) Administration of highly tumor specific antibodies and their accumulation at the target site, 2) Following maximum tumor uptake, freely circulating antibodies are removed from the blood using a clearing agent, 3) After sufficient time, a fast clearing radiolabeled species is injected which has high specificity and affinity towards

tumor bound antibodies.(19) Because of their small size, any unbound radiolabeled effector molecules are rapidly excreted out of body via the kidneys. As a result, high tumor-to-nontumor (T/NT) ratios can be achieved resulting in an improved therapeutic index compared to the conventional RIT. Some of the earlier classes of pretargeting strategies include biotin/avidin systems, bispecific antibodies, and complementary oligonucleotides. Even though these approaches displayed some promise, they have had limited success due to several disadvantages like immunogenicity, slow reaction rates, and low binding constants. Over the past decade, a new class of biorthogonal click-chemistry reactions has been increasingly investigated and has shown great promise in cancer radioimaging and radiotherapy.(20)

According to Bertozzi *et al.*, for a chemical reaction to be termed as biorthogonal, it must be very selective, high yielding, have very fast reaction kinetics, have biologically inert components, and produce non-toxic byproducts.(21) Cu(I)-catalyzed azide-alkyne click chemistry (CuAAC) is one of the most prominent examples of biorthogonal reactions. It is an extremely efficient reaction between azide and alkyne functionalized molecules forming a stable conjugate via a triazole moiety. Over the years, a number of imaging probes have been designed and investigated for in vivo radioimaging using this strategy.(22-24) However, the necessity of cytotoxic copper as a catalyst for the CuAAC reaction would severely limit its application in a clinical setting. As a result, metal-free click-chemistry reactions have attracted significant interest in

recent times for radioimaging as well as therapeutic applications in living systems.

The Staudinger ligation is one of the earliest metal-free click chemistry reactions investigated.(25) It involves a highly selective reaction between azide and phosphine groups resulting in formation of an amide bond. In 2011, Van Dongen and co-workers functionalized an anti-CD44v6 mAbs with azide groups and synthesized phosphine containing small radiolabeled effector moieties for in vivo tumor radioimaging. Unfortunately, there was no in vivo Staudinger reaction detected. It was mainly because of slow reaction rates ( $k_2 = 2 \times 10^{-3} \text{ M}^{-1}\text{s}^{-1}$ ) as well as oxidation of the phosphine group which made it unreactive.(26)

Strain promoted alkyne-azide cycloaddition (SPAAC) represents another class of copper-free biorthogonal reactions. It relies upon the use of strained cyclooctyne and azide moieties and can achieve up to 3 orders of magnitude faster reaction kinetics ( $k_2 = 0.31 \text{ M}^{-1}\text{s}^{-1}$ ). (27) In 2013, Lee *et al.* successfully displayed the potential of SPACC reaction for in vivo tumor PET imaging using cyclooctyne modified nanoparticles and  $^{18}\text{F}$ -labeled azide ligands.(28) Even though SPAAC has much faster reaction kinetics, it is still not fast enough to be used in low enough concentrations typically used in in vivo applications.

The discovery of the inverse electron-demand Diels-Alder cycloaddition (IEDDA) reaction between *trans*-cyclooctene (TCO) and tetrazine (Tz) by Fox and coworkers was the turning point in terms of in vivo application of biorthogonal reactions. This is a highly specific and rapid reaction with reaction rates of up to

$2.5 \times 10^5 \text{ M}^{-1}\text{s}^{-1}$ .(27,29) In their landmark study in 2010, Rossin *et al.* demonstrated for the first time, the application of IEDDA-based click-chemistry approach for SPECT imaging in a mouse tumor model.(30) In this study, mice bearing LS174T xenografts were pretargeted with TCO modified CC49 mAbs.  $^{111}\text{In}$ -DOTA labeled tetrazine was injected 24 hours after the CC49-TCO mAb administration for SPECT imaging. Following a similar approach, Lewis and Zegils developed PET imaging strategies using  $^{64}\text{Cu}$ -labeled tetrazine species.(31) Since then, there have been numerous IEDDA-based studies that have been conducted using various tumor targeting vectors such as diabodies, affibodies, and nanoparticles. The application of TCO-tetrazine based click-chemistry is not only limited to imaging studies. Recently, Houghton *et al.* demonstrated the feasibility of pretargeted radioimmunotherapy (PRTI) using TCO conjugated antibodies and  $^{177}\text{Lu}$ -DOTA labeled tetrazine.(32)

## Alpha Particle Based Therapy

Nuclear decay occurs as a result of spontaneous disintegration of atomic nuclei resulting in more stable nuclei. The three major types of radiation include alpha particles, beta particles, and gamma rays. All of these radiations differ in their physical characteristics and thus in their intended use.(33) Alpha radiation is made up of charged particles composed of two protons and two neutrons. They are essentially  $^4\text{He}$  nucleus with +2 net charge. Alpha emission usually occurs in elements of high atomic number ( $Z > 82$ ) and is an example of ionizing radiation. The emitted alpha particle, due to its mass and energy, can knock an orbital electron from the interacting atom creating a positively charged ion. This pair of negatively charged electrons and positively charged ions can then go on to cause further ionization reactions in their paths. Alpha particles move relatively slowly and deposit large amounts of energy per unit path length (100 keV/ $\mu\text{m}$ ). Alpha particles offer several advantages over beta particles and gamma radiation for use in targeted radiotherapy. First, alpha particles have a very short tissue path length of around 50-100  $\mu\text{m}$ . When combined with its high linear energy transfer (LET), they can deposit a therapeutic dose in a highly localized manner with negligible damage to normal tissue. They induce double stranded DNA damage which is irreparable and produce nucleotide modifications that cause apoptosis, cell cycle-arrest and autophagy. Moreover, these cytotoxic damages are independent of the tissue oxygen level and can thus be effective in a hypoxic tumor microenvironment.(34) These properties make alpha particles an attractive

choice for the use in radioimmunotherapy, especially in the treatment of micrometastatic and disseminated tumors.

The fundamental goal of any cancer radioimmunotherapy is to deliver a cytotoxic radiation dose to the tumor with minimum irradiation to the surrounding healthy tissue. Alpha particle based therapy offers a decisive advantage towards this goal due to its intense ionizing track over a very short path length in tissues. Several alpha emitting radioisotopes have been investigated over the years for their potential therapeutic application. These include  $^{211}\text{At}$ ,  $^{212}\text{Bi}$ ,  $^{213}\text{Bi}$ ,  $^{225}\text{Ac}$ ,  $^{212}\text{Pb}$ ,  $^{227}\text{Th}$ , and  $^{223}\text{Ra}$ .(35) Pretargeted radioimmunotherapy (PRIT) described in Chapter 2 of this dissertation was carried out using  $^{212}\text{Pb}$ . It is important to note here that  $^{212}\text{Pb}$  is not an alpha emitter but decays to  $^{212}\text{Bi}$ , which actually emits alpha particles. The short half-life of  $^{212}\text{Bi}$  ( $t_{1/2} = 60$  min) presents a challenge in dose preparation and delivery. By using  $^{212}\text{Pb}$  as an in vivo generator for  $^{212}\text{Bi}$ , it is possible to deliver more than 10 times the administered dose compared to  $^{212}\text{Bi}$  while overcoming the time constraints of  $^{212}\text{Bi}$ .(36,37)  $^{212}\text{Pb}$  is a product of  $^{228}\text{Th}$  decay chain and can be produced from the  $^{224}\text{Ra}/^{212}\text{Pb}$  generator. Traditionally, the bifunctional chelator 1,4,7,10-tetraazacyclododecane-1,4,7,10-tetraacetic acid (DOTA) has been used to radiolabel mAbs, peptides, and other molecules with  $^{212}\text{Pb}$ .(38-40) Although DOTA has been used successfully to radiolabel  $^{212}\text{Pb}$  with a high labeling yield, around 30% of  $^{212}\text{Bi}$  is released from the complex during  $^{212}\text{Pb}$  to  $^{212}\text{Bi}$  decay.(41) Also, DOTA requires heating the reaction mixture to  $>80^\circ\text{C}$  which is not ideal for labeling thermolabile proteins like antibodies. To overcome this issue, Brechbiel and coworkers have developed

1,4,7,10-tetra-(2-carbamoyl methyl)-cyclododecane (TCMC) as a novel chelator to stably chelate  $^{212}\text{Pb}$  at  $37^\circ\text{C}$ .(41) Preclinical studies with  $^{212}\text{Pb}$ -TCMC-Trastuzumab demonstrated an improvement in median survival of mice from 19 days to 56 days.(38)  $^{212}\text{Pb}$ -labeled peptides in a melanoma tumor model have shown the improvement in survival from 15 to 50 days.(39) Combination therapy studies of  $^{212}\text{Pb}$ -labeled trastuzumab with gemcitabine or paclitaxel have successfully showed the therapeutic efficacy of this approach where the median survival of animals receiving treatment were improved significantly.(42,43) Because of its success in animal models,  $^{212}\text{Pb}$ -TCMC-Trastuzumab was recently approved for phase I clinical studies at the University of Alabama. The results of this study have clearly demonstrated the potential and feasibility of alpha particle based therapeutic approaches.(44,45) Combining the benefits of superior pharmacokinetics of the PRIT approach with alpha emitters may produce even better results and thus requires further investigation.

## Single-Chain Antibody Fragments (scFvs)

Monoclonal antibodies (mAbs) are a major weapon of the body's immune system against foreign antigens derived from bacterial and viral infections. In 1975, Kohler and Milstein demonstrated for the first time the ability to generate antibodies in vitro by cell fusion between antibody generating B cells and immortal myeloma cells.(46) Since then monoclonal antibodies have transformed cancer diagnostics and therapeutics due to their excellent specificity and binding affinities. The IgG antibody molecule is made up of 4 chains, 2 heavy chains and 2 light chains, arranged in a "Y" shaped structure. (**Fig. 1.1**) The antigen binding domains, which are specific for each antigen, are located on the tips of Fab domains. The fragment crystalline domain (Fc), which binds to the Fc receptors, is involved in recruitment of cytotoxic effector molecules and is responsible for long serum half-lives (> 10 days) of the antibodies. The IgG class of antibodies are 150,000 kDa in size and are bivalent in nature.(47) Even though full length mAbs have been invaluable in recent decades as therapeutics as well as diagnostic agents in a number of diseases, there are instances where Fc-mediated effects are not desirable. For example, the long serum half-life of full length antibodies results in high background noise and poor contrast in imaging applications. The unwanted activation of Fc-mediated activation of Fc-receptors may lead to massive cytokine release and associated cell toxicities.(48) Thus, antibodies have been modified either enzymatically or genetically engineered to be expressed in various monovalent or multivalent forms.

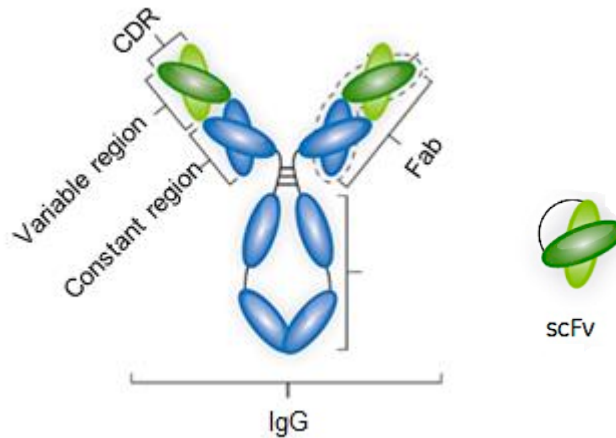


**Fig: 1.1** Schematics of full length IgG monoclonal antibody and single-chain fragment (scFv)

Single-chain variable fragments (scFv) consist of the smallest stabilized antigen binding domain where variable heavy chain (VH) and variable light chain (VL) domains are joined by a flexible peptide linker. (**Fig.1.1**) Each V domain contains three hypervariable loops, which form the antigen-binding site, and are referred to as complementarity determining regions (CDRs). The amino acid sequences of these CDRs are specific for individual antigens. The peptide linker joining VH and VL domains is usually 10-25 amino acids long. The scFv fragments are around 30 KDa in size with each variable domain containing roughly 110 amino acids.(49,50)

The scFv fragments retain the antigen binding specificity of the parent mAbs and offer several advantages over full length antibodies. Due to lack of the

Fc domain, scFvs are devoid of immunogenicity. They can be expressed and purified in large quantities in bacterial as well as mammalian systems. Because of their smaller size, scFvs offer superior pharmacokinetic properties such as higher tissue penetration and rapid whole-body clearance.(51) This is important in the in vivo radioimaging applications where a reduction in background noise is as important as target recognition for attainment of high contrast images. The radiolabeled scFv fragments quickly bind to their tumor targets and any unbound scFvs are excreted out of the body via kidneys within a few hours. These properties have made scFvs one of the most used agents for molecular imaging. So far scFvs have been labeled with several radionuclides ( $^{111}\text{In}$ ,  $^{64}\text{Cu}$ ,  $^{68}\text{Ga}$ ,  $^{99\text{m}}\text{Tc}$ ) for successful in vivo PET and SPECT imaging.(52-55)

Although scFvs offer several advantages they are not without their drawbacks. Due to their monovalent nature, scFvs have lower binding affinities and higher target off rates than the full length antibodies. Combined with their rapid blood clearance rates, this generally impairs the tumor uptake of scFvs. These drawbacks have been remedied by genetically engineering antibodies into various multi-valent forms, which offer higher avidity without compromising fast blood clearance compared to monovalent scFv fragments.

## Phage Display of Antibodies

Phage display technology, first described by Dr. George Smith in 1985, allows insertion of foreign amino acids into phage coat proteins and creating phage display libraries.(56) McCafferty and co-workers reported the display of single-chain antibody fragments (scFvs) on the phage surface in 1990.(57) Since then, phage display has been successfully used to display peptides, various forms of antibodies, receptors, and enzymes.(58-60) The most commonly used phages are the filamentous single-stranded DNA phages (M13, fd and f1) and two of the most common sites for insertion of foreign sequences are coat proteins pIII and pVIII.(61-64) The power of the phage display technology comes from the ability to co-select peptides/proteins and their genes using a large and diverse library. The term antibody phage display library refers to the collection of phage particles that displays antibody fragments on their surfaces. The McCafferty phage display library was created by sequentially cloning a repertoire of human light chain variable regions (VL) followed by human heavy chain regions (VH) in the pSANG4 phagemid. The VH and VL pools were created by PCR amplification of non-immunized human lymphocytes.(57,65) This results in a naïve or non-immunized scFv antibody library that can be used to isolate antibodies against a range of different antigens, including antibodies recognizing “self” proteins or toxic antigens.

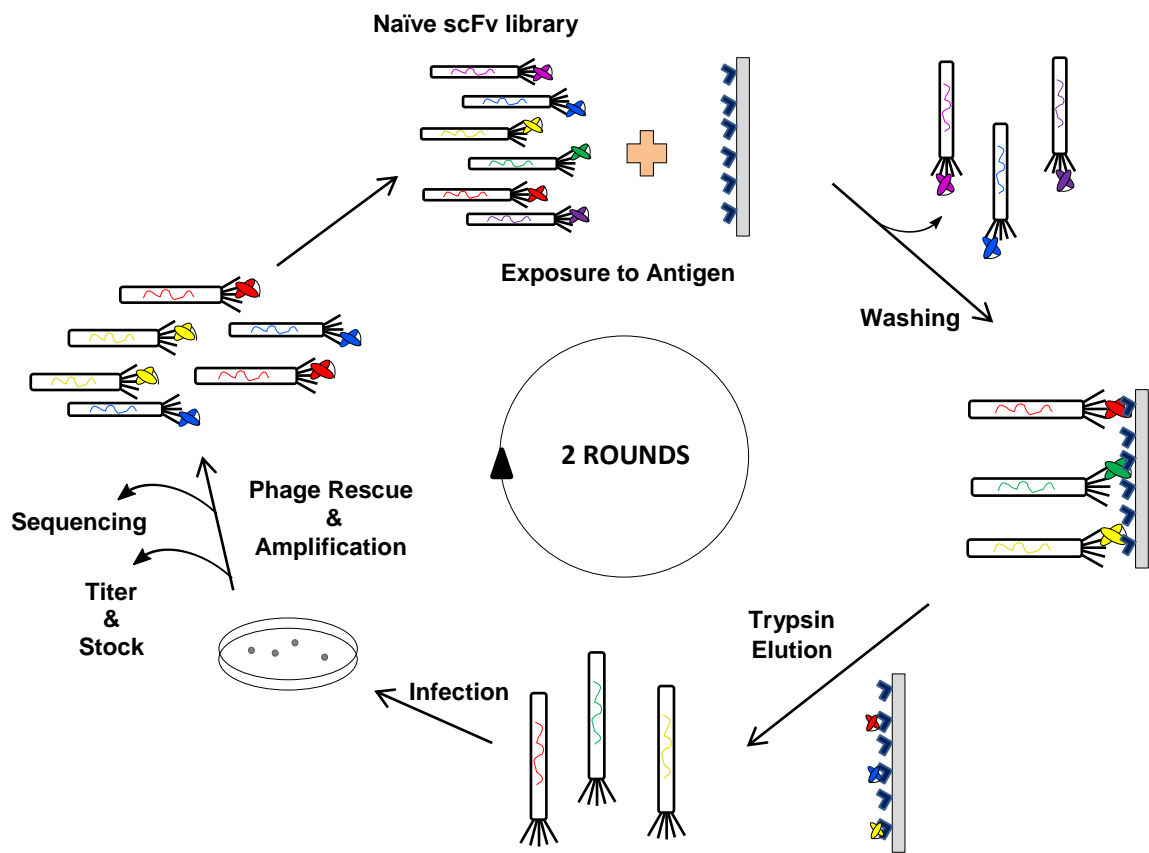


**Figure: 1.2** Schematic of phage display selection process

The goal of an antibody phage display selection process is to isolate a subpopulation of antibodies against a specific biomarker from a large and diverse library. The McCafferty library has a diversity of  $1.1 \times 10^{10}$  unique scFv clones with each clone having around 100 copies.(65) The general scheme of phage display selection involves incubating an entire library with an immobilized target. Phages are allowed to bind to the target and non-specifically bound phages are washed away. The target bound phages are eluted using trypsin mediated proteolytic cleavage and are amplified in TG1 E.coli cells. These amplified phages are then rescued by helper phage superinfection and the resulting subset of phage population is used for the next round of selection (**Fig. 1.2**). The antibody library is subjected to multiple rounds of selection with each round being more stringent than the previous one in order to isolate high affinity antibodies against a target of interest. One has to be careful though as excessive rounds of selection can lead to enrichment of so-called “bald” phages which do not display any scFv but have a significantly higher growth advantage.

The use of trypsin-cleavable KM13 helper phage ensures that only 2 rounds of selection are required instead of the usual 3-4 rounds. This helper phage was engineered with modified pIII protein which has a trypsin-sensitive site in pIII protein (**Fig. 1.3**).(66,67) During phagemid rescue and phage assembly, both pIII protein from helper phage and pIII-scFv fusion protein from phagemid compete for packaging into phage particles. In fact, approximately 90% of all phage particles produced have only pIII protein from the helper phage and do not display scFv on their surfaces. The remaining 10% phages carry at

least one phagemid derived recombinant pIII-scFv fusion protein and thus display antibody fragments on their tips. During trypsin elution, pIII-scFv fusion protein is cleaved between scFv domain and pIII leaving the phage particle with at least one intact pIII protein and their infectivity. Meanwhile trypsin treatment also cleaves helper phage derived pIII proteins resulting in truncated phage particles with defective pIII protein. Because of the loss of D1 and D2 domains in these “bald” particles, they lose their bacterial infectivity. Thus, the use of genetically modified M13 helper phage and trypsin treatment make all particles (phagemid and helper) that do not have at least one phagemid-encoded recombinant pIII-scFv protein non-infective and reduces the population these “bald” phages from the selection process.

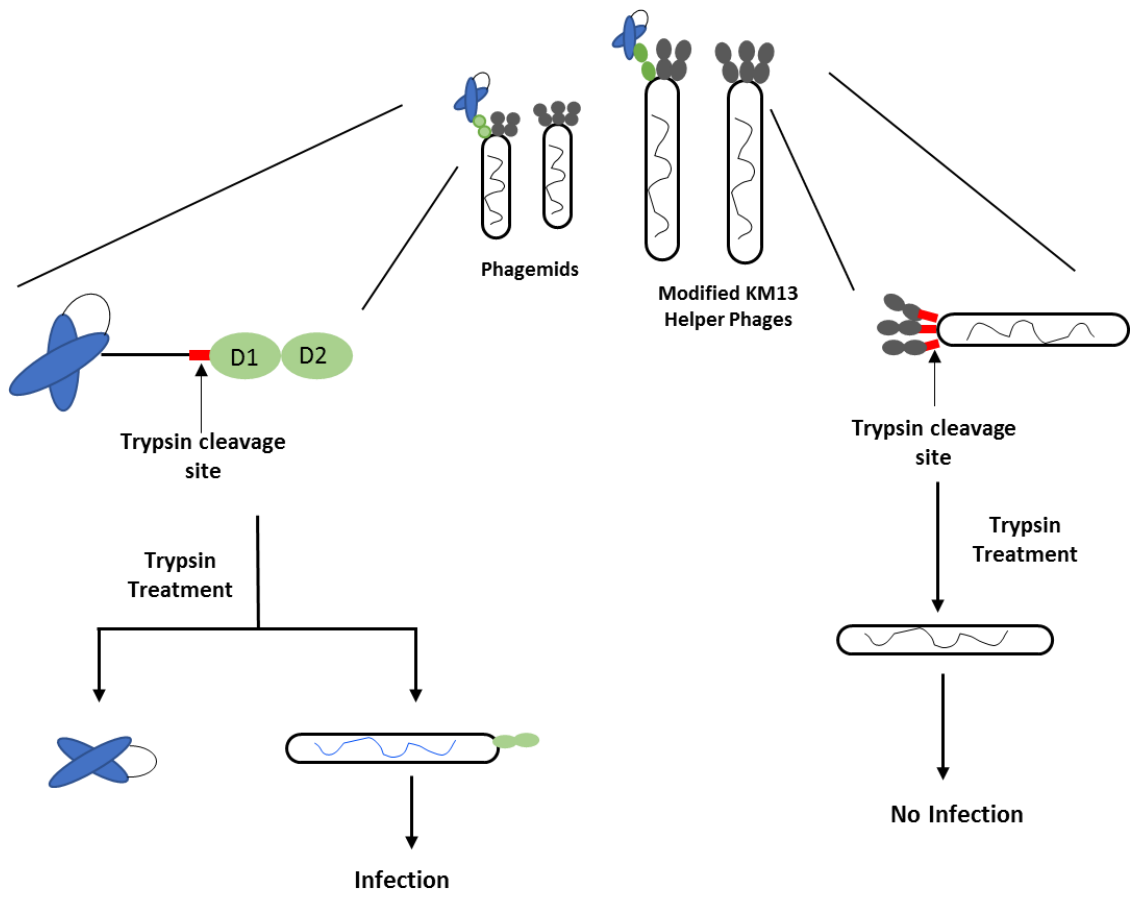


**Fig 1.3:** Principle of trypsin based elution

Isolation of antibody fragments against a specific target can be accomplished using purified protein or directly on the cells expressing a particular target. Phage display can also be used to identify antibodies against non-protein targets like small molecules which is very difficult to achieve using immunization. The scFvs isolated from phage display have binding affinities in the micromolar to nanomolar range.(68,69) This can be further increased by affinity maturation where the sequence of initial lead scFv is used to create a sub-library, which is screened again to enrich for binders with higher binding affinities.(70) Apart from directly selecting human antibodies against a target protein with nanomolar affinities, it is also possible to tailor the selection and screening techniques to isolate antibodies with many other attributes like agonistic or antagonistic properties, potency, specificity, stability, and cross-reactivity.(87-89) Antibody fragments isolated from phage libraries can be readily reformatted into full length IgG format without the loss of function. All of these in vitro flexibilities and advantages make phage display technology very attractive for the discovery of new therapeutics. As of 2017, more than 60 phage display-derived drug candidates are in various stages of clinical trials. So far, US FDA has approved 6 antibodies and 1 peptide based drugs discovered by phage display.(90) Adalimumab (Humira), the first fully human monoclonal antibody drug approved by US FDA, was discovered from phage display using the McCafferty library. Humira had sales of \$18.9 billion worldwide in 2017.(91) This demonstrates the potential and power of phage display technology as rapid, efficient, and relatively inexpensive way of generating biological agents.

## **Matrix Metalloproteinases (MMPs)**

Matrix metalloproteinases (MMPs) are a family of 25 zinc-containing protease enzymes that are involved in degradation of extra cellular matrix (ECM) and basement membrane components. MMPs are structurally related: they all have a propeptide domain, a zinc-containing catalytic domain, and a hemopexin-like domain. The propeptide domain gets cleaved during the activation leaving a truncated active enzyme, while the hemopexin domain is involved in protein-protein interaction and substrate specificity.(71) The ECM is a complex and dynamic network that is made up various macromolecules such as collagens, fibronectins, proteoglycans, glycosaminoglycans, and other glycoproteins. It acts as a glue to keep cells together and functions as a pool of various growth factors and signaling molecules. In normal physiological condition, the ECM plays an important role in embryonic development, morphogenesis, tissue resorption and remodeling, cell differentiation, growth, migration, and apoptosis.(72) The degradation of ECM by MMPs can thus have a profound impact on tissue structure, function, and remodeling.(73) The uninhibited activities of MMPs have been implicated in various pathological conditions like inflammation, arthritis, fibrosis, and cancer.(74-77) Because MMPs are involved in degradation of ECM components, they are known to help cancer cells in detachment from the primary tumor cells, allowing them to escape into blood vessels for metastasis. Several MMPs are implicated in their role in cancer metastasis and it is possible that they work in tandem.(78,79)

MMP-12 is a 54 kDa proteolytic enzyme which is mainly secreted by macrophages.(80) MMP-12 is implicated in numerous diseases like atherosclerosis, aortic aneurysm, chronic obstructive pulmonary disease (COPD), and rheumatoid arthritis.(81-84) Recently, more and more evidences are emerging which suggest that MMP-12 plays important role in lung cancer. MMP-12 overexpression by lung tissues has been correlated with lung cancer propagation.(85) At the same time, knockdown of MMP-12 from lung adenocarcinoma cells suppresses the cell growth and invasiveness of the tumor cells.(86) This body of evidences suggests that MMP-12 might be a potential target for lung cancer diagnosis as well as for therapy.

Due to advantages offered by phage display, we decided to identify MMP-12 specific scFvs and investigate if MMP-12 can be used as a novel biomarker for lung cancer detection. This project is detailed in Chapter 3.

## CHAPTER 2

### **Metal-Free Cycloaddition Chemistry Driven Pretargeted Radioimmunotherapy Using $\alpha$ -Particle Radiation**

This work has been published in *Bioconjugate Chemistry*, Volume 28.11, Pages 3007-3015 in 2017 under the title "Metal-Free Cycloaddition Chemistry Driven Pretargeted Radioimmunotherapy Using  $\alpha$ -Particle Radiation" It is reprinted with permission (© American Chemical Society 2018).

Manankumar A. Shah, Xiuli Zhang, Raffaella Rossin, Marc S. Robillard, Darrell R. Fisher, Tyler Buelmann, Freek J. M. Hoeben, and Thomas P. Quinn are co-authors of this work

## Introduction

Conventional radioimmunotherapy (RIT) involves a single step approach in which a tumor targeting monoclonal antibody (mAb) is directly radiolabeled. Once injected, the radiolabeled mAb circulates throughout the body and ultimately binds to its target on tumor cells. The radiation emitting from the radionuclide delivers the therapeutic dose to tumor cells.(92,93) However, the success of RIT has been limited due to poor pharmacokinetic properties of antibodies. The large molecular weight of the radiolabeled mAb results in extended biodistribution and whole-body clearance. This prolonged blood circulation of radiolabeled mAbs results in lengthy radiation exposure to non-target normal tissues, which in turn limits the amount of radiation dose administered and reduces the therapeutic efficacy.(94-96)

Pretargeted radioimmunotherapy (PRIT) is an alternative strategy developed to address the drawbacks associated with conventional RIT. Pretargeting is a multistep approach which essentially separates the delivery of the tumor targeting molecule from the delivery of the radionuclides. The general scheme of pretargeting involves administration of tumor targeting mAb, which has been modified with a specific tag. This modified mAb is allowed to circulate throughout the body and accumulate on the tumor. The unbound mAb is cleared from the blood usually via liver and GI tract. The clearance of unbound mAb from the blood can be accelerated by administration of a clearing agent. This is followed by the administration of low molecular weight radioactive effector molecules, which have a very high affinity and specificity for the tag on the

modified mAb. Due to their small size and fast pharmacokinetics, radiolabeled effector molecules bind rapidly to the pretargeted mAb on the tumor and any unbound radioactive effector molecules are quickly cleared out of the blood via kidneys. As a result, PRIT achieves a high tumor/non-tumor (T/NT) ratio allowing administration of high radiation doses with minimal exposure to normal tissues.(97,98) Several pretargeting approaches have been investigated extensively in preclinical studies, which include bispecific antibodies (bsAb), avidin/streptavidin- biotin based systems, mAb conjugated to oligonucleotides and mAb conjugated to enzymes.(99-103) Although these strategies have shown some success over the years, their effectiveness is limited because of some limitations. For example, streptavidin-biotin system causes induction of adverse immune reactions, while bispecific antibodies suffer from complexity and high production costs as well as moderate biomarker binding constants.(20) Novel bioorthogonal chemical reactions that do not suffer from these limitations have increasingly been investigated over the last decade.(104) The widely evaluated bioorthogonal reactions include the Staudinger ligation, the strain promoted alkyne-azide cycloaddition (SPAAC) and the inverse electron demand Diels-Alder reaction (IEDDA).(26-31) In 2010, Robillard *et al.* demonstrated the first successful in vivo application of an IEDDA reaction between *trans*-cyclooctene (TCO) and tetrazine (Tz) for SPECT imaging using CC49-TCO mAb and <sup>111</sup>In-DOTA-Tz. In subsequent studies, a clearing agent was developed to reduce circulating unbound antibody prior to radiolabeled tetrazine administration. Dosimetry studies demonstrated that the use of clearing agent resulted in an 8-

fold increased dose to the tumor. Moreover, they showed the potential and feasibility of an IEDDA based pretargeting approach for in vivo PRIT using  $^{177}\text{Lu}$ -DOTA-Tz.(105-107) Recently, Houghton *et al.* showed that a pretargeted approach can reduce total body dose and demonstrated the in vivo efficacy of a PRIT regimen using a  $\beta$ -emitters  $^{177}\text{Lu}$  labeled tetrazine and TCO modified mAb.(32,108)

Alpha-particles are charged  $\text{He}^{+2}$  nuclei with radionuclide energies ranging from 2 to 10 MeV. The linear energy transfer of  $\alpha$ -particles, typically  $\sim 100$  keV/ $\mu\text{m}$ , is significantly higher than that of  $\beta$ -particles ( $\sim 0.2$  keV/ $\mu\text{m}$ ). Furthermore,  $\alpha$ -particles have a very short tissue path length of  $\sim 100$   $\mu\text{m}$  and can deposit  $\sim 1500$  times more energy per unit path length than  $\beta$ -particles. The cytotoxic effects of  $\alpha$ -particles resulting from irreversible double strand DNA damage are independent of dose rate, dose fractionation, or tissue oxygen levels. These properties make  $\alpha$ -particle based therapeutic approaches attractive for targeted treatment strategies. The most widely studied radionuclides for targeted  $\alpha$ -radiotherapy include  $^{225}\text{Ac}$  ( $t_{1/2} \sim 10.0$  days),  $^{211}\text{At}$  ( $t_{1/2} \sim 7.2$  days),  $^{212}\text{Bi}$  ( $t_{1/2} \sim 60.5$  minutes),  $^{213}\text{Bi}$  ( $t_{1/2} \sim 45.6$  minutes), and  $^{212}\text{Pb}$  ( $t_{1/2} \sim 10.6$  hours).(34-36,109,111) Moreover, the use of parent radionuclides as an in vivo generator of short half-life  $\alpha$ -emitters has also been successfully employed.(37-39) In this report  $^{212}\text{Pb}$ , parent of the  $\alpha$ -emitter  $^{212}\text{Bi}$ , was used to overcome difficulties associated with short half-life of  $^{212}\text{Bi}$  ( $t_{1/2} \sim 60$  min). Our laboratory has successfully demonstrated the use of  $^{212}\text{Pb}$  in a peptide targeted  $\alpha$ -particle therapy on melanoma tumors.(39) Over the years, Brechbiel *et al.* and others

have shown the feasibility and therapeutic efficacy of targeted RIT using  $^{212}\text{Pb}$ -Transtuzumab.(40,112,113) Recently, the results of the first clinical trial employing  $^{212}\text{Pb}$ -Transtuzumab have further confirmed the safety and suitability of  $^{212}\text{Pb}$  in radioimmunotherapy.(44,45)

In this study, we investigated the feasibility and effectiveness of pretargeted  $^{212}\text{Pb}$   $\alpha$ -particle radioimmunotherapy using in vivo IEDDA chemistry in mice bearing LS174T human colon carcinoma xenografts. We compared and evaluated two tetrazine-PEG conjugated chelators 1,4,7,10-tetraazacyclododecane-1,4,7,10-tetraacetic acid (DOTA) and 1,4,7,10-tetra-(2-carbamonyl methyl)-cyclododecane (TCMC) (**Fig. 2.1**) for their  $^{212}\text{Pb}$  radiolabeling efficiencies and in vivo pharmacokinetic properties. CC49, a mouse IgG mAb which binds to the tumor-associated glycoprotein (TAG-72) antigen, was used as the tumor targeting molecule. A three step pretargeting protocol involving pretargeted CC49-TCO mAb, administration of a clearing agent and  $^{212}\text{Pb}$ -DOTA-Tz was carried out for radioimmunotherapy. The results of the IEDDA based  $\alpha$ -PRIT therapy regimen yielded dose-dependent reductions in tumor growth with improved survival, highlighting the clinical potential of the  $\alpha$ -particle based PRIT.

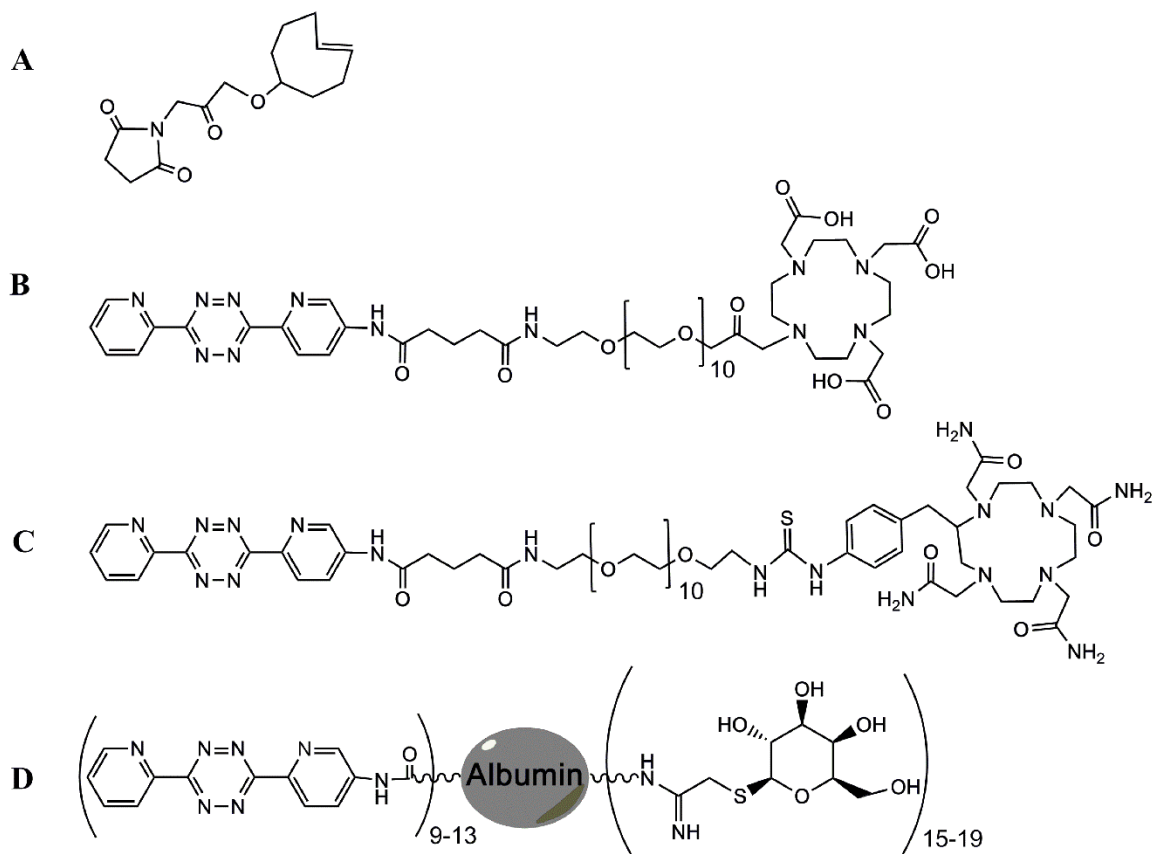


**Figure 2.1:** Structures of pretargeting reagents used in the study. A) TCO-NHS, B) DOTA-PEG<sub>10</sub>-Tetrazine and, C) TCMC-Bn-SCN-PEG<sub>10</sub>-Tetrazine, and D) Galactose-albumin-Tetrazine based clearing agent.

## Materials and Methods

### Antibody Preparation and TCO conjugation:

CC49 mAb was purified from the supernatant of its hybridoma cell line (American Type Culture collection, VA) using protein G affinity column chromatography (GE Healthcare, NJ) as per the manufacturer's instructions. Rituximab (Genentech Inc.), a human mAb which targets CD20 on the surface of B-cells, was used in therapy as a non-targeting control antibody.

### CC49-TCO Conjugation:

To modify CC49 mAb with TCO, 2 mg of CC49 (8 mg/ml in PBS) was incubated with 10 molar equivalent excess of TCO-NHS (1 mg/ml in dry DMSO). The pH was adjusted to 9.0 with 1M carbonate buffer and the reaction was carried out for 30 minutes at room temperature with agitation. The TCO modified CC49 was purified using PD-10 desalting columns (GE healthcare, NJ) and the concentration was measured by NanoDrop (Thermo Scientific). The average number of TCO molecules per antibody was calculated by titrating CC49-TCO with radiolabeled Tz as previously reported (data not shown).<sup>21</sup>

### Radiolabeling:

<sup>224</sup>Ra/<sup>212</sup>Pb radionuclide generators were purchased from the US Department of Energy, Oak Ridge National Laboratory (Oak Ridge, Tennessee). Preferential elution of <sup>212</sup>Pb was carried out by rinsing the generator column with 0.5 N HCl to remove <sup>212</sup>Bi and its daughters. Subsequently, the generator column

was rinsed with 2 N HCl to elute  $^{212}\text{Pb}$ . The eluent was mixed with 2 M  $\text{HNO}_3$  in a glass vial and the resulting solution was heated to dryness on a hot plate. The  $^{212}\text{Pb-Pb}(\text{NO}_3)_2$  residues were dissolved in 0.5 M ammonium acetate buffer (pH 5.5) and used for radiolabeling.

DOTA-PEG<sub>10</sub>-Tz was synthesized as previously reported.<sup>22</sup> Synthesis of TCMC-PEG<sub>10</sub>-Tz is described in the supporting information (Scheme S1). For radiolabeling, DOTA-Tz or TCMC-Tz (2 mg/ml in 0.5M  $\text{NH}_4\text{Ac}$ , pH 7.0) was combined with an appropriate amount of  $^{212}\text{Pb-Pb}(\text{NO}_3)_2$  solution. The pH was adjusted to 5.5 and the reaction mixture was incubated at 60°C for 20 minutes. Unbound  $^{212}\text{Pb}$  was removed using a PD-10 column. Fractions containing  $^{212}\text{Pb}$  were pooled and mixed with 10 mM diethylenetriaminepentaacetic acid DTPA (5  $\mu\text{L}$ ) and gentisic acid (20 mg/ml, 100  $\mu\text{g}$ / mouse dose; pH 5.5). The radiolabeling yield was measured by instant thin layer chromatography (ITLC) using 200 mM ethylenediaminetetraacetic acid (EDTA) as mobile phase. To determine the stability of radiolabeled complexes, an aliquot of  $^{212}\text{Pb-DOTA-Tz}$  and  $^{212}\text{Pb-TCMC-Tz}$  was diluted in PBS, added to serum and incubated at 37°C. Samples were taken at various time points and analyzed by ITLC. The effective specific activity of  $^{212}\text{Pb-Labeled Tz}$  used for biodistribution was approximately 0.8  $\mu\text{Ci/nmol}$  of the tetrazine chelator.

### **Tumor Model:**

All animal experiments were carried out in compliance with the Institutional Animal Care and Use committee approval. The pharmacokinetic and therapy studies were carried out in athymic female BALB/C (*nu/nu*) mice (Envigo, USA). The human colon carcinoma cell line LS174T was obtained from ATCC and was maintained in RPMI 1640 medium supplemented with 1% L-glutamine, 10% FBS and 1% penicillin/streptomycin. Mice were inoculated subcutaneously (s.c.) with  $4 \times 10^6$  LS174T cells in 100  $\mu$ L sterile PBS in the right flank and used when tumors were clearly visible, palpable and measurable.

### **Blood Clearance and Biodistribution of DOTA-Tz and TCMC-Tz:**

Two groups of 3 tumor bearing mice were injected intravenously via tail vein with  $^{212}\text{Pb}$ -DOTA-Tz and  $^{212}\text{Pb}$ -TCMC-Tz (100  $\mu$ L/ mouse,  $\sim 10$   $\mu$ Ci) to examine blood clearance. The mice were serially bled and blood samples were collected at 10, 20, 30, 60 minutes and 24 hours. The blood samples were weighed and counted for radioactivity. In a separate experiment, two groups of LS174T tumor mice (n=3) were injected intravenously with  $^{212}\text{Pb}$ -DOTA-Tz and  $^{212}\text{Pb}$ -TCMC-Tz (100  $\mu$ L/ mouse,  $\sim 10$   $\mu$ Ci) to study the biodistribution profile of the compounds. The mice were sacrificed at 30 minutes, 3 and 6 hours post injection (p.i.), and tumors and organs of interest were harvested, weighed, and counted to measure radioactivity. The radioactive tissue samples were counted using gamma counter and the results were expressed as a percentage of injected dose per gram (% ID/g) and as a percentage injected dose (% ID).

### **Pretargeted Biodistribution:**

Mice with visible and palpable tumors (n=3 mice per group) were selected for biodistribution studies and were injected with CC49-TCO via tail vein (100 µg/100 µL per mouse). Unbound, freely circulating antibodies were removed from circulation by administration of two doses of a galactose- albumin-Tz based clearing agent (120 µg/ 100 µL per mouse) 30 h and 48 h post CC49-TCO injection. The clearing agent should capture any unbound mAb in the blood and remove it from the circulation to the liver via Ashwell receptors on hepatocytes.<sup>21</sup> Two hours after the last dose of clearing agent, mice were injected with a 10 molar excess to CC49-TCO of either <sup>212</sup>Pb-DOTA-Tz or <sup>212</sup>Pb-TCMC-Tz (~5 µCi per mouse containing 100 µg of gentisic acid and 50 nmol of DTPA). The mice were sacrificed 3 h, 24 h and 48 h after the injection of radiolabeled-tetrazine. Tumors and other major organs were harvested, weighed and counted for radioactivity. Blood values were assumed to be 6.5% of whole body weight. Radioactivity in the remainder of the carcasses was also counted to determine the whole body retention and clearance by accounting for all the activity in the mice.

## Dosimetry Studies:

Dosimetry calculations were based on total radiation energy deposited per unit mass, as determined for the  $\beta$ -decay of  $^{212}\text{Pb}$  as well as  $\alpha$ ,  $\beta$  and  $\gamma$  radiations emitted for  $^{212}\text{Bi}$ .<sup>43</sup> The biodistribution profiles of  $^{212}\text{Pb}$ -DOTA-Tz and  $^{212}\text{Pb}$ -TCMC-Tz for the organ and tissues in the LS174T tumor-bearing mice pretargeted with CC49-TCO were used to calculate radiation absorbed doses to the tumors and also to the mouse normal organs and tissues using methods described previously.<sup>(39,116-118)</sup> Similar methods were previously used to calculate alpha-particle radiation doses in mice from  $^{213}\text{Bi}$  and  $^{211}\text{At}$ .<sup>(119,120)</sup> For each tumor, organ, or tissue, the time-activity measurement data were plotted, and a time-activity function was fitted to the plotted data by least-squares regression analysis; these included time-activity data generated for 14 organs (blood, brain, heart, lung, liver, spleen, stomach, kidneys, small intestine, large intestine, muscle, skin, bone and tumor). Integration of the time activity curves yielded the cumulative number of radioactive disintegrations for  $^{212}\text{Pb}$  and  $^{212}\text{Bi}$  in each organ. The cumulative activities associated with each organ or tissue were then multiplied by the equilibrium dose constants for each of the alpha- and beta-emissions to yield the cumulative absorbed dose, integrated to infinity (for complete biological clearance or radioactive decay), together with an accounting for beta-particle absorbed fractions. Cross-organ beta doses for these organs were negligible compared to the radiation self-organ-dose imparted by alpha particles, and were not included.

### **Pretargeted Therapy:**

Pretargeted radioimmunotherapy was performed in mice bearing LS147T human colon carcinoma xenografts. Tumor bearing mice were randomized into study groups (n=8 mice per group) 4 days post LS174T cell inoculation ensuring that all study groups have approximately equal tumor volumes. Initially, four groups of tumor bearing animals (n=8) were injected with 100 µg of CC49-TCO, followed by two doses of clearing agent at 30 h and 48 h. These mice were treated with 75 µCi, 125 µCi and 200 µCi of <sup>212</sup>Pb-DOTA-Tz (10 molar equivalents to CC49-TCO) two hours after the last dose of clearing agent (**Fig. 2.3**). To determine the efficacy of a multi-dose regimen, one group of mice (n=8) was pretargeted with CC49-TCO and two doses of clearing agent, followed by two doses of 75 µCi of <sup>212</sup>Pb-DOTA-Tz at a 7 day interval. Two non-treatment control groups of mice (n=8) were injected with 100 µL of PBS and 100 µg of CC49-TCO. As a non-specific control, a group of 8 mice was injected with rituximab-TCO (RTX-TCO) and received 200 µCi of <sup>212</sup>Pb-DOTA-Tz. To compare the therapeutic efficacy of PRIT vs. RIT regimen, one group of mice (n=8) was treated with 15 µCi of direct labeled <sup>212</sup>Pb-TCMC-CC49, which was reported to be the maximum tolerated dose.(111) All injections were carried out i.v. through tail vein and mice were monitored for tumor size, body weight and body score twice a week. Tumor volume was calculated by measuring length, width and depth of the tumors with digital caliper and using the following formula: Tumor volume = length x width x depth. Mice were removed from the therapy study and sacrificed if weight loss was > 20% of initial weight, tumor volume exceeded 1.0

cm<sup>3</sup>, or the appearance of skin ulceration on the tumor. To determine the hematological toxicity, blood samples were collected at the time of animal sacrifice. White Blood Count (WBC), total and differential leukocyte count, Red Blood Cell (RBC) count and platelet counts were performed for each tumor bearing mouse group and compared with a non-tumor bearing control mouse group. Histopathological studies were performed on tumor and kidney tissue samples from the PBS, 75 µCi, and 200 µCi treatment groups.

### **Statistical Analysis:**

The values for all samples in the different experimental conditions were averaged, and the standard error or standard deviation of the mean was calculated. All values were expressed as mean ± sd. Differences between means were determined using the unpaired Student's *t*-tests. Kaplan-Meier survival curves were generated using Graph Pad Prism software and curve comparison was done using Log-rank (Mantel-Cox) test model. (\**P* < 0.05, \*\**P* < 0.01, \*\*\**P* < 0.001)

## Results

### Radiolabeling and Pharmacokinetics of $^{212}\text{Pb}$ Labeled Tetrazine Conjugates:

The radiolabeling efficiencies for both  $^{212}\text{Pb}$ -DOTA-Tz and  $^{212}\text{Pb}$ -TCMC-Tz (**Fig. 2.1**) were found to be  $\geq 95\%$ . Both compounds also exhibited high serum stability with  $>85\%$  of  $^{212}\text{Pb}$ -DOTA-Tz and  $>91\%$  of  $^{212}\text{Pb}$ -TCMC-Tz remaining intact after 24 hours incubation.

The blood clearance of  $^{212}\text{Pb}$ -DOTA-Tz and  $^{212}\text{Pb}$ -TCMC-Tz was very rapid with  $\sim 95\%$  of activity cleared out of blood within first 3 hours p.i. (**Fig. 2.2A-B**). The  $t_{1/2}$  values for  $^{212}\text{Pb}$ -DOTA-Tz and  $^{212}\text{Pb}$ -TCMC-Tz were found to be  $< 60$  minutes. Further, the pharmacokinetic profiles of the two radiolabeled tetrazine compounds were evaluated for their tissue uptake and whole body clearance (**Fig. 2.2C-D**). Both  $^{212}\text{Pb}$ -DOTA-Tz and  $^{212}\text{Pb}$ -TCMC-Tz exhibited rapid tissue and whole body clearance with  $\sim 77\%$  and  $\sim 74\%$  of injected dose cleared through urine by 3 hours p.i., respectively. At 24 hours, there was no uptake of  $^{212}\text{Pb}$ -DOTA-Tz in any of major organs except for kidneys (2.3% ID/g), which was the primary route of excretion. In contrast, the biodistribution of  $^{212}\text{Pb}$ -TCMC-Tz at 24 hours showed significant uptake in liver ( $\sim 15.6\%$  ID/g), spleen (3.2% ID/g), lung (2.0% ID/g) and kidneys (3.0% ID/g).

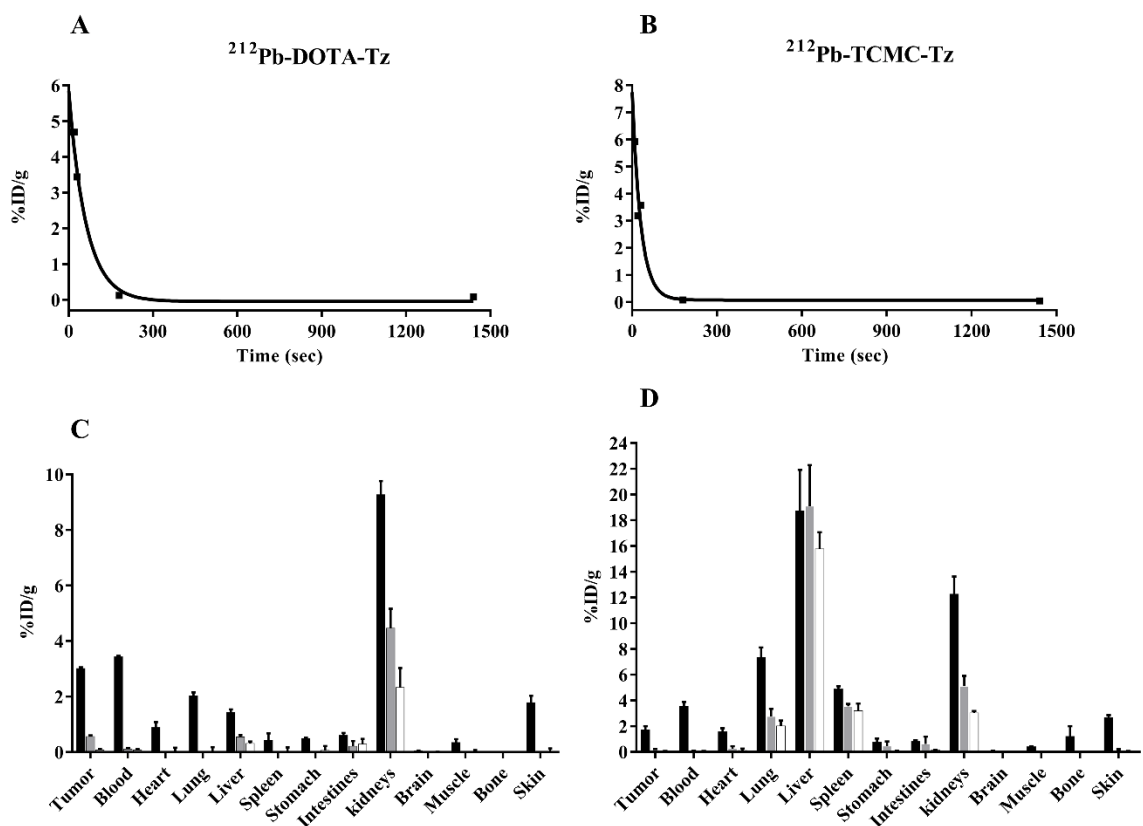


**Figure 2.2:** Pharmacokinetics of  $^{212}\text{Pb}$ -labeled tetrazines (without the pretargeted mAb) in mice bearing LS174T human colon carcinoma xenograft. Blood Clearance of A)  $^{212}\text{Pb}$ -DOTA-Tz and B)  $^{212}\text{Pb}$ -TCMC-Tz. Biodistribution of C)  $^{212}\text{Pb}$ -DOTA-Tz and D)  $^{212}\text{Pb}$ -TCMC-Tz in LS174T tumor bearing mice at 30 minutes (■), 3 hours (▒), and 24 hours (□) post injection (n=3).

### **Pretargeted Biodistribution:**

The biodistribution and tumor-targeting properties of  $^{212}\text{Pb}$ -DOTA-Tz and  $^{212}\text{Pb}$ -TCMC-Tz were evaluated in LS174T tumor bearing mice pretargeted with CC49-TCO mAb (**Table 2.1**).  $^{212}\text{Pb}$ -DOTA-Tz showed rapid tumor uptake and minimum accumulation in other major body tissues. The tumor uptake value for  $^{212}\text{Pb}$ -DOTA-Tz reached  $0.94 \pm 0.47\%$  ID/g by 3 hours p.i. and then decreased to  $0.66 \pm 0.11\%$  ID/g by 24 hours p.i. Clearance from blood ( $0.1 \pm 0.02\%$  ID/g at 3 hours and  $0.04 \pm 0.02\%$  ID/g at 24 hours) and other major organs was rapid and no non-specific uptake was observed except for the kidneys ( $2.53 \pm 0.23\%$  ID/g at 3 hours and  $1.33 \pm 0.16\%$  ID/g at 24 hours). Given that  $t_{1/2}$  of  $^{212}\text{Pb}$  is  $\sim 10.6$  hours, almost no tissue activity was measured at 48 hours p.i. In comparison,  $^{212}\text{Pb}$ -TCMC-Tz also displayed rapid tumor accumulation with a higher uptake value of  $1.64 \pm 1.22\%$  ID/g at 3 hours p.i. which dropped to  $0.50 \pm 0.17\%$  ID/g by 24 hours p.i. While  $^{212}\text{Pb}$ -TCMC-Tz cleared out of blood rapidly ( $0.12 \pm 0.09\%$  ID/g at 3 hours and  $0.01 \pm 0.04\%$  ID/g at 24 hours p.i.), a significant uptake in the liver was observed. The liver accumulation of  $^{212}\text{Pb}$ -TCMC-Tz at 3 hours and 24 hours was  $5.39 \pm 1.31\%$  ID/g and  $2.49 \pm 0.35\%$  ID/g, respectively. The high liver uptake of  $^{212}\text{Pb}$ -TCMC-Tz in the pretargeting study was consistent with tissue distribution of  $^{212}\text{Pb}$ -TCMC-Tz alone as described above.

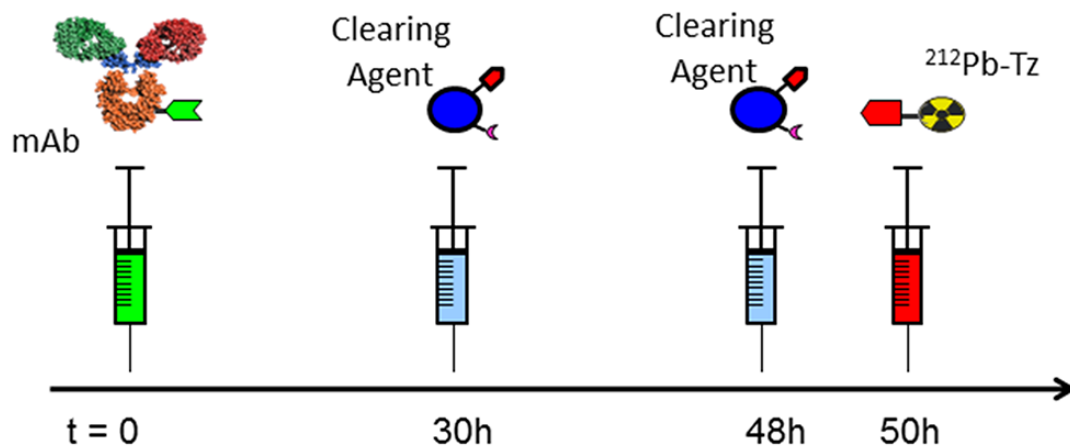


**Figure 2.3:** Schematic of the pretargeting protocol used in this study. Tumor bearing mice were first injected with TCO modified mAb. To remove circulating antibodies from the blood, two doses of clearing agent were administered at 30 h and 48 h post mAb injections. Two hours after the last dose of clearing agent, mice were injected with  $^{212}\text{Pb}$ -labeled tetrazine probes.

**Table 2.1:** Biodistribution of  $^{212}\text{Pb}$ -DOTA-Tz and  $^{212}\text{Pb}$ -TCMC-Tz in LS174T tumor bearing nude mice pretargeted with CC49-TCO mAb.

Tissues	$^{212}\text{Pb}$ -DOTA-Tz (%ID/g)			$^{212}\text{Pb}$ -TCMC-Tz (%ID/g)		
	3 Hours	24 Hours	48 Hours	3 Hours	24 Hours	48 Hours
<b>Tumor</b>	0.94 ± 0.47	0.66 ± 0.11	0.00 ± 0.00	1.64 ± 1.22	0.50 ± 0.17	0.58 ± 0.05
<b>Blood</b>	0.10 ± 0.02	0.04 ± 0.02	0.00 ± 0.00	0.12 ± 0.09	0.01 ± 0.04	0.12 ± 0.01
<b>Heart</b>	0.03 ± 0.03	0.00 ± 0.00	0.00 ± 0.00	0.00 ± 0.00	0.00 ± 0.00	0.14 ± 0.22
<b>Lung</b>	0.20 ± 0.04	0.09 ± 0.06	0.00 ± 0.00	0.41 ± 0.28	0.13 ± 0.23	0.28 ± 0.15
<b>Liver</b>	0.28 ± 0.03	0.21 ± 0.05	0.17 ± 0.11	5.39 ± 1.31	2.49 ± 0.35	2.53 ± 0.30
<b>Spleen</b>	0.01 ± 0.00	0.00 ± 0.00	0.00 ± 0.00	0.19 ± 0.24	0.05 ± 0.14	0.54 ± 0.11
<b>Stomach</b>	0.25 ± 0.13	0.08 ± 0.11	0.00 ± 0.00	0.48 ± 0.23	0.06 ± 0.10	0.12 ± 0.05
<b>Intestines</b>	0.44 ± 0.12	0.12 ± 0.14	0.01 ± 0.01	0.70 ± 0.02	0.08 ± 0.03	0.19 ± 0.15
<b>Kidneys</b>	2.53 ± 0.23	1.33 ± 0.16	0.47 ± 0.20	4.07 ± 0.93	2.46 ± 0.44	1.79 ± 0.18
<b>Brain</b>	0.00 ± 0.00	0.00 ± 0.00	0.00 ± 0.00	0.00 ± 0.00	0.00 ± 0.00	0.03 ± 0.01
<b>Muscle</b>	0.00 ± 0.00	0.00 ± 0.00	0.00 ± 0.00	0.00 ± 0.00	0.00 ± 0.00	0.00 ± 0.00
<b>Bone</b>	0.00 ± 0.00	0.00 ± 0.00	0.00 ± 0.00	0.00 ± 0.00	0.00 ± 0.00	0.89 ± 0.78
<b>Skin</b>	0.17 ± 0.17	0.12 ± 0.06	0.00 ± 0.00	0.07 ± 0.05	0.00 ± 0.00	0.16 ± 0.09

**Dosimetry:**

The mean organ absorbed doses to tumors, organs, and tissues per unit administered activity for  $^{212}\text{Pb}$ -DOTA-Tz and  $^{212}\text{Pb}$ -TCMC-Tz were calculated using the measured biodistribution data in mice bearing LS174T tumors (**Table 2.2**). The absorbed doses to tumor tissue from  $^{212}\text{Pb}$ -DOTA-Tz and  $^{212}\text{Pb}$ -TCMC-Tz were found to be 4.83 cGy/ $\mu\text{Ci}$  and 9.42 cGy/ $\mu\text{Ci}$  respectively. Normal organ doses for  $^{212}\text{Pb}$ -DOTA-Tz were comparatively low except for the kidneys, which were calculated to be 12.6 cGy/ $\mu\text{Ci}$ . The absorbed doses to kidneys and liver for  $^{212}\text{Pb}$ -TCMC-Tz were 34.4 cGy/ $\mu\text{Ci}$  and 43.7 cGy/ $\mu\text{Ci}$ , respectively.

**Table 2.2:** Absorbed radiation doses from  $^{212}\text{Pb}$ -DOTA-Tz and  $^{212}\text{Pb}$ -TCMC-Tz in mice bearing LS174T colon carcinoma tumors.

	$^{212}\text{Pb}$ -DOTA-Tz	$^{212}\text{Pb}$ -TCMC-Tz
<b>Tissue</b>	<b>cGy/<math>\mu\text{Ci}</math></b>	<b>cGy/<math>\mu\text{Ci}</math></b>
Tumor	4.83	9.42
Blood	0.937	2.47
Heart	0.0867	N/A
Lung	0.789	3.74
Liver	2.44	43.7
Spleen	0.0746	N/A
Stomach	0.584	1.8
L. Intestine	1.63	3.55
S. Intestine	0.884	1.44
Kidneys	12.6	34.4
Brain	0.0181	N/A
Muscle	0.0489	N/A
Carcass	0.943	2.65
Bone	0.329	N/A
Skin	0.991	N/A

### **Pretargeted Therapy:**

The pretargeted radioimmunotherapy studies were carried out in LS147T tumor bearing mice following the protocol depicted in **Fig. 2.3**. The effects of  $^{212}\text{Pb}$ -DOTA-Tz treatment on tumor growth rate as well as body weight are shown in **Fig. 2.4**. Mouse groups receiving the single dose of 75  $\mu\text{Ci}$  and 200  $\mu\text{Ci}$  of  $^{212}\text{Pb}$ -DOTA-Tz exhibited substantial tumor growth inhibition over the study period with mean tumor volume of  $0.14 \pm 0.13 \text{ cm}^3$  and  $0.06 \pm 0.06 \text{ cm}^3$  respectively, on day 20. By comparison, tumors in the non-treatment control groups, which received PBS and CC49-TCO, grew rapidly and had to be sacrificed on day 20 due to large tumor volume (mean tumor volume  $> 0.6 \text{ cm}^3$ ) and over-all poor body condition. Mice which received a single 15  $\mu\text{Ci}$  dose of directly labeled  $^{212}\text{Pb}$ -TCMC-CC49 or pretargeted RTX-TCO and 200  $\mu\text{Ci}$  of  $^{212}\text{Pb}$ -DOTA-Tz exhibited slower tumor growth rate than that of the non-treated control groups but faster than the mice in the PRIT regimen (**Fig. 2.4A**). Mice that received either 200  $\mu\text{Ci}$  of  $^{212}\text{Pb}$ -DOTA-Tz or 15  $\mu\text{Ci}$  of  $^{212}\text{Pb}$ -TCMC-CC49 were sacrificed on day 20 due to acute radiation toxicity and poor body score.

In a second therapy study, a multi-dose therapy regimen (2 doses of 75  $\mu\text{Ci}$  at 7 days interval) was compared with an intermediated dose of 125  $\mu\text{Ci}$ . The results showed that both treatment groups exhibited substantial inhibition of tumor growth over time compared to non-treatment group (**Fig. 2.4C**). In addition to tumor volume, animal weights were also monitored following the administration of the dose (**Fig. 2.4B, D**). Although mice receiving high dose of radiation (125  $\mu\text{Ci}$  and 200  $\mu\text{Ci}$  therapy groups) showed a temporary loss in body weight, they

recovered and maintained an acceptable level (>80 % original body weight) throughout the course of study.

Based on the Kaplan-Meier analyses, the median survival of treatment groups receiving 75  $\mu\text{Ci}$ , 125  $\mu\text{Ci}$  and 2 x 75  $\mu\text{Ci}$  of pretargeted  $^{212}\text{Pb}$ -DOTA-Tz were 26, 28 and 31 days, respectively (**Fig. 2.5**). The median survival of groups receiving 200  $\mu\text{Ci}$  dose and 15  $\mu\text{Ci}$  of directly labeled antibody were same as the control groups receiving no treatment at day 20. This was supported by hematological studies that clearly showed the negative effects of radiation on WBC and platelets counts in the 200  $\mu\text{Ci}$  group. Moreover, mice in the 125  $\mu\text{Ci}$  and 2 x 75  $\mu\text{Ci}$  pretargeted treatment groups showed reduced WBC and platelet counts, however they were less severe than the 200  $\mu\text{Ci}$  dose. At the same time, the 75  $\mu\text{Ci}$  dose was well tolerated and did not induce any blood toxicity (**Fig. 2.6**). Even though the kidneys received the highest organ dose, histopathological analysis of the kidneys revealed no acute tissue damage in 200  $\mu\text{Ci}$  and 75  $\mu\text{Ci}$   $^{212}\text{Pb}$ -DOTA-Tz pretargeted therapy groups (**Fig. 2.7**).

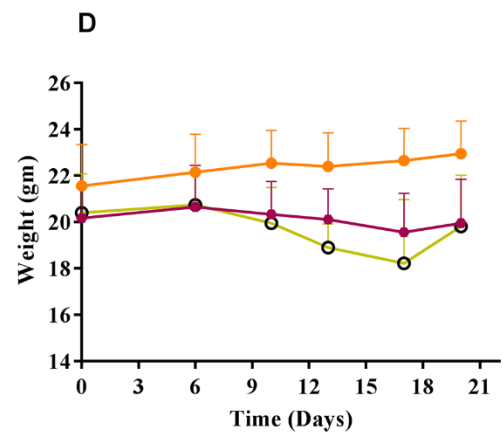
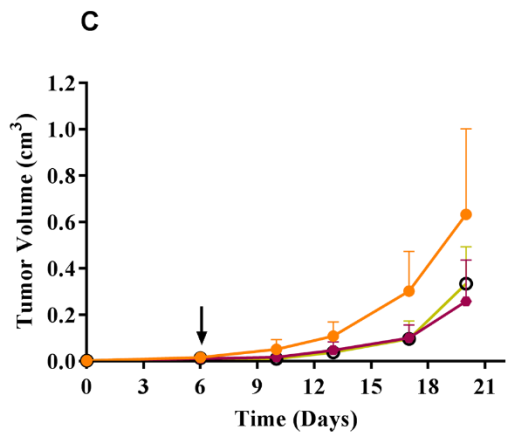
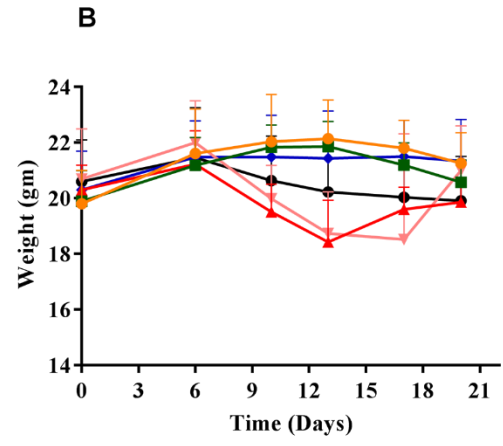
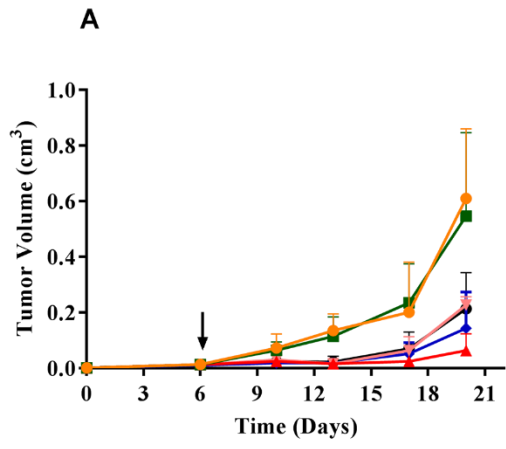


**Figure 2.4:** Plots of average tumor volumes (A, C) and average body weights (B, D) of each group of mice (n=8) during first 21 days of the PRIT studies. Mice bearing LS174T human colon carcinoma tumors were pretargeted with CC49-TCO mAb or RTX-TCO, two doses of clearing agent and  $^{212}\text{Pb}$ -DOTA-Tz. A  $^{212}\text{Pb}$ -TCMC-CC49 direct labeled mAb group was also included. In the first pretargeted therapy study, tumor volumes (A) and mouse weights (B) are reported for mice administered with PBS (—●—), CC49-TCO (—■—), CC49-TCO + 75  $\mu\text{Ci}$   $^{212}\text{Pb}$ -DOTA-Tz (—◆—), CC49-TCO + 200  $\mu\text{Ci}$   $^{212}\text{Pb}$ -DOTA-Tz (—▲—), RTX-TCO + 200  $\mu\text{Ci}$   $^{212}\text{Pb}$ -DOTA-Tz (—▼—) and a direct labeled  $^{212}\text{Pb}$ -TCMC-CC49 (15  $\mu\text{Ci}$ ) mAb control (—●—). In a second pretargeted therapy study, tumor volumes (C) and mouse weights (D) are reported for mice injected with PBS (—●—), CC49-TCO + 125  $\mu\text{Ci}$   $^{212}\text{Pb}$ -DOTA-Tz (—○—) and CC49-TCO + 2 x 75  $\mu\text{Ci}$   $^{212}\text{Pb}$ -DOTA-Tz (—◆—). Radioactive doses were administered (↓) 6 days post tumor inoculation, with an additional dose on day 13 for the multi-dose therapy group.

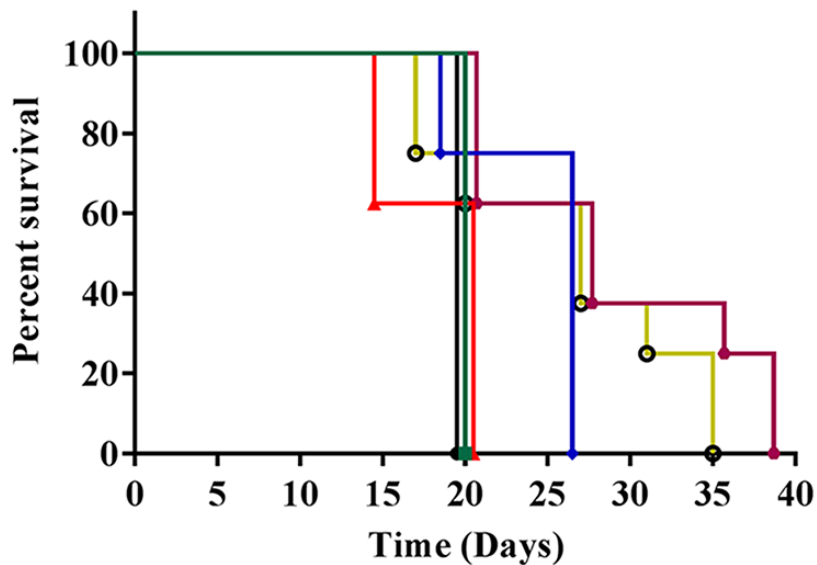


**Figure 2.5:** Kaplan-Meier survival curves. Mice bearing LS174T human colon carcinoma tumors were pretargeted with CC49-TCO mAb and treated with CC49-TCO (—■—), 75 μCi (—◆—), 125 μCi (—○—), 200 μCi (—▲—), and 2 x 75 μCi (—■—) of <sup>212</sup>Pb-DOTA-Tz. One group of mice was treated with directly labeled <sup>212</sup>Pb-TCMC-CC49 mAb (—●—). The PBS vehicle and non-radiolabeled CC49-TCO control groups were sacrificed on day 20 (data not shown). Treatment groups receiving 75 μCi (*P* = 0.03), 125 μCi (*P* = 0.02), and 2 x 75 μCi (*P* = 0.001) showed significant survival over vehicle control and direct labeled mAb

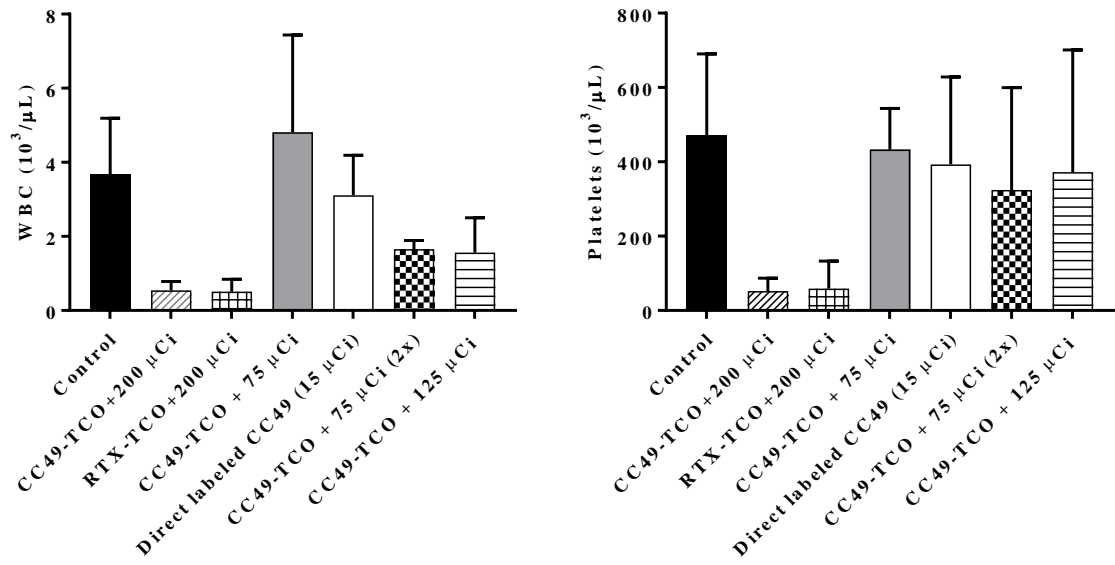


**Figure 2.6:** The effects of radiation-induced toxicity on (A) white blood cell counts, and (B) platelet counts.

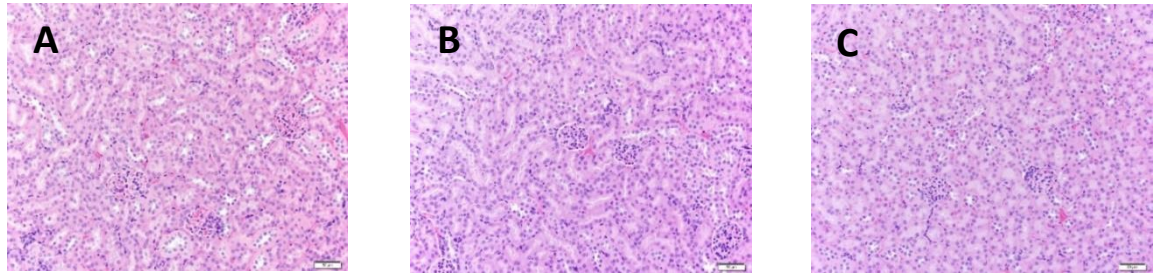


**Figure 2.7:** Kidney histology sections from (A) Untreated mice (PBS), and pretargeted mice treated with (B) 200 μCi and (C) 75 μCi of <sup>212</sup>Pb-DOTA-Tz.

## DISCUSSION

Two Tz based chelating systems, DOTA-Tz and TCMC-Tz (**Fig. 2.1**), were evaluated for their  $^{212}\text{Pb}$  radiolabeling efficiency, stability and tissue biodistribution. DOTA is one of the most widely used chelators and has been used in the clinical setting for number of radiometals.(114) TCMC was specifically designed to stably coordinate  $^{212}\text{Pb}/^{203}\text{Pb}$  under mild conditions necessary for labeling antibodies.(41) TCMC has shown favorable radiolabeling kinetics and in vivo stability with radiolabeled antibodies and was successfully used in a phase 1 clinical trial with trastuzumab.(44,45) Both DOTA-Tz and TCMC-Tz were radiolabeled with identical efficiencies and there was no significant difference in their serum stabilities. Similarly, both radiolabeled complexes exhibited rapid blood clearance with ~95% of the injected dose being cleared from the blood within 3 hours of injection (**Fig. 2.2A-B**). In contrast, the tissue distribution of  $^{212}\text{Pb}$ -DOTA-Tz and  $^{212}\text{Pb}$ -TCMC-Tz showed a marked difference in that there was a significant liver uptake of  $^{212}\text{Pb}$ -TCMC-Tz at 24 hours p.i. (**Fig. 2.2C-D**). This suggested that in addition to the kidneys, a significant portion of the  $^{212}\text{Pb}$ -TCMC-Tz dose was also excreted via hepatobiliary/gastrointestinal tract. This difference in liver uptake of two compounds was likely due to differences in charge and hydrophobicity of the two complexes. A slight increase in hydrophobicity due to the isothiocyanatobenzyl (SCN-Bz) group may have been responsible for the Tz-PEG<sub>10</sub>-SCN-Bn- $^{212}\text{Pb}$ -TCMC<sup>2+</sup> liver uptake. The positive charge of  $^{212}\text{Pb}(\text{TCMC})^{2+}$  would likely

contribute to increased non-specific kidney retention compared to the negative net charge of  $\text{Pb}(\text{DOTA})^{1-}$  complex.(41)

The biodistribution results in mice bearing LS174T color carcinoma tumors showed targeted tumor uptake and rapid clearance from the normal organs for both  $^{212}\text{Pb}$ -DOTA-Tz and  $^{212}\text{Pb}$ -TCMC-Tz (**Table 2.1**). The rapid clearance from the blood and normal organs led to moderately high tumor-to-normal tissue activity at 24 hours. This is particularly important in therapy as it allows administering higher radiation dose with minimal normal tissue toxicity. It is anticipated that greater tumor uptake and tumor/non-tumor ratios can be achieved by administering higher specific activity  $^{212}\text{Pb}$ -DOTA-Tz preparations. Purification of  $^{212}\text{Pb}$ -DOTA-Tz coupled with decreasing the mAb:Tz ratio from 1:10 to 1:2 as reported by Houston *et al.* should improve tumor localization and therapeutic efficacy.(32)  $^{212}\text{Pb}$ -TCMC-Tz was expected to have an equally favorable pharmacokinetic profile and in vivo stability in PRIT studies as well due to the success of  $^{212}\text{Pb}$ -TCMC-trastuzumab in clinical trials.  $^{212}\text{Pb}$ -TCMC-Tz showed almost double the tumor uptake than that of  $^{212}\text{Pb}$ -DOTA-Tz at 3 hours, however, tumor uptake was lower at 24 hours than  $^{212}\text{Pb}$ -DOTA-Tz. In addition, there was also a significantly higher liver and kidney uptake for  $^{212}\text{Pb}$ -TCMC-Tz at all times points compared to  $^{212}\text{Pb}$ -DOTA-Tz.

Apart from the tumor, the kidneys received the highest organ dose from  $^{212}\text{Pb}$ -DOTA-Tz (**Table 2.2**). A moderate dose to the kidneys was expected as  $^{212}\text{Pb}$ -DOTA-Tz clears from the body through kidneys. Moreover, it has been reported that approximately 30% of the  $^{212}\text{Bi}$  is released from the DOTA chelator

during decay from  $^{212}\text{Pb}$  to  $^{212}\text{Bi}$ .(115) The free  $^{212}\text{Bi}$  released from the tumor and other organs during this transition may also contribute to the kidney dose values. However, the rapid pharmacokinetics of  $^{212}\text{Pb}$ -DOTA-Tz yielded reduced residence time the kidneys, which minimized the total dose to the kidneys. This was further confirmed by the histopathological examination of kidneys, which showed no observable acute radiation toxicity in groups receiving 75  $\mu\text{Ci}$  and 200  $\mu\text{Ci}$  of  $^{212}\text{Pb}$ -DOTA-Tz (**Fig. 2.6**).

Based on radiation dose to tumor, liver and kidneys (**Table 2.2**),  $^{212}\text{Pb}$ -DOTA-Tz was selected as a choice of chelator system for the pretargeted therapy study. The pretargeted radioimmunotherapy studies were carried out according to the protocol described in **Fig. 2.3** where mice were treated with various doses (0, 75, 125, 200 and 2 x 75  $\mu\text{Ci}$ ) of  $^{212}\text{Pb}$ -DOTA-Tz. All the groups receiving PRIT displayed dose-dependent reductions in tumor growth rate, while the non-treatment control groups showed exponential tumor growth (**Fig. 2.4A, C**). All the treatment groups maintained an acceptable level of body weight (>80% of initial body weight) throughout the course of the study (**Fig. 2.4B, D**). Even though the 200  $\mu\text{Ci}$  therapy group showed the highest reduction in tumor growth rate, all the mice in that group were sacrificed on day 20 due to poor body score index and hematological radiation toxicity. This group displayed ~86% reduction in the WBC and platelets counts compared to the control group. Similar results were also observed in the group which was pretargeted with RTX-TCO and received a 200  $\mu\text{Ci}$  dose of  $^{212}\text{Pb}$ -DOTA-Tz. This indicated severe bone marrow toxicity due to the high radiation dose. Treatment groups receiving 125

$\mu\text{Ci}$  and 2 x 75  $\mu\text{Ci}$  doses of  $^{212}\text{Pb}$ -DOTA-Tz also displayed a drop in leukocyte counts, ~57 % and ~55% respectively, indicating moderate acute blood toxicity. In comparison, 75  $\mu\text{Ci}$   $^{212}\text{Pb}$ -DOTA-Tz dose was very well tolerated (**Fig. 2.6**) with little radiation associated toxicity.

A comparison of the treatment group receiving 75  $\mu\text{Ci}$   $^{212}\text{Pb}$ -DOTA-Tz dose in PRIT protocol to that of group receiving 15  $\mu\text{Ci}$  of directly labeled  $^{212}\text{Pb}$ -TCMC-CC49 in RIT protocol clearly displayed the advantages of the pretargeting therapy regimen. Pretargeting allowed at least 5 times higher dose administration with better tumor growth rate reduction and lower blood toxicity. The median survival of mice in the 75  $\mu\text{Ci}$  PRIT group (26 days) was statistically significantly higher ( $P = 0.05$ ) than control groups (20 days) (**Fig. 2.5**). The mice in the 125  $\mu\text{Ci}$  and 2 x 75  $\mu\text{Ci}$  therapy groups achieved better median survival times of 28 days ( $P = 0.02$ ) and 31 days ( $P = 0.001$ ) however they also exhibited transient hematological toxicity. Pretargeted  $\alpha$ -therapy's ability to control tumor growth is due to the radionuclide's decay properties, tumor marker heterogeneity and tumor size. LS174T is an aggressive tumor model with rapid tumor growth. However, the path length of  $\alpha$ - particle is very short and is not an ideal match for treating large solid tumors. Higher energy  $\beta$ -emitters, such as  $^{90}\text{Y}$  ( $t_{1/2} \sim 2.7$  days) or moderate energy emitter  $^{177}\text{Lu}$  ( $t_{1/2} \sim 6.6$  days) are likely to be better suited to treat large volume tumors.  $\alpha$ -particle radiation therapy is expected to be more effective in treating disseminated disease and micrometastatic disease.

## CONCLUSION

In summary, this study successfully establishes the therapeutic potential of in vivo pretargeted radioimmunotherapy employing  $^{212}\text{Pb}$ -labeled Tz-chelators and TCO-modified tumor targeting mAbs. The PRIT protocol allowed administration of 5-10 times the dose of the direct labeled RIT approach. Despite its complexities, pretargeted  $\alpha$ -particle therapy utilizing  $^{212}\text{Pb}$ -DOTA-Tz was effective in reducing tumor growth rate and reducing normal tissue toxicity, resulting in improved survival. These preclinical results underscore the potential use of the IEDDA pretargeted  $\alpha$ -therapy in the clinic.

## **CHAPTER 3**

### **MMP-12 As a Novel Tumor Target for PET/CT Imaging Using Phage Display Derived Antibody Fragments and Ultrasmall Silica Nanoparticles.**

## Introduction

Lung cancer remains the deadliest of all cancers for both men and women world-wide. The number of people dying of lung cancer is more than breast, prostate, and colon cancers combined. Lung cancer accounts for roughly 25% of all cancer related deaths in the United States. More than half of patients with lung cancer die within one year of diagnosis and the 5-year survival rate remains less than 20%. One of the main reasons for the high mortality rate associated with lung cancer is that by the time the disease is diagnosed, it is already metastasized and is at an advanced stage. Around 40% of newly diagnosed patients have a stage IV lung cancer.(121) The conventional methods for screening lung cancer include chest X-rays, low-dose computed tomography (LDCT), MRI scans, and FDG PET/CT scans. These methods are the mainstay of lung cancer detection and provide a non-invasive means for tumor detection. However, chest X-rays are not sensitive enough to detect lung cancer in early stages. While CT and MRI scans are more sensitive and can detect much smaller tumors, they have their own limitations. CT and MRI scans simply identify a structural abnormality and cannot differentiate between a benign mass and a malignant tumor. In almost all cases, further testing such as tissue biopsy is required to make the diagnosis. According to a recent large randomized trial, almost 96% of patients who tested positive by a CT scan screening exam did not result in lung cancer.(181) This significantly high false positive testing results in unnecessary, expensive, and more invasive tests. These findings indicate that

there is an urgent need to develop new biomarkers and diagnosis methods for early detection of lung cancer.

Matrix metalloproteinase-12 (MMP-12), which is also referred to as macrophage elastase or macrophage metalloelastase, was originally identified as elastase and is secreted by activated macrophages.(122) As the name suggests, MMP-12 mainly cleaves elastin in the extra cellular matrix (ECM), but it also degrades other ECM components like type IV collagen, fibronectin, fibrillin-1, laminin, entactin, vitronectin, chondroitin sulfate, and heparin sulfate proteoglycans.(123-125) It is secreted as a 54 kDa pro-enzyme which is subsequently activated by auto-cleavage of its 9 kDa propeptide domain. The role of MMP-12 has been clearly established in various lung diseases like chronic obstructive pulmonary disease (COPD) and emphysema, especially in response to cigarette smoking.(126) MMP-12 expression has also been associated with development, progression, and instability of atherosclerotic plaques.(127) Because of its role in inflammation, aneurism, and atherosclerosis, MMP-12 has been evaluated as a target for in vivo imaging using various molecular probes.(128-130)

Apart from macrophages, MMP-12 is also overexpressed by epithelial cells in lung adenocarcinoma and squamous cell carcinomas.(131,132) The overexpression of MMP-12 by epithelial tumor cells is correlated with more aggressive and invasive disease.(133) MMP-12 overexpression in non-small cell lung cancer (NSCLC) is associated with higher relapse rates and reduced patient survival.(134,135) MMP-12 up-regulation also promotes an emphysema

to lung adenocarcinoma transition.(136) The role of MMP-12 in lung cancer was further confirmed when Lv and coworkers showed that knockdown of MMP-12 inhibits cell proliferation and invasiveness of lung adenocarcinoma.(86). More recently, Ella *et al.* demonstrated that tumor-derived MMP-12 promoted tumor proliferation in the lungs. They also showed that MMP-12 secreted by tumor epithelial cells, not by activated macrophages, was responsible for cancer propagation.(85) All these findings suggest the potential of MMP-12 as a novel target for lung cancer diagnosis and treatment.

Phage display is a robust and proven technique that allows researchers to select target-specific antibodies against a variety of clinically relevant antigens from large antibody libraries. It involves incubating the antibody library with an immobilized target of interest, washing away unbound phages, and eluting the target bound phages. This process is repeated for a number of rounds to enrich for antibodies with high affinity for a specific target. Single-chain antibody fragments (scFvs), which consist of variable heavy (VH) and variable light (VL) chain domains linked by flexible linker, are powerful tools in research and clinical settings due to their superior pharmacokinetic properties compared to full-length mAbs. ScFvs retain the binding specificity of the parent full-length antibody while offering rapid blood clearance and better tissue penetration.

Even though small antibody fragments can achieve high-contrast imaging, they often suffer from poor tumor uptake and higher kidney and liver uptakes. This is mainly due to their very short *in vivo* half-lives and rapid whole-body clearance. One way to counter this problem is to conjugate scFv fragments to

nanoparticles to generate nano-immunoconjugates. Over the years, a diverse group of nanoparticles made up of various materials like silica, gold, magnetic or colloidal metals, liposomes, carbon nanotubes, and polymeric nanoparticles have been investigated for tumor targeting. These nanoparticles can be functionalized with various tumor specific ligands such as peptides, chemotherapeutic drugs, DNA/RNA aptamers, and small antibody fragments.(137-140) Because of their multivalent formats and longer biological half-lives, these nano-immunoconjugates often display better tumor uptake and tissue penetration compared to monovalent scFvs.

It was hypothesized that due to its role in lung cancer propagation, MMP-12 may serve as a novel diagnostic marker for lung cancer using in vivo PET imaging. In this study, antibody phage display methodology was used to identify MMP-12 specific scFv fragments. The antibody fragments would not only serve as imaging vectors but could also validate MMP-12 as a biomarker for lung adenocarcinoma. In order to identify MMP-12 specific antibody fragments, two rounds of scFv phage display selections were carried out against purified MMP-12 protein. The selected subpopulation of scFv library was further screened in vitro for MMP-12 specificity by ELISA, flow-cytometry, and fluorescence microscopy using MMP-12 expressing A549 human lung adenocarcinoma cells. The selected MMP-12 specific scFv clone with high binding affinity was subsequently conjugated with ultrasmall silica Cornell prime dot (or C' dot) nanoparticles using azide-DBCO click-chemistry. The C' dot-scFv construct was radiolabeled with  $^{89}\text{Zr}$  and injected in mice bearing A549 human lung

adenocarcinoma xenografts. The whole-body in vivo PET/CT images revealed that there was a specific and high accumulation of  $^{89}\text{Zr}$ -C'dot-scFv nano-immunoconjugate in the tumor with no kidney uptake at 48 hours post injection. Here, we clearly demonstrated the potential of MMP-12 as a novel diagnostic marker for lung adenocarcinoma and that MMP-12 specific scFv-nanoparticle conjugates could be used for non-invasive in vivo tumor imaging.

## Materials and Methods

### Phage Display Selection

Two rounds of solid-phase selections were carried out using the scFv library provided by Dr. John McCafferty.(65) For the first round of selection, 100 ng (100µl) of purified MMP-12 was coated onto the surface of a microtiter plate well (Nunc MaxiSorp™ plate) and blocked with 5% (w/v) skim milk powder in TBS. An aliquot of the McCafferty library (50 µl, 10<sup>12</sup> phages), pre-blocked in 3% (w/v) skimmed milk in TBS, was added to the coated well and incubated for 1 hour at room temperature. Unbound phages were washed away by rinsing the well 5 times with 0.1% Tween 20 (TBST) and 5 times with TBS. Bound phages were eluted in 100 µg/ml TPCK-treated trypsin for 15 minutes at room temperature. A mid-log culture of E.coli TG1 cells (5 ml) was added to the eluted phage and incubated for 1 hour at 37°C (250 rpm). Cells were centrifuged at 3000 x g for 10 minutes, resuspended in 200 µl of 2xTY media containing ampicillin and 2% glucose (2xTYAG), plated on 2xTYAG agar plates, and incubated at 30°C overnight. The next day, positively infected TG1 cells were scrapped from the surface of agar dishes, resuspended in 2xTYAG media, and incubated at 37°C in a shaker incubator until the OD<sub>600</sub> reached 0.5. Helper phage M13KO7 were added at a multiplicity of infection (MOI) of around 10 and incubated at 37°C for 1 hour. Cells were centrifuged at 4500 x g for 10 minutes, resuspended in 2xTYAK media (2xTY with ampicillin and kanamycin), and incubated at 30°C overnight in a shaking incubator (250 rpm). The following day, cells were spun down at 27000 x g for 15 minutes. The supernatant, which

contained secreted phages, was then used for the second round of the selection. To increase the stringency of the selection, the second round was carried out with a 10 times lower amount of MMP-12 protein (10 ng) than the first round. At the end of the second round, individual phage colonies were picked for screening by phage ELISA.

### **Primary Screening by Individual Phage ELISA**

Individual colonies picked after the selection were grown in 2xTYAG media at 37°C for 5-6 hours in a shaker incubator (120 rpm) in a 96 well plate. Once the OD<sub>600</sub> reached ~ 0.5, cultures were superinfected with helper phage at MOI of 10 and incubated at 37°C for 1 hour. Following incubation, the plate was centrifuged at 4500 x g for 10 minutes and supernatant was collected. Three Nunc MaxiSorp™ 96-well plates were coated with 10 µg/ml (100 µl) of MMP-12 protein and blocked with Rockland blocking buffer (Rockland Inc., PA) for 1 hour at room temperature. A separate set of three 96-well plates were coated with bovine serum albumin (BSA) as a negative control. Supernatants containing individual phage-scFvs were added to the MMP-12 and BSA coated plates and incubated for 1 hour at room temperature. After washing plates with 0.1% TBST for 5 times, an anti-M13-HRP conjugated antibody (1:2000 dilution) was added to the wells. This was followed by addition of HRP substrate 2,2'-Azino-bis(3-ethylbenzothiazoline-6-sulfonic acid) (ABTS) and the absorbance was measured at 405 nm using UV-Vis spectrophotometer plate reader. The scFv clones with highest signal-to-background ratios (MMP-12 : BSA) were selected for further analysis.

## Sequence Analysis of Positive Clones

A total of 23 phage clones with highest binding ratios of MMP-12 : BSA in the phage ELISA were selected for sequence analysis. These clones in pSANG4 phagemid were sequenced using forward primer M13 LeadSeq (5'-AAATTATTATTCGCAATTCCTTTGGTTGTTTCCT) and reverse primer NotMycSeq (5'-GGCCCCATTCAGATCCTCTTCTGAGATGAG). The clones were analyzed for the presence of full-length VH and VL inserts and their sequence similarities using Serial Cloner™ software. After sequence alignment, duplicate clones were removed and the remaining unique scFv clones were subcloned into the pSANG10-3F PET expression vector for soluble antibody production. The scFv genes were also analyzed for identification of complementarity determining regions (CDR), framework regions (FWRs), and immunoglobulin families using Kabat and Chothia databases.

## Expression and Purification of Selected scFv Fragments

The selected MMP-12 specific scFv clones with unique sequences were amplified by PCR using M13 LeadSeq and NotMycSeq primers. Purified PCR products were digested with *Nco*I and *Not*I restriction enzymes and subsequently ligated into the *Nco*I/*Not*I digested pSANG10-3F expression vector.(30) The ligated vector was used to transform chemically competent E.coli BL21 (DE3) cells by the heat shock method.

For the expression of scFv fragments, a single colony of transformed E.coli cells was picked and grown in 10 ml of 2xTYKG media (2xTY media with

kanamycin and 2% glucose) at 37°C overnight in a shaker incubator. The next day, 1L of 2xTYKG media was inoculated with the overnight culture and incubated at 37°C for 2.5-3 hours until the OD<sub>600</sub> reached 0.5-0.7. To induce the scFv expression, cells were pelleted at 4500 x g for 20 minutes, resuspended in 2xTY media (containing kanamycin and 1mM IPTG), and incubated at 30°C overnight (250 rpm). After overnight induction, cells were centrifuged at 4500 x g for 30 minutes, resuspended in 50 ml of ice-cold buffer 1 (100 mM Tris HCl pH 8.0, 20% (w/v) sucrose, and 0.5 mM EDTA), and incubated on ice for 30 minutes. The supernatant (periplasmic fraction) was collected after spinning down the cells at 27000 x g for 30 minutes. To initiate osmotic shock, the pellet was resuspended in buffer 2 (5 mM MgCl<sub>2</sub>, benzonase, and protease inhibitor cocktail) and incubated on ice for 20 minutes. Cells were pelleted at 27000 x g for 30 minutes and the supernatant (osmotic shock fraction) was collected. At this stage, both the periplasmic fraction and the osmotic shock fraction were pooled together and passed through a 0.2 µm filter.

Single-chain scFv fragments were purified by immobilized metal affinity chromatography (IMAC). Using a GE AKTA start FPLC system, a sample containing scFv was loaded on a 5 ml HisTrap™ HP Ni-column at a 3 ml/minute flow rate. Unbound impurities were removed with 10 column volumes of washing buffer (20 mM Tris-HCl, 500 mM NaCl, and 40 mM Imidazole; pH 8.0). The scFv was eluted by washing the column with elution buffer (20 mM Tris-HCl, 500 mM NaCl, and 250 mM Imidazole; pH 8.0). The scFv containing fractions were

pooled and the purity of the purified scFv was analyzed by SDS-PAGE and immunoblot.

### **ScFv-ELISA**

A Nunc MaxiSorp™ plate was coated with 100 µl (10 µg/ml) of MMP-12 protein overnight and blocked with Rockland blocking buffer for 1 hour at room temperature. The purified scFv antibodies (100 ng) were added to the blocked wells and incubated for 1 hour at room temperature. The plate was washed 5 times with 0.1% TBST before incubating with an anti-FLAG-HRP conjugated antibody for 1 hour at room temperature. After washing 5 times with 0.1% TBST, the binding was detected by addition of ABTS substrate and measuring the absorbance at 405 nm using a UV-Visible spectrophotometer plate reader. A plate coated with BSA was used as a negative control.

### **In Vitro Cell Binding Studies**

The A549 human lung adenocarcinoma cells and MDA-MB-231 human breast cancer cells were acquired from American Type Culture Collection. A549 cells were grown and maintained in F-12K medium supplemented with 10% fetal bovine serum, L-glutamine, and gentamycin. MDA-MB-231 cells were grown as a monolayer in RPMI 1640 media supplemented with 10% fetal bovine serum, L-glutamine, and gentamycin. Cell cultures were maintained at 37°C in a 5% CO<sub>2</sub> humidified incubator. For in vitro fluorescent cell binding studies, MMP-12 specific H12 scFv was conjugated with FITC-NHS dye using manufacturer's

instruction. An Anti-MMP-12 antibody conjugated to Alexa Fluor (ab200409, Abcam) was used as a positive control.

The binding characteristics of the purified H12-scFv to MMP-12 overexpressing A549 cells were assessed by flow cytometry. Cells ( $2 \times 10^5$  cells/tube) were fixed with 80% methanol for 5 minutes and permeabilized with 0.1% TBST for 20 minutes. Cells were then blocked with 5% BSA/TBS for 1 hour at room temperature. After washing 3 times with 1% BSA/TBS buffer, cells were incubated with FITC-labeled H12-scFv at 4°C for 1 hour in the dark. The binding was determined by measuring relative fluorescence intensities of the stained cells by CyAn ADP flow cytometer (Beckman Coulter) using the FITC channel. MDA-MB-231 cells, which do not express MMP-12, were used as a negative control.

For the fluorescence confocal microscopy, A549 and MDA-MB-231 cells were grown in chamber slides, fixed with 100% methanol (5 minutes), and permeabilized with 0.1% Triton X-100 for 5 minutes. The slides were blocked with 5% BSA/TBS for 1 hour at room temperature and subsequently washed with 1% BSA/TBS. This was followed by incubating slides with FITC-labeled H12-scFv at 4°C overnight. Next day, slides were washed and incubated with 4'-6-diamidino-2-phenylindole (DAPI) for 15 minutes at room temperature for nuclear staining. After additional washes, the samples were mounted under a cover-glass and analyzed on a Keyence fluorescent microscope.

## **Microscale Thermophoresis**

To determine the binding affinity of the H12-scFv towards purified MMP-12 protein, microscale thermophoresis (MST) technique was used. Here, 200 nM of H12-scFv (100  $\mu$ l) was incubated with 100 nM of NT-647 dye (100  $\mu$ l) for 30 minutes. The NTA containing dye binds specifically to the 6xHis-tag on the C-terminus of the scFv. Following dye incubation, 10  $\mu$ l aliquots of the labeled H12-scFv were taken and mixed with varying concentrations of MMP-12 protein (10  $\mu$ l) to make a dilution series. The resultant samples were loaded in microcapillaries and placed in the MST instrument for binding affinity determination.

## **Synthesis of C'dot-scFv immunoconjugate**

The DFO-DBCO-PEG-Cy5-C' dots were synthesized and purified as previously described.(141-143) To conjugate scFv fragments to DFO-DBCO-PEG-Cy5-C' dots, H12-scFv was first modified with NHS-PEG<sub>4</sub>-Azide. 2 mg of H12-scFv in PBS was incubated with 10 molar excess of NHS-PEG<sub>4</sub>-Azide (5 mg/ml in anhydrous DMSO). The pH of the reaction was adjusted to 9.0 using 1M carbonate buffer and the reaction was carried out for 1 hour at room temperature with agitation. Azide modified H12-scFv was purified using a PD-10 gel filtration column to remove unreacted NHS-PEG<sub>4</sub>-Azide.

Next, 12.5 nmols of DFO-DBCO-PEG-Cy5-C' dots were mixed with 5 molar excess of azide modified H12-scFv fragments and incubated for 24 hours at room temperature with continuous mixing. Unconjugated scFv-azide fragments

were removed by size-exclusion chromatography using HP Superdex 200 10/300 GL column. The purified C' dot-cFv containing fractions were pooled and concentrated using amicon-4 concentrator (10,000 Da MWCO) for further studies. The number of H12-scFv fragments on a single C' dot particle was determined by measuring the absorbance at 280 nm (scFvs) and 640 nm (C' dots).

### **Radiolabeling**

To radiolabel H12-scFv with  $^{67}\text{Ga}$  (Lantheus Medical Imaging, MA), antibody fragments were first conjugated with the bifunctional chelator NOTA-SCN. Briefly, 1 mg of purified H12-scFv was incubated with 10 molar excess of NOTA-SCN overnight at 4°C. The pH of the reaction mixture was adjusted to 9.0 with carbonate buffer. After the overnight reaction, excess NOTA-SCN was removed using a PD-10 column. For radiolabeling, 100 µg of scFv-NOTA was mixed with 1.0 mCi of  $^{67}\text{GaCl}_3$ . The pH was adjusted to 6.0 and the reaction mixture was incubated at room temperature for 30 minutes. This was followed by addition of 50 µl of EDTA (80 mM) and an additional incubation for 30 minutes at room temperature. The labeling yield was measured by instant thin layer chromatography (ITLC) using EDTA as a mobile phase. The unconjugated  $^{67}\text{Ga}$  was removed by PD-10 column purification and radiochemical yield was measured by ITLC.

For  $^{89}\text{Zr}$  labeling, 1.0 nmol of DFO-C' dot-scFv immunoconjugate was mixed with 1 mCi of  $^{89}\text{Zr}$ -oxalate (University of Wisconsin Cyclotron facility, WI) in HEPES buffer (pH 8) and incubated for 1 hour at 37°C. The reaction pH was

adjusted at 7.0-7.5. After 1 hour, 50  $\mu$ l of EDTA (80 mM) was added and incubated for an additional 1 hour at 37°C. The labeling yield was measured by ITLC using 10 mM diethylenetriaminepentaacetic acid (DTPA) as a mobile phase. Free  $^{89}\text{Zr}$ -oxalate was removed using a PD-10 column and the radiochemical purity was measured by ITLC.

### **A549 Lung Adenocarcinoma Xenograft Model**

All animal experiments were carried out in compliance with the Institutional Animal Care and Use committee in accordance with U.S. Public Health Service Guidelines. Athymic female BALB/C (*nu/nu*) mice were obtained from Envigo (USA) and inoculated with  $1 \times 10^7$  A549 cells in the right shoulder subcutaneously. Tumors were allowed to grow for 3-4 weeks and mice were used when tumors were clearly visible, palpable, and measurable.

### **In Vivo imaging**

For SPECT imaging, mice bearing A549 human lung adenocarcinoma xenografts were injected with 300  $\mu\text{Ci}$  of  $^{67}\text{Ga}$ -labeled H12-scFv via tail vein, and whole-body SPECT/CT images were taken 4 hours post injection. For  $^{89}\text{Zr}$  PET/CT imaging, mice bearing A549 xenografts were injected with 300  $\mu\text{Ci}$  of  $^{89}\text{Zr}$ -DFO-scFv-C' dots via I.P. injection. Small-animal PET/CT images were acquired 4, 24, and 48 hours after the injection under isoflurane anesthesia. Images were reconstructed using an ordered-subset expectation maximization 2-dimensional algorithm. For anatomical data fusion, small-animal CT was

performed, and concurrent images were reconstructed with Fanbeam filtered-backprojection algorithm.

## Results

### Phage Display Selection

The McCafferty scFv library, made up of  $1.1 \times 10^{10}$  clones, was used for solid-phase affinity selection (panning) to identify MMP-12 specific scFv fragments. To increase the stringency of the selection, the second round was carried out with a 10 times lower amount of MMP-12 than the first round. At the end of each round, the bulk of the output was spread on the agar plate and after overnight growth at 37°C, single colonies were picked to calculate the selection output and the enrichment ratio. The selection output of round I and II was  $3.1 \times 10^4$  and  $1.95 \times 10^5$  colony forming units (cfus), respectively, with an estimated enrichment ratio of about 6.3. It may be possible to achieve higher enrichment by performing more rounds of selections, but that would also increase the chances of amplifying fast-growing phage clones which may have lost their pIII-scFv fusion gene. Due to the use of trypsin-cleavable M13 helper phage in this study, only 2 rounds of selection were required instead of the usual 3-4 rounds. The use of this engineered helper phage and trypsin treatment greatly reduces the population of “bald” phages, which do not display antibodies on their surface.

### Phage ELISA

Following two rounds of selections, 96 individual phage colonies were picked for the phage ELISA screening. The relative binding specificities of selected clones were determined by comparing phage-scFv binding to MMP-12 verses BSA. Out of 96 clones, 23 clones had MMP-12 : BSA binding ratios of  $\geq$

5. These 23 clones with the highest MMP-12 specificities were selected and sequenced by Sanger sequencing (**Fig. 3.1**). The sequence alignment revealed that out of 23 selected clones, 8 clones had unique sequences and these 8 scFv clones were chosen for further characterization (**Table 3.1**).

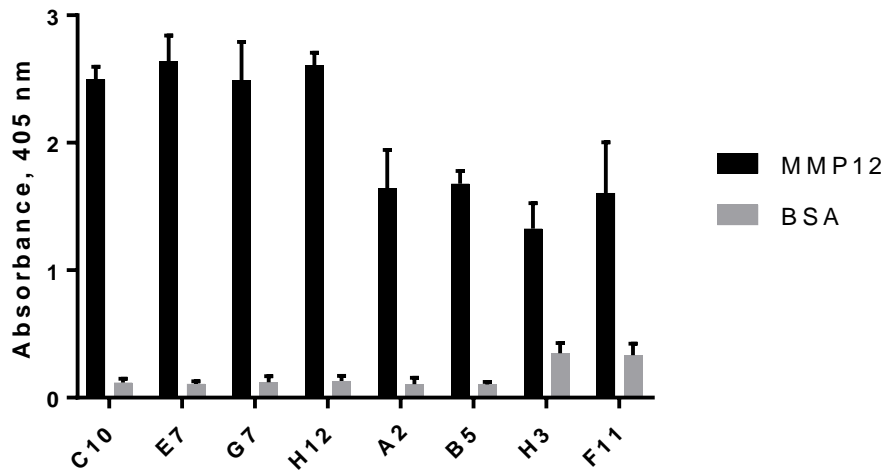


**Figure 3.1:** Phage ELISA: Following two rounds of selection against purified MMP-12 protein, the binding specificities of individual phage-scFv clones were determined by phage ELISA in a 96 well plate. The individual phage-scFv clones were added to 96-well plates coated with MMP-12 or BSA. After washing non-specific binders, the bound phage-scFvs were detected using an anti-M13-HRP conjugated secondary antibody. The 8 phage-scFv clones represented in the figure displayed highest specificities towards MMP-12 over BSA. Each bar represents average of 3 replicates.

**Table 3.1:** Sequence analysis of MMP-12 specific antibody fragments

ScFv clone	CDR-H1	CDR-H2	CDR-H3	CDR-L1	CDR-L2	CDR-L3
H12	SYTIS	IIPILGIANYAQK	GVVEGSGAFDI	TRSRGSIASHYVQ	LEDDQRP	QSYDSSNVV
C10	SYTIS	IIPILGIANYAQK	DRFEGAIFDY	TRSSGSIASNYVQ	FEDNQRP	QSYDSSNVV
E7	SYTIS	IIPILGIANYAQK	DRPYIYGMDV	KSSQNVLDSSNMNYLG	YWASTRE	QQYYSPVVT
G7	SYTIS	IIPILGIANYAQK	AGYDSSGYSYFDY	RSSQSLVYVDGDTYLN	YRVSNRD	MQGTHWPPT
A2	SYTIS	IIPILGIANYAQK	DGGNDFDY	TGSSSNIGSTYDVH	FGNTNRP	QSYDDSLSAFV
B5	SYTIS	IIPILGIANYAQK	SQTTVTSGGAFI	RSSQSLVHSNGYTYLN	YKVSNRD	MQGTHWPPT
H3	SYTIS	IIPILGIANYAQK	ERTYDNYGMDV	TRSSGSIASNYVQ	YEDNQRP	QSYDSSNQV
F11	SYTIS	IIPILGIANYAQK	DGSSWHRYMDV	TRSQSISSYLN	YEDQNRP	QSYDSTTVVT

## ScFv Expression and Purification

The McCafferty scFv library used in this study was constructed in the pSANG4 phagemid (**Fig. 3.2A**). Even though it is possible to express soluble scFvs from this phagemid, the yield is poor. Thus, to express large quantities of soluble scFvs, the antibody genes were subcloned into the pSANG10-3F PET expression vector. Here, expression of scFv gene is under the T7 promoter and it also fuses the scFv antibody to a C-terminal His-tag and a tri-FLAG tag for easy purification and detection. The pSANG10-3F expression vector also has an N-terminal pelB leader sequence which exports scFvs into the bacterial periplasm for disulfide bond formation and proper folding (**Fig. 3.2B**). Following the subcloning of scFv genes into the pSANG10-3F vector, resultant plasmids were transformed into the E.coli BL21 (DE3) cells and scFv fragments were expressed by IPTG induction. Osmotic shock was used to extract scFvs out of the periplasm, which were then purified using the Ni-affinity chromatography. The SDS-PAGE analysis showed a single band at around 30 kDa for each scFv, which is the predicted mass of scFv antibodies. The expression of scFvs was furthered verified by immunoblotting using an anti-FLAG-HRP conjugated monoclonal antibody which confirmed the successful expression and purification of scFvs (**Fig. 3.3**).

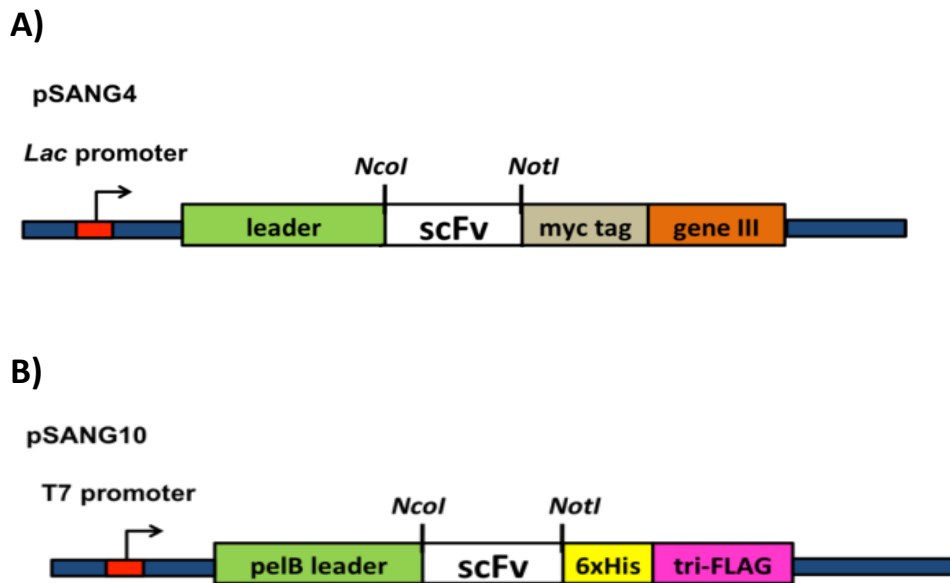
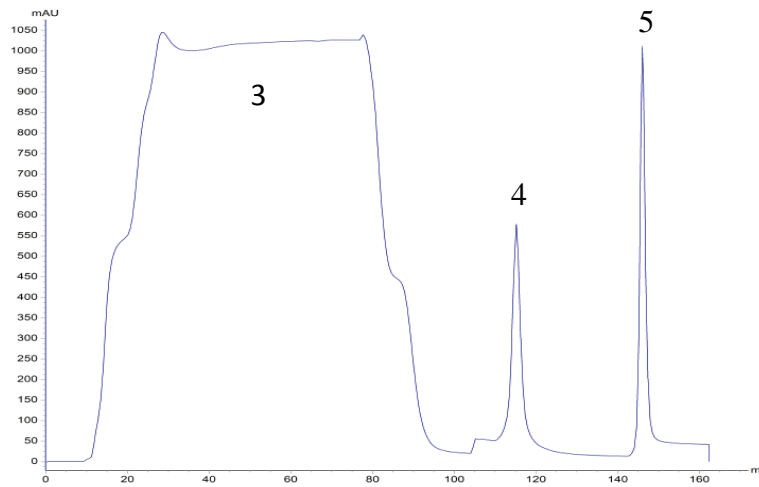


**Figure 3.2:** Expression vectors: Schematic representation of A) pSANG4 phagemid used for the McCafferty scFv library construction, and B) pSANG10-3F vector used to express soluble scFvs in *E.coli*. (Adopted and modified from Schofield *et al.*, (2006))

**A**



**B**

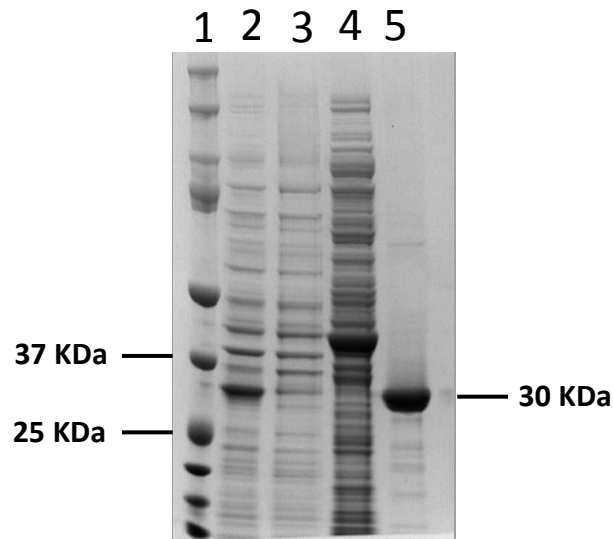


**Figure 3.3:** Expression and purification of the H12-scFv: The H12-scFv was expressed and purified from E.coli periplasm using a Ni-column. A) Chromatographic profile of the purification of H12-scFv using a Ni HiTrap column on AKTA Start system. B) Coomassie blue staining of SDA-PAGE gel; Lane 1- Molecular weight markers, Lane 2- Loading sample, lane 3 – Flow through, lane 4 – Washing (40 mM Imidazole), and lane 5 - Elution (250 mM Imidazole)

## ScFv-ELISA

In order to confirm the results of the phage scFv ELISA and MMP-12 specificities of the selected clones, a secondary binding assay was performed with soluble scFv antibodies. Each of the 8 selected clones were subjected to ELISA with MMP-12 as a target antigen and BSA as a negative control. As shown in **Fig. 3.4**, all 8 scFv clones maintained their MMP-12 binding affinities and specificities with minimum binding to BSA. This assay illustrated that purified scFvs retained their MMP-12 specificities in their soluble form.

## In Vitro Cell Binding Studies

A flow cytometry analysis was performed with MMP-12 expressing A549 human lung adenocarcinoma cells to determine the cell-binding characteristics of the selected scFv fragments. The human breast cancer cell line MDA-MB-231 was used as a negative control. Cells were permeabilized by detergent treatment and incubated with FITC-conjugated H12-scFv antibody fragments. A total of 10,000 cells were counted for each cell line and the relative fluorescence intensities were measured by flow cytometry. As shown in **Fig. 3.6**, the mean fluorescence intensity (MFI) of FITC-labeled H12-scFv with A549 cells was  $153 \pm 68$ , while the MFIs for MDA-MB-231 and the unstained A549 cells were  $4.0 \pm 1.0$  and  $3 \pm 1$ , respectively. These observations demonstrated that the selected H12-scFv could specifically recognize MMP-12 on A549 lung carcinoma cells. Commercially available anti-MMP-12 antibody was used as a positive control which had the MFI of  $55 \pm 14$  with A549 cells.

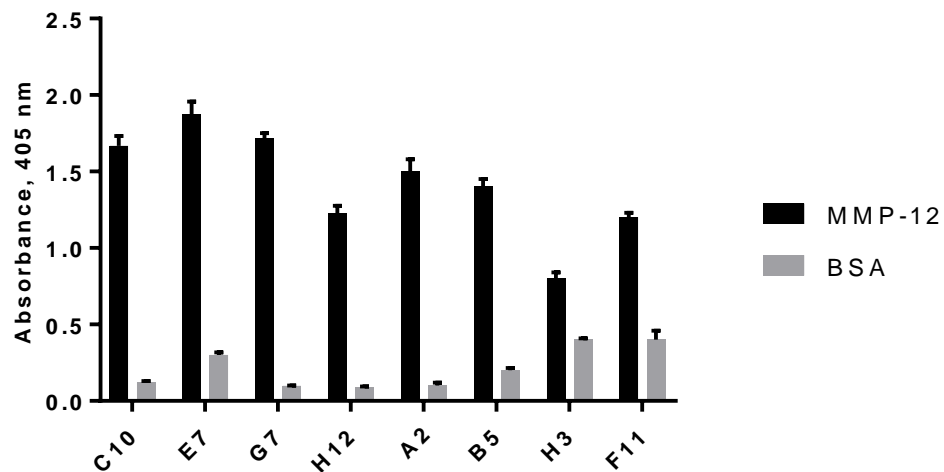


**Figure 3.4:** Soluble scFv ELISA: The binding specificities of soluble scFv fragments were determined by incubating 100 ng of purified scFv fragments in wells coated with either purified MMP-12 or BSA. After the washing step, wells were incubated with an anti-FLAG-HRP conjugated secondary antibody and the binding was detected by measuring absorbance at 405 nm. Bars represent the average of 3 replicates.

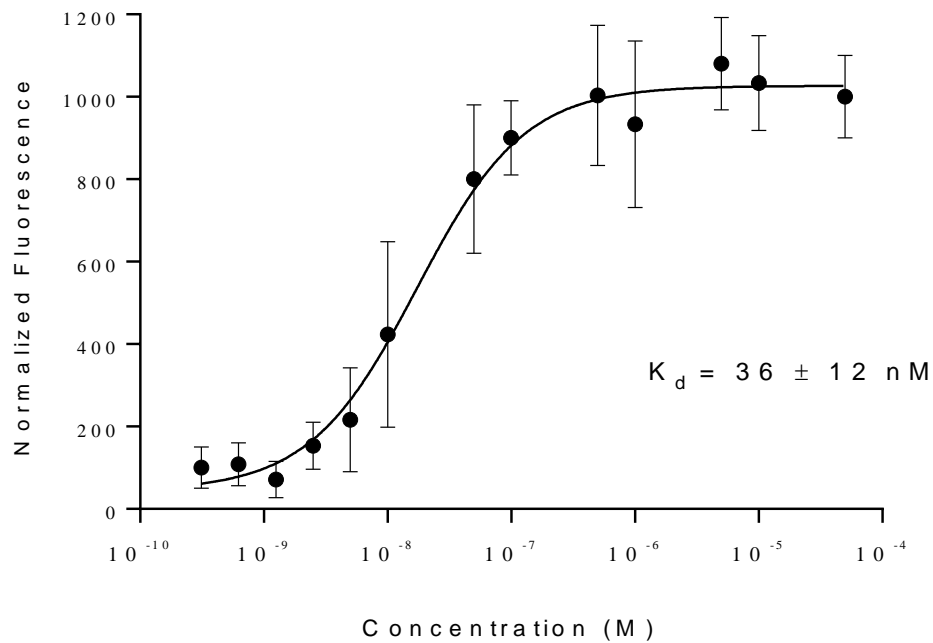


**Figure 3.5:** Binding affinity of the H12-scFv to purified MMP-12 protein was determined by the microscale thermophoresis (MST). The H12-scFv was fluorescently labeled with NTA-dye. Serial dilutions were prepared by keeping the concentration of the H12-scFv constant while changing the MMP-12 concentration.

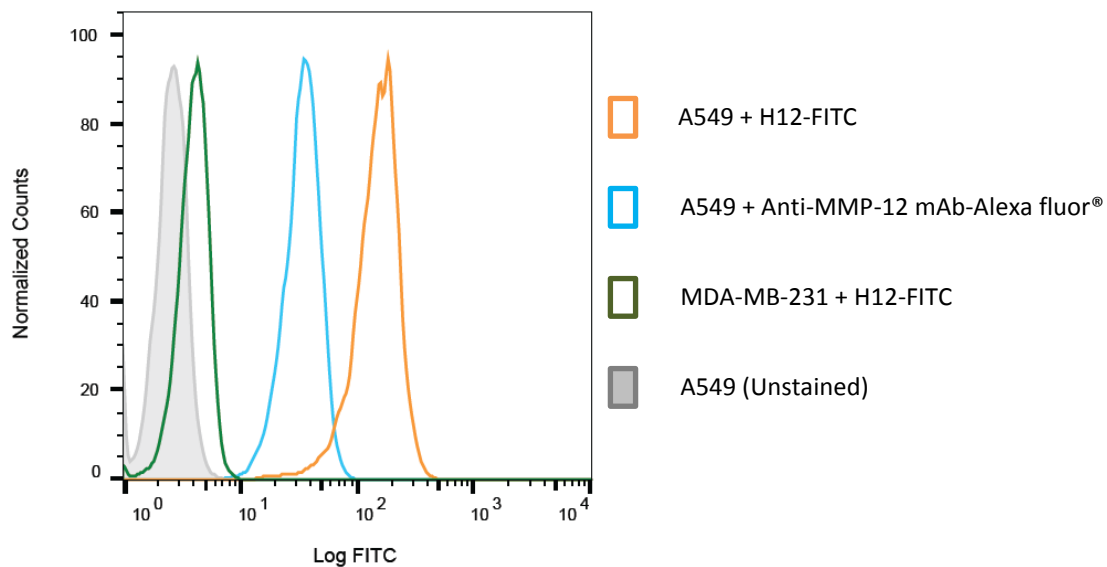


**Figure 3.6:** Flow cytometry analysis was carried out to assess the binding characteristics of the H12-scFv to MMP-12 overexpressing cell line A549. Cells ( $1 \times 10^5$ ) were fixed in 80% methanol and permeabilized with 0.1% TBST for 20 minutes. After blocking cells with 5% BSA/TBS for 1 hour, cells were incubated with FITC-conjugated H12-scFv for 1 hour on the ice. Next, cells were washed and binding was determined by counting 10,000 cells in CyAn ADP flow cytometer. MDA-MB-231 cells and unstained A549 cells were used as negative controls. An Anti-MMP-12 antibody conjugated to Alexa Fluor (ab200409, Abcam) was used as a positive control.

To visualize scFv binding and specificity to A549 cells, fluorescent microscopy was carried out using FITC-labeled H12-scFv. Similar to flow cytometry, FITC-labeled H12-scFv bound to MMP-12 positive A459 cells (**Fig. 3.7**).

### **Synthesis of C' dot-scFv Immunoconjugates**

The C' dot nanoparticles have a silica core with embedded Cy5 dye. Their surface is coated with PEG chains to make them more hydrophilic. A portion of these PEG chains can be modified further with different functional groups like DFO and DBCO. The DFO-DBCO-PEG-C' dots were synthesized in a multi-step procedure as described previously.(141,142) The C' dot nanoparticles used in these studies had a hydrodynamic diameter (HD) of 5.3 nm. (**Fig. 3.8**). The DFO-DBCO-PEG-C' dots were conjugated with azide-modified scFvs using azide-DBCO click chemistry.(143) After incubating azide modified H12-scFv with DBCO functionalized C' dots for 24 hours at room temperature, the unconjugated scFvs were removed by size exclusion chromatography in 50 mM HEPES buffer. By measuring the UV absorbance of C' dots at 640 nm and of scFvs at 280 nm, it was determined that there were an average of 2.4 scFv molecules attached to each C' dot nanoparticle.

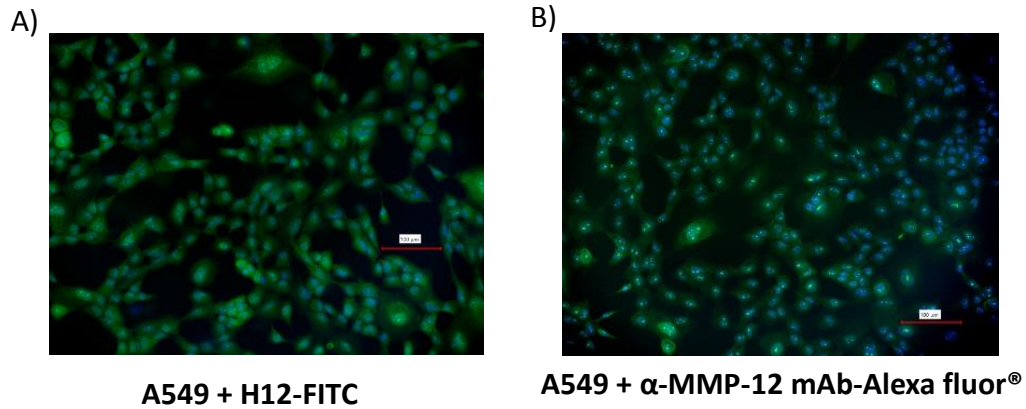


**Figure 3.7:** Fluorescence microscopy analysis of cell binding: A549 cells were grown and fixed on the microscope slides. Cells were permeabilized with 0.1% Triton X-100 and blocked with 5% BSA/TBS. This was followed by incubating cells H12-FITC scFv overnight at 4°C. Images were taken the next day using a fluorescent microscope. A) An Image with H12-FITC scFv displaying the strong binding of the H12-scFv to MMP-12 positive A549 cells. B) An image with a commercially available anti-MMP-12 mAb binding to A549 cells as a positive control.

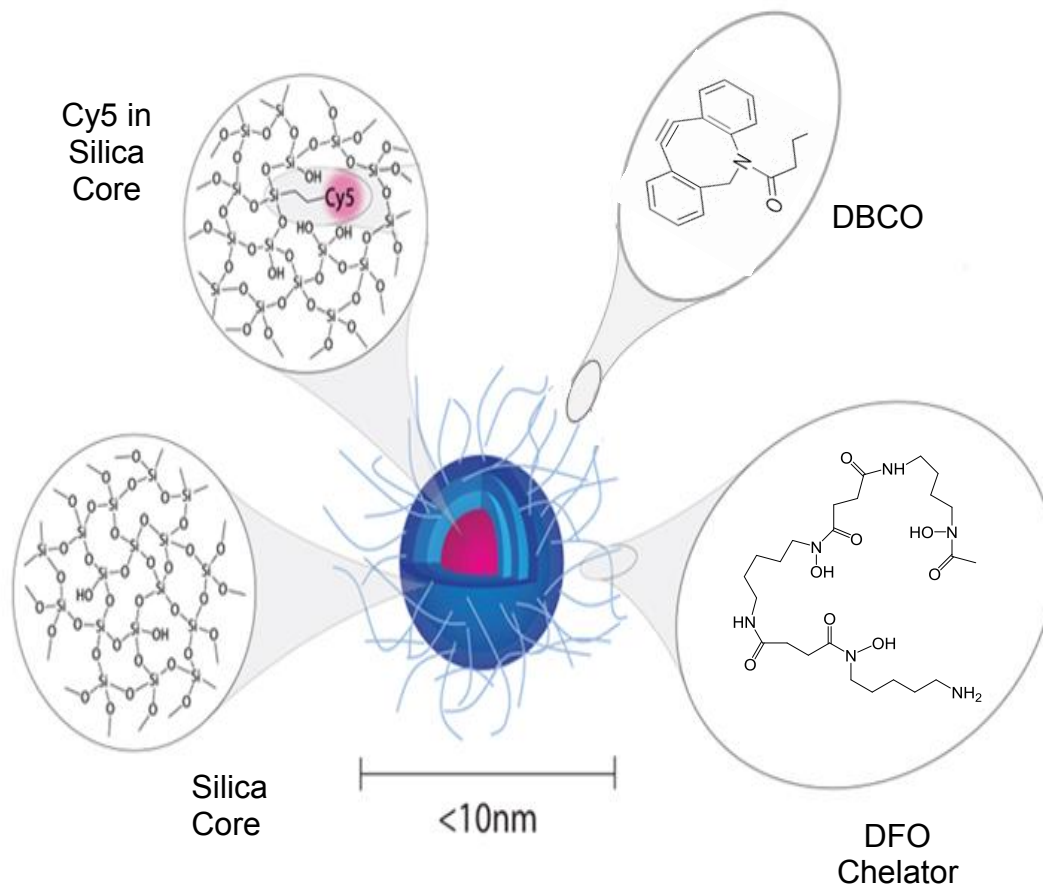


**Figure 3.8:** A schematic of the Cornell prime (C' dot) nanoparticles: The C' dot nanoparticles have a silica core with embedded Cy5 fluorophore. The surface of the C' dot is covered with PEG chains to make C' dot particles more hydrophilic. The C' dot nanoparticles were further modified with DFO chelators and DBCO functional groups. The hydrodynamic diameter of DFO-DBCO-C' dot nanoparticle was ~5.3 nm.

## In Vivo Imaging

The imaging capability of the direct labeled  $^{67}\text{Ga}$ -H12-scFv was investigated in mice bearing A549 lung adenocarcinoma xenografts. Whole-body SPECT/CT images were acquired 4 hours following the injection of  $^{67}\text{Ga}$ -H12-scFv. Images revealed a clear tumor uptake of radiolabeled scFvs. Unfortunately, it also demonstrated high kidney and liver uptake. The high liver and kidney uptake of radiolabeled antibody fragments with C-terminal 6xHis tag is consistent with previous studies (**Fig. 3.9**). (173-175)

To Investigate the tumor targeting efficiency of scFv-conjugated nanoparticles, the DFO-C' dot-scFv construct was radiolabeled with  $^{89}\text{Zr}$  and injected in mice bearing A549 xenografts. PET/CT images were acquired 4, 24, and 48 hours after the injection of  $^{89}\text{Zr}$ -C'dot-H12-scFv nano-immunoconjugate. Images at 4 hours post injection showed that the radiolabeled particles were circulating throughout the body and there was no observable tumor uptake, however at 24 hours the specific tumor uptake of the particles was evident. There was still a significant amount of activity in the heart indicating that the particles were still circulating in the body. At 48 hours post injection, high accumulation of  $^{89}\text{Zr}$ -labeled C' dot-scF nanoparticles in the tumor was observed (**Fig. 3.10**). There was a little uptake in the liver which indicated that a small amount of  $^{89}\text{Zr}$ -C' dot-H12-scFv nanoparticle was getting cleared out of body via liver. There was no non-specific uptake in any other major body organ. Most importantly there was no kidney uptake at any time points. This result indicated that the high kidney and liver retention observed in  $^{67}\text{Ga}$ -H12-scFv SPECT/CT image was

likely due to positively charged amino acid on the C-terminal tail of the scFv.(173-175)

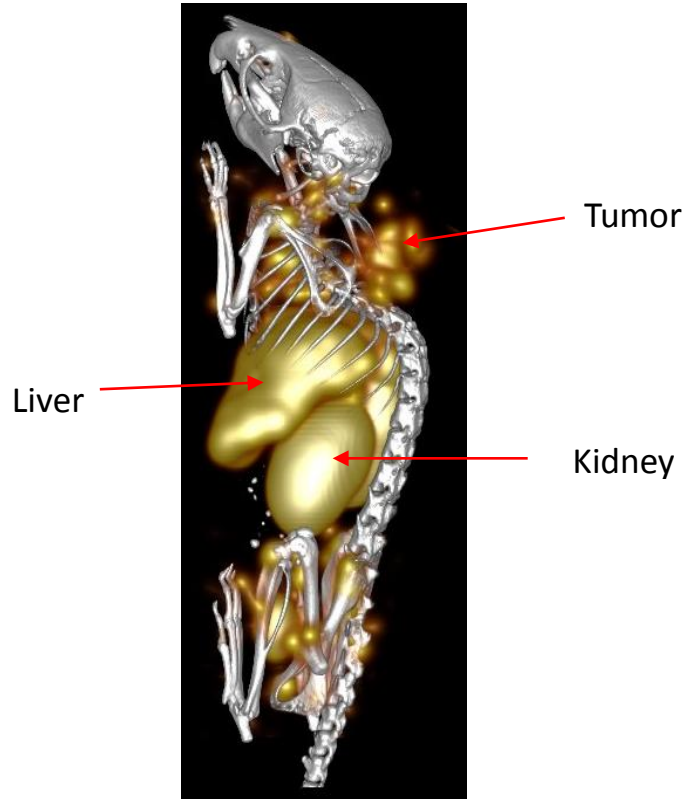


**Figure 3.9:** In vivo SPECT/CT imaging: An A549 tumor bearing mouse was injected with 300  $\mu\text{Ci}$  of  $^{67}\text{Ga}$ -labeled H12-scFv via tail vein injection. The whole body SPECT/CT image was acquired 4 hours post injection. An analysis of the image revealed that the radiolabeled H12-scFv bound to the tumor, however there was also a significant accumulation of H12-scFv in the liver and kidneys.

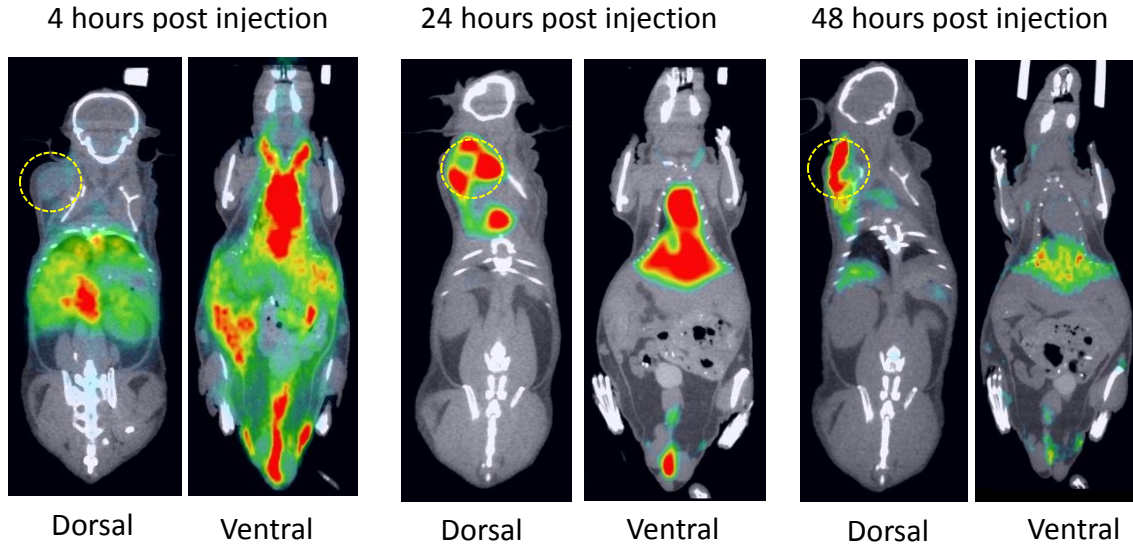


**Figure 3.10:** In vivo PET/CT imaging: The H12-conjugated C' dot nanoparticles were radiolabeled with  $^{89}\text{Zr}$  (300  $\mu\text{Ci}$ ) and injected in mice bearing A549 xenografts by I.P. Injection and whole-body PET/CT images were taken 4, 24, and 48 hours post injection. There was a significant accumulation of  $^{89}\text{Zr}$ -C' dot-scFvs in the tumor at 48 hours with no kidney retention and very minimal liver uptake. This image clearly demonstrated that the ultras-small C' dot-H12 nano-immunoconjugate exhibited higher tumor uptake and superior pharmacokinetics compared to the direct labeled-H12 scFvs. Dotted yellow circle indicates the tumor.

## Discussion

Lung cancer is by far the leading cancer killer in both men and women, accounting for nearly 1.7 million deaths world-wide. One of the main reasons for this high mortality rate is the lack of sensitive early diagnosis methods. It is critically important to detect lung cancer in its early stages, as the survival rate goes down drastically as the disease progresses to advanced stages. Here, we describe the development of a targeted imaging agent against MMP-12 for in vivo PET/CT imaging in A549 human lung adenocarcinoma tumor model. The MMP-12 specific construct would not only be used for initial diagnosis, but could also play an important role in treatment planning and post treatment response assessment. Various MMP-12 specific probes have been used for imaging aneurysms and atherosclerotic plaques, but to date MMP-12 has not been investigated as a molecular target for radioimaging in lung cancer. In this study, we successfully identified an antibody fragment that specifically targeted MMP-12 antigen in lung cancer. To the best of our knowledge, this is the first in vivo study establishing MMP-12 as a novel target for human lung adenocarcinoma using PET/CT imaging in a mouse xenograft model.

To identify MMP-12 specific antibody fragments (scFvs), phage display selections were carried out against MMP-12 protein. Using a standard affinity-selection method, two rounds of selections were performed, and individual phage clones were picked at the end of the second round. A total 96 were selected and screened for MMP-12 specificity using BSA as a non-specific control target. Out of 96 phage-scFv clones, 23 clones displaying highest binding signals over BSA

(MMP-12 : BSA  $\geq$  5) were selected and sequenced by Sanger sequencing to identify duplicate clones. The sequencing analysis revealed that out of 23 clones, 8 clones had unique CDR sequences. Surprisingly, all 8 unique clones had the identical CDR-H1 and CDR-H2 sequences, but they all differed in their CDR-H3 regions (**Table 3.1**). No discernable pattern in their light chain CDR sequences was observed. This result indicated that the selection was convergent towards a common sequence motif and that the library was specifically enriched towards MMP-12. The selected phage-scFv clones were subsequently subcloned into pSANG10-3F vector for expression and purification of soluble scFvs. ELISA was carried out to ascertain that the purified scFvs in soluble form retained their MMP-12 specificity. In the phage ELISA binding studies, the scFv is connected to a huge phage particle that might bind non-specifically to the target resulting in false positives. By repeating the ELISA with soluble scFvs, we can confirm that the binding signal observed was due to specific interaction between scFvs and the target protein. ELISA performed with soluble scFvs confirmed that all selected 8 clones were MMP-12 specific, as the binding signal for MMP-12 was at least 5 times higher than that of the negative control BSA (**Fig. 3.3**).

Based on the specificity towards MMP-12 as well as the purification yield, scFv clone H12 was selected for further characterization. The microscale thermophoresis analysis revealed that H12-scFv bound to purified MMP-12 protein with the binding affinity ( $K_d$ ) of  $36 \pm 12$  nM (**Fig. 3.5**). The H12-scFv was further characterized in vitro to determine if it could detect MMP-12 in A549 human lung adenocarcinoma cells. The A549 cell line was reported to

overexpress MMP-12 and was used as a target cancer cell line, while human breast cancer cell line MDA-MB-231 was used as a negative cell line since it does not express MMP-12. Also, MDA-MB-231 cells overexpress membrane bound MMP-14 (MT-1 MMP). Therefore, not only does MDA-MB-231 serve as a negative control for MMP-12 expression, but it also helps to determine if H12-scFv can discriminate between MMP-12 and MMP-14. The flow cytometry analysis showed that H12-scFv bound specifically to MMP-12 expressing A549 cells and did not bind to MDA-MB-231 cells (**Fig. 3.6**). Surprisingly H12-scFv showed a much higher binding signal to A549 cells than the commercially available anti-MMP-12 antibody. The specific binding of H12-scFv to A549 cell was further confirmed by fluorescent microscopy. Again, the H12-scFv did not bind to the MDA-MB-231 cells, which affirmed that H12-scFv could recognize MMP-12 in cell binding assays and also distinguish between MMP-12 and MMP-14 (**Fig. 3.7**). The specificity of H12-scFv towards MMP-12 and its nanomolar affinity were sufficient to further investigate its usefulness as an in vivo radioimaging agent.

Radiolabeling of H12-scFv for in vivo imaging was accomplished by conjugating scFvs with bifunctional chelator *p*-SCN-Bn-NOTA and subsequently labeling with <sup>67</sup>Ga. The <sup>67</sup>Ga-H12-scFv was injected in A549 tumor bearing mice. The in vivo SPECT/CT images showed that there was a moderate tumor uptake for the <sup>67</sup>Ga-labeled H12scFv at 4 hours post injection. Unfortunately, there was also a significant non-tumor uptake of H12-scFv in the liver and kidneys (**Fig. 3.9**). Because of their smaller size and rapid body clearance via kidneys, scFvs

usually have a higher kidney uptake compared to the full length antibodies. This problem was compounded by the fact that scFvs expressed using pSANG10 vector has a C-terminal 6xHis-tag. At a physiological pH, these histidine residues are positively charged and bind to negatively charged proximal tubule cells of the kidneys resulting in high kidney uptake. The presence of 6 histidine residues as well as lysine residues in the tri-FLAG tag also lead to higher liver uptake as observed in the in vivo SPECT image with  $^{67}\text{Ga}$ -H12-scFv.(173-175) There are various ways to reduce the liver and kidney uptakes of vectors with histidine tags. It has been shown that modifying the HHHHHH tag to the HEHEHE tag leads to considerable less uptake in kidney and liver.(175,176) So does the administration of positively charged amino acids like lysine or arginine just before the injection of radiolabeled vector with 6xHis-tag.(179,180) In this study, we conjugated scFvs to the ultrasmall silica nanoparticles which resulted in no kidney uptake and significantly lower liver retention.

Cornell prime (C' dot) ultrasmall nanoparticles were designed with a Cy5 fluorophore embedded silica core. These particles have a hydrodynamic diameter in the range of 5-7 nm. The silica core particles are coated with PEG chains to make them more hydrophilic which in turn reduce non-specific uptake in liver, spleen, and other body organs. Because of their small size and hydrophilic properties, the C' dot nanoparticles excrete through the body via kidneys with no kidney retention.(141-143) These C' dot nanoparticles have been functionalized with various tumor targeting peptides for successful in vivo tumor imaging with superior tumor targeting and high tumor-to-background ratios. (144-

146) Because of their non-toxic nature, favorable biodistribution profile, and higher tumor targeting, the C' dot nanoparticles are approved by the FDA for clinical trials and have been used successfully for in vivo PET imaging in patients with metastatic melanoma.(147)

The C' dot nanoparticles used in this study were synthesized and provided by the Michelle Bradbury and Ulrich Wiesner groups.(143) These nanoparticles were functionalized with DBCO and DFO groups and had hydrodynamic diameter of 5.3 nm (**Fig. 3.8**). Using azide-DBCO click-chemistry, H12-scFv was conjugated to the C' dot particles with approximately 2.4 scFvs per particle. The scFv-conjugated C' dots were radiolabeled with  $^{89}\text{Zr}$  and injected in mice bearing A549 xenografts. The in vivo PET/CT imaging demonstrated a high tumor specific uptake for  $^{89}\text{Zr}$ -C' dot-H12-scFv nano-immunoconjugates at 48 hours post injection (**Fig. 3.10**). Unlike the direct labeled  $^{67}\text{Ga}$ -scFv construct, there was no kidney uptake and a very little to moderate liver uptake. This clearly demonstrated that the ultras-small silica nanoparticles functionalized with single-chain antibody fragments could be used successfully as an in vivo imaging agent with superior tumor targeting and efficient renal clearance. Also, this study established MMP-12 as a novel target for lung adenocarcinoma diagnosis with the potential be explored as a therapeutic target.

## Conclusion

In summary, this project was aimed at discovering MMP-12 specific antibody fragments for in vivo radioimaging. The growing evidence suggests that MMP-12 is involved in lung adenocarcinoma tumor growth and metastasis. Given the lack of a MMP-12 specific tumor targeting probes, we decided to investigate if MMP-12 has the potential as a novel biomarker for lung cancer diagnosis. Using the McCafferty scFv library, MMP-12 specific antibody fragments were selected and characterized in vitro. The in vivo SPECT/CT imaging using direct labeled  $^{67}\text{Ga}$ -scFv demonstrated moderate tumor uptake. Even though this construct showed promise, it had a limited feasibility as potential imaging agent due to very high kidney and liver uptake. In sharp contrast, PET/CT imaging with  $^{89}\text{Zr}$ -labeled C' dot-scFv construct displayed a very high MMP-12 specific tumor uptake and no kidney retention in the A549 xenograft model. Additionally, there was no non-specific binding of the probe in any other major organ except for a little uptake in the liver. The C' dot-scFv nano-immunoconjugates provided a better imaging tool due to their higher tumor retention and better pharmacokinetic profile than the direct labeled antibody fragments. These observations clearly demonstrated that MMP-12 is an attractive new target for lung adenocarcinoma diagnosis as well as therapy.

## Future Studies

Since the in vivo PET/CT imaging with  $^{89}\text{Zr}$ -labeled C' dot-scFv nano-immunoconjugates yielded positive results, the next step would be to study the biodistribution profile of this construct to quantify the uptake in the tumor and normal organs and tissues. For this experiment, mice bearing A549 xenografts will be injected with 5  $\mu\text{Ci}$  of  $^{89}\text{Zr}$ -C' dot-scFv probe. Mice will be sacrificed at various time points (4, 24, 48, and 72 hours) and individual organs will be collected to measure radioactivity. The biodistribution data will establish the pharmacokinetics of the C' dot-scFv conjugates and will also be used to calculate dosimetry. Also, the specificity of  $^{89}\text{Zr}$ -labeled C' dot-scFv probe can be further confirmed by carrying out a blocking PET imaging study where  $^{89}\text{Zr}$ -labeled C' dot-scFv is co-injected in mice in the presence of excess MMP-12 specific scFv fragments (100 fold excess). Because of their high molar concentration, the non-radioactive scFvs should block the access of  $^{89}\text{Zr}$ -labeled nanoparticles to the tumor resulting in significant reduction in tumor uptake. In addition, MMP-12 specific C' dot-scFv nanoparticles can be radiolabeled with therapeutic radionuclides such as  $^{177}\text{Lu}$  to explore the possibility of radioimmunotherapy in a lung cancer model.

## **CHAPTER 4**

### **Phage Display Selection of Single-Chain Antibody Fragments Against Thomsen-Friedenreich Antigen (TF-Antigen)**

## Introduction

Thomsen-Friedenreich (TF) antigen is a disaccharide, galactose  $\beta$ 1-3 N-acetylgalactosamine alpha, which is also referred to as core-1 structure.(148) It is an O-linked mucin associated type glycan. In normal cells, the TF epitope is masked either by sialic acid or by other carbohydrate moieties. However, in cancer cells, the TF antigen is exposed on the surface due to aberrant glycosylation.(149) The presence of TF has been detected on the surface of ~ 90% of all carcinomas and thus TF is also known as a 'pancarcinoma antigen'. The expression of TF antigen has been shown in various types of cancers including breast, colon, liver, prostate, and ovary.(150) There may be numerous reasons for this increased exposure of TF antigen on the surface of tumor cells such as over expression of TF antigen, reduced level of enzymes that further glycosylate the core-1 structure, or increased synthesis of neuraminidase or other glycosidase enzymes that would strip more complex carbohydrates revealing this simple disaccharide.(151) TF expression on tumor cells is correlated with poor prognosis and tumor propagation. TF antigen is also involved in cell to cell adhesion and metastasis.(152,153) TF antigen is a major ligand for cell surface adhesion molecules like galactin-3. TF-expressing malignant cells bind to the endothelium through TF and galactin-3 interactions, which support tumor cell metastasis.(154) The phage display derived peptide (P30), discovered by the Quinn group, selectively bound to the TF antigen and was able to block TF mediated cell to cell adhesion of breast cancer cells.(155,156) On a related line, the Deutscher group demonstrated that

galactin-3 specific peptides inhibited metastasis associated cancer cell adhesion by blocking the TF and galactin-3 interaction.(157) A second generation TF specific peptide (P30-1) was used successfully for in vivo PET/CT imaging in a tumor mouse model.(158) Taken together, these studies suggest that TF antigen is a promising target for tumor imaging and therapeutic probe development.

Over the years, numerous attempts have been made to discover TF specific antibodies.(159-161) However, most of these antibodies are of the IgM class. Due to their large molecular weight and poor in vivo pharmacokinetic properties, the IgM class of antibodies are not suitable for in vivo applications.(162) The group of Kate Rittenhouse-Olson identified a mouse monoclonal IgG<sub>3</sub> antibody JAA-F11, which specifically bound to the tumor associated TF antigen alpha linkage.(163) This antibody has been shown to inhibit cancer cell growth, decrease metastasis, and improve survival in tumor breast cancer models.(164,165). Antibody fragments in either monovalent or multivalent forms have also been isolated for development of TF targeting molecular probes.(166-168) So far, there have been no reports of utilizing single-chain antibody fragments for in vivo imaging targeting TF antigen.

The aim of this project was to identify TF antigen specific scFv fragments for development of in vivo tumor imaging agents. To accomplish this goal, two rounds of phage display selection were carried out using the McCafferty scFv antibody library. A total of 96 clones were screened for their TF binding specificity. One selected TF scFv specific scFv clone was further characterized in vitro for its ability to recognize TF antigen on the MDA-MB-231 human breast

cancer cell line. The TF-specific 9C-scFv was expressed with C-terminal 6xHis-tag which allowed them to be radiolabeled directly with [ $^{99m}\text{Tc}(\text{CO})_3$ ] $^+$ .  $^{99m}\text{Tc}$  is one of the most commonly used radioisotopes for molecular imaging due to its favorable half-life ( $t_{1/2} = 6\text{h}$ ), low cost, and availability. Antibody fragments radiolabeled with  $^{99m}\text{Tc}$  by the 6xHis-tag sequence would yield scFvs with defined radionuclide coordination that would not interfere with the antigen recognition. The radiolabeled  $^{99m}\text{Tc}$ -scFv was evaluated for in vitro cell binding using TF displaying human breast cancer cell line MDA-MB-231. The  $^{99m}\text{Tc}$ -labeled scFv was investigated in vivo for its tumor binding ability by SPECT/CT imaging.

## **Materials and Methods**

### **Phage Display Selection**

Phage display selection was carried out using the McCafferty scFv library as described in Chapter 3. Briefly, 2 rounds of selections were performed using a standard affinity-selection method. For the first round, 10 ng of asialoglycophorin was adsorbed on the well of Nunc Maxisorb™ 96-well plate. For the second round, 10 ng of TF-conjugated human serum albumin (TF-HSA) was used. At the end of the second round, 96 individual colonies were picked for the phage ELISA screening.

### **Primary Screening by Individual Phage ELISA**

Phage ELISA was carried out to identify the phage-scFv clones with high binding specificity towards the TF epitope. Two Nunc Maxisorb™ 96-well plates were coated with 10 µg/ml (100 µl) of asialoglycophorin and asialofetuin. Both of these proteins display TF antigen on their surface and serve as target plates. While two additional plates coated with glycophorin and fetuin were used as negative control as these proteins do not display TF. Plates were blocked with Rockland blocking buffer (Rockland Inc., PA) and incubated with individual phage-scFv clones. After 1 hour incubation at room temperature, plates were washed 5 times with 0.1 % TBST and an anti-M13-HRP conjugated antibody (1:2000 dilution) was added to wells. To detect binding, 100 µl of 2,2'-Azino-bis(3-ethylbenzothiazoline-6-sulfonic acid) (ABTS) was added and the absorbance was measured at 405 nm using UV-Vis spectrophotometer plate

reader. Clones which displayed highest signal-to-noise ratios were picked for further analysis.

### **Sequence Analysis of Positive Clones**

A total of 5 phage clones with the highest binding ratios of asialoglycophorin-to-glycophorin and asialofetuin-to-fetuin in phage ELISA were selected for sequence analysis. These clones in the pSANG4 phagemid were sequenced using the forward primer M13 LeadSeq (5'-AAATTATTATTCGCAATTCCTTTGGTTGTTCT) and the reverse primer NotMycSeq (5'-GGCCCCATTCAGATCCTCTTCTGAGATGAG). These clones were analyzed for the presence of full-length scFv gene inserts and their sequence similarities using Serial Cloner™ software. Clones missing either heavy chain or light chain domains were removed. The clone which had the highest signal:noise ratio in ELISA and had intact VH and VL domains was selected for large scale expression.

### **Expression and Purification of The Selected scFv Fragment**

The selected scFv gene was subcloned into the pSANG10-3F expression vector using *NcoI/NotI* restriction enzymes as described in Chapter 3. The ligated plasmid was transformed into the chemically competent E.coli BL21 (DE3) cells for expression. A single colony of the scFv clone was grown in 30 ml of 2xTYKG media (2xTY media with kanamycin and 2% glucose) at 37°C overnight (250 rpm). The next day, 3L of 2xTYKG media was inoculated with the 30-ml of overnight culture and incubated at 37°C for 2.5-3.0 hours until the OD<sub>600</sub> reached

0.5-0.7. To induce the scFv expression, cells were pelleted at 4500 x g for 20 minutes, resuspended in 2xTY media (containing kanamycin and 1mM IPTG), and incubated at 37°C for 4 hours with shaking. The cell pellet was obtained by spinning down the culture at 4500 x g for 25 minutes. The pellet was resuspended in lysis buffer containing 20 mM Tris-HCL (pH 8.0), 500 mM NaCl, benzonase, and protease inhibitor cocktail. Cells were lysed by sonication and cell debris was pelleted at 27000 x g for 30 minutes. The supernatant was collected and filtered through 0.22 µm filter.

For the purification of the scFv, filtered supernatant was loaded onto a 5-ml HisTrap™ HP Ni-column. The column was washed with 10 column volumes of washing buffer (20 mM Tris-HCl, 500 mM NaCl, and 40 mM Imidazole; pH 8.0). The bound scFv was eluted with elution buffer (20 mM Tris-HCl, 500 mM NaCl, and 250 mM Imidazole; pH 8.0). ScFv containing fractions were pooled and the purity of the scFv was analyzed by SDS-PAGE and immunoblot.

### **ScFv-ELISA**

To determine the binding of purified scFv, wells of nunc MaxiSorp™ plates were coated with 100 µl (10 µg/ml) of asialoglycophorin and asialofetuin overnight. Wells coated with glycophorin, fetuin, and BSA were used as negative controls. Next day, plates were blocked with Rockland blocking buffer for 1 hour at room temperature. The purified scFv fragment (100 ng) was added to blocked wells and incubated for 1 hour at room temperature. Plates were washed 5 times

with 0.1% TBST before incubating with an anti-FLAG-HRP conjugated antibody for 1 hour at room temperature. After washing 5 times with 0.1% TBST, the binding was detected by addition of ABTS substrate and measuring the absorbance at 405 nm using a UV-Visible plate reader.

### **In Vitro Cell Binding Studies**

The binding characteristics of the purified 9C-scFv to the TF epitope was determined by flow cytometry using MDA-MB-231 human breast cancer cell line. MDA-MB-231 cells over expresses TF on their surface, while TF negative mouse melanoma cell line B10F16 was used as a negative control cell line. Cells ( $2 \times 10^5$  cells/ tube) were fixed with 4% paraformaldehyde for 10 minutes, followed by blocking with 5% BSA/TBS for 1 hour at room temperature. After washing 3 times with 1% BSA/TBS solution, cells were incubated with purified 9C-scFv at 4°C for 1 hour in the dark. After washing 3 times with 1% BSA/TBS, cells were incubated with an anti-FLAG-FITC secondary antibody. The binding was determined by measuring relative fluorescence intensity of stained cells by CyAn ADP flow cytometer (Beckman Coulter) using the FITC channel.

### **Microscale Thermophoresis**

To determine the binding affinity of selected 9C-scFv towards the TF epitope, microscale thermophoresis technique was used. The binding affinities of the scFv were calculated against TF expressing proteins asialoglycophorin and asialofetuin as described in Chapter 3.

## Radiolabeling

The selected 9C-scFv was radiolabeled directly with  $^{99m}\text{Tc}$  using the 6xHis-tag on the C-terminus. Briefly, 5 mCi of  $^{99m}\text{TcO}_4^-$  generator eluent was added directly into an IsoLink kit. The mixture was heated for  $100^\circ\text{C}$  for 20 minutes. The resultant  $[\text{}^{99m}\text{Tc}(\text{CO})_3]^+$  was mixed with 100  $\mu\text{g}$  of purified 9C-scFv in PBS. The pH was adjusted to 7.4 and labeling reaction was carried out at  $37^\circ\text{C}$  for 90 minutes. The labeling yield was calculated by ITLC using 200 mM EDTA as a mobile phase. The  $^{99m}\text{Tc}$ -labeled 9C-scFv was purified using a PD-10 gel-filtration column and the radiochemical yield was measured by ITLC.

To evaluate the stability of  $^{99m}\text{Tc}$ -labeled 9C-scFv, a histidine challenge was performed. The  $^{99m}\text{Tc}$ -labeled 9C-scFv was incubated with 5000 molar excess of histidine for 1h, 2h, and 4 hours. After the incubation, stability was determined by ITLS as described above.

## Cell Binding Analysis

$^{99m}\text{Tc}$ -labeled 9C-scFv (100 $\mu\text{L}$ ) was diluted to 100,000 counts per minute (CPM) aliquots and added to MDA-MB-231 cells or TF-negative B16F10 cells. After 1 hour of incubation, cells were washed three times with ice-cold 1% BSA/PBS buffer. Cells were centrifuged at 14000 x g for 5 minutes and supernatant was discarded. The pellet was collected and used for determining the binding by counting the radioactivity in a gamma counter.

## **A549 Lung Adenocarcinoma Xenograft Model**

All animal experiments were carried out in compliance with the Institutional Animal Care and Use committee in accordance with U.S. Public Health Service Guidelines. Athymic female BALB/C (*nu/nu*) mice were obtained from Envigo (USA) and inoculated with  $1 \times 10^7$  MDA-MB-231 cells in right shoulder subcutaneously. Tumors were allowed to grow for 3-4 weeks and mice were used when tumors were clearly visible, palpable, and measurable.

### **In Vivo Imaging**

For SPECT imaging, mice bearing MDA-MB-231 xenograft were injected with 300  $\mu\text{Ci}$  of  $^{99\text{m}}\text{Tc}$ -labeled 9C-scFv via tail vein. Whole-body SPECT/CT images were taken 4 hours post injection. For anatomical data fusion, small-animal CT was performed, and concurrent images were reconstructed with Fanbeam filtered-backprojection algorithm.

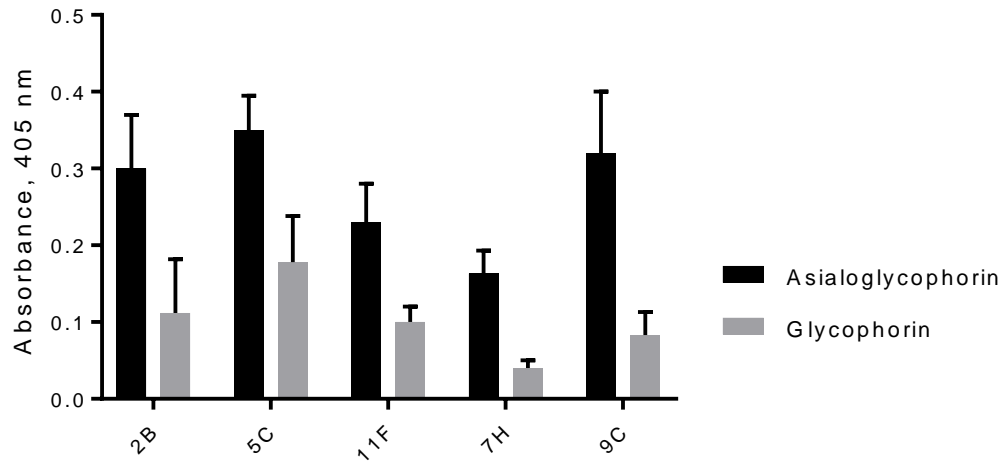
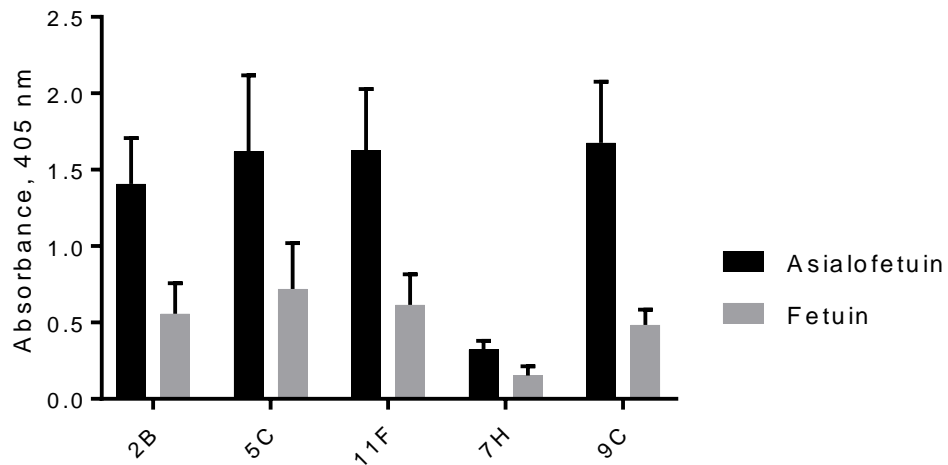
## Results

### Phage Display Selection

To isolate TF specific antibodies, two rounds of affinity selections were carried out using the McCafferty scFv library (diversity of  $1.1 \times 10^{10}$ ). To increase the stringency of the selection process and to avoid selecting antibodies against carrier proteins, each round of selection was performed using a different TF displaying carrier protein. The selection output of first round against asialoglycophorin was  $2.9 \times 10^4$  cfu, while the output of second round against TF-HSA was  $1.3 \times 10^5$  cfu with the enrichment of 4.48 times between two rounds. Since the helper phage with trypsin cleavable pIII protein was used for superinfection, only two rounds of selections were necessary.

### Phage ELISA

Phage ELISA was carried out with 96-colonies picked at the end of the second round of selection. The binding specificity against the TF antigen was determined by measuring binding signal for asialoglycophorin over glycophorin and asialofetuin over fetuin. There were 5 clones which had signal-to-noise ratio of  $\geq 3$ . (**Fig. 4.1**) These 5 clones were selected and sequenced by Sanger sequencing. The sequence analysis revealed that out of 5 clones, only one clone (9C) had the full scFv sequence with both heavy and light chain domains intact. The clone 9C was selected for large scale expression and downstream characterization.

**A****B**

**Figure 4.1:** Phage ELISA: At the end of the second round, 96 random phage clones were selected and screened for TF binding specificity. Individual phage-scFv clones were incubated with asialoglycophorin and asialofetuin coated 96-well plates and binding was detected using an anti-M13-HRP conjugated secondary antibody. Glycophorin and fetuin coated plates were used as negative control.

## ScFv Expression and Purification

The 9C-scFv gene was subcloned into the pSANG10-3F expression vector. Expression of 9C-scFv was induced by IPTG induction and purified by affinity chromatography using Ni-column as described in Chapter 3. The expression and purity of the 9C-scFv was verified by SDS-PAGE and immunoblot analysis (**Fig. 4.2**).

## ScFv-ELISA

In order to confirm binding specificity of the purified 9C-scFv towards the TF epitope, a secondary binding assay was performed with soluble 9C-scFv. The ELISA demonstrated that 9C-scFv retained its binding affinity towards TF displaying proteins asialoglycophorin and asialofetuin with minimal binding to TF negative glycophorin, fetuin, and BSA (**Fig. 4.3**). This assay proved that purified 9c-scFv in soluble form bound to the TF epitope and not to the carrier proteins.

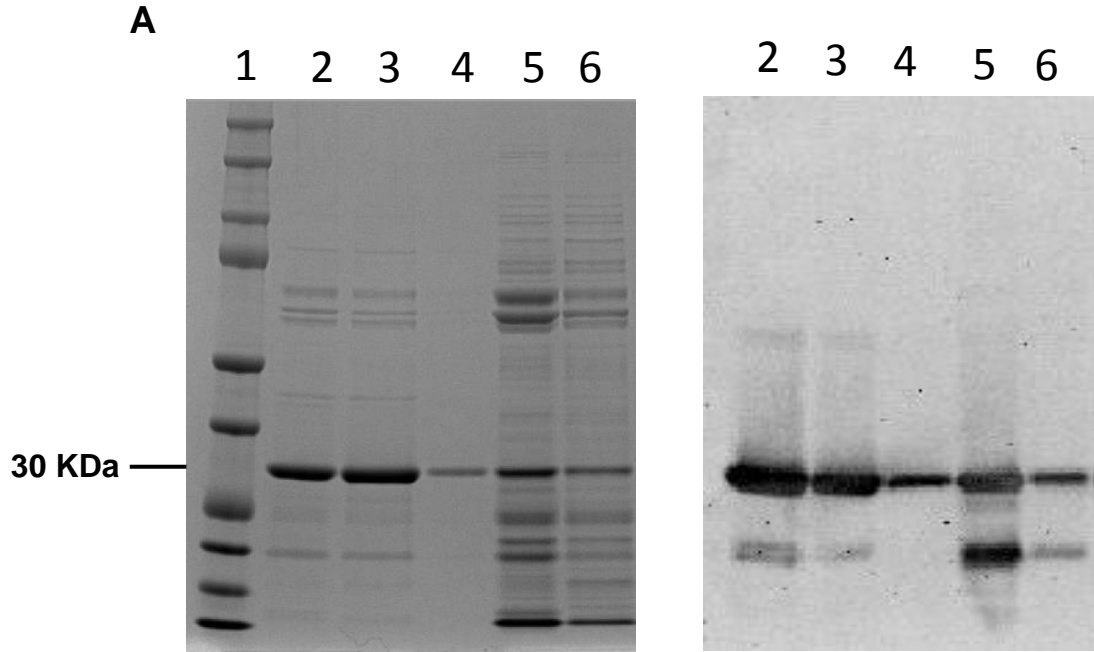


**Figure 4.2:** Expression and purification of 9C-scFv. The scFv was expressed by IPTG induction in E.coli BL21 cells and purified using a Ni-column. The purity of the eluted 9C-scFv was detected by A) SDS-PAGE gel, and B) Immunoblot analysis using anti-FLAG-HRP conjugated secondary antibody. Lane 1- Molecular weight markers, lane 2, 3, and 4- Eluted fractions containing purified 9C-scFv, lane 5- Loading sample, lane 6- Flow through.

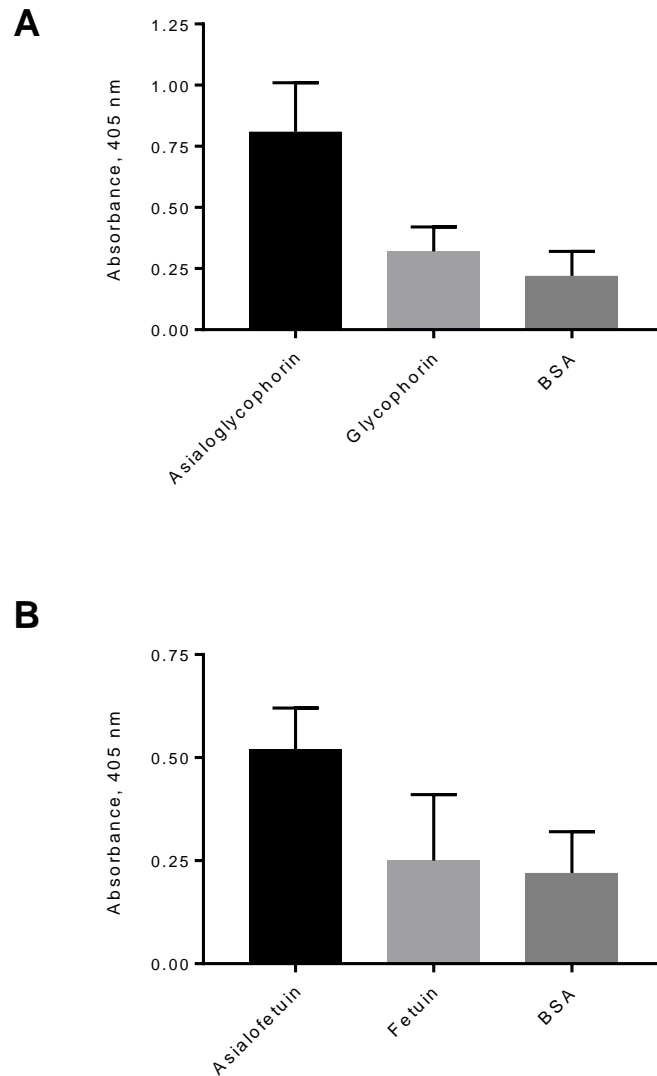


**Figure 4.3:** Soluble scFv ELISA. The binding specificity of purified 9C-scFvs was determined by incubating 100 ng of purified 9C-scFv fragments in wells coated with asialoglycophorin and asialofetuin. After the washing step, the wells were incubated with an anti-FLAG-HRP conjugated secondary antibody and the binding was detected by measuring absorbance at 405 nm. Bars represent the average of 3 replicates. Glycophorin, fetuin, and BSA were used as negative controls.

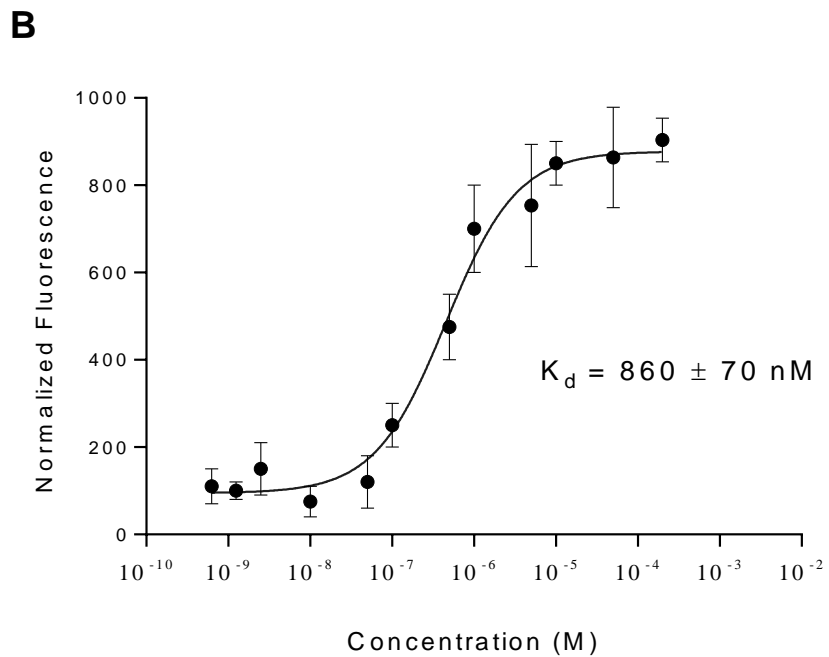
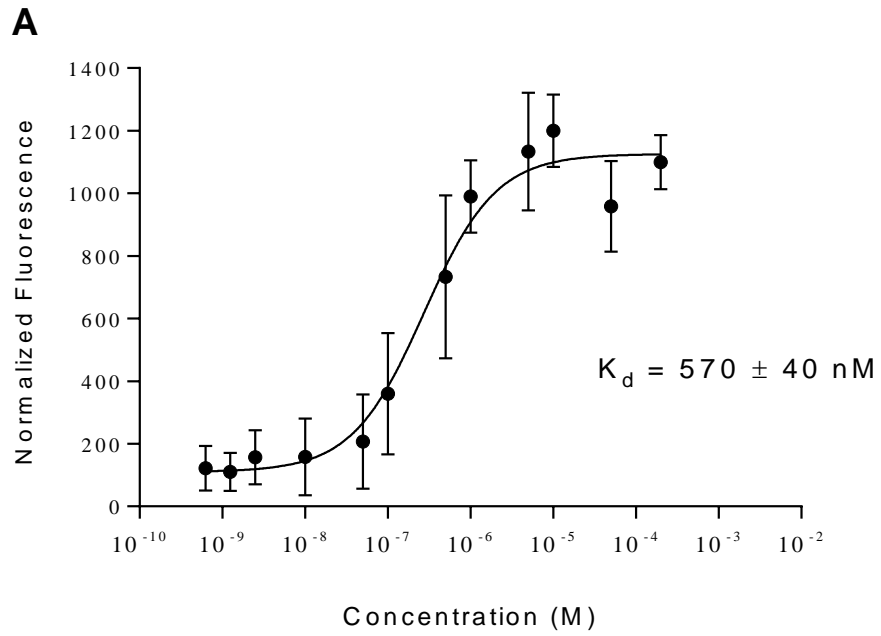


**Figure 4.4:** Binding affinity of the TF-specific 9C-scFv clone was determined for A) Asialoglycophorin and B) Asialofetuin by microscale thermophoresis.

## Cell Binding Analysis

Cell binding analysis was carried out by flow cytometry using MDA-MB-231 and B16F10 cells. As shown in **Fig. 4.5**, 9C-scFv bound to TF expressing MDA-MB-231 cells with higher specificity (MFI of  $16 \pm 4$ ) while the signal with TF negative cell line B16F10 was negligible (MFI of  $2 \pm 3$ ). Peanut agglutinin (PNA) was used as a positive control for TF binding (MFI of  $21 \pm 6$ ). The binding signal for selected 9C-scFv against MDA-MB-231 cells was very similar to PNA while the signal against B16F10 was similar to unstained negative control. These results confirmed that the 9C-scFv specifically bound to the TF epitope on the human breast cancer cell line.

## Radiolabeling and Cell Binding Analysis

The TF specific 9C-scFv was radiolabeled with  $^{99m}\text{Tc}$  using the IsoLink kit as previously described. A radiolabeling yield of 93% was achieved, while the radiochemical purity was found to be >99%. The  $^{99m}\text{Tc}$ -labeled 9C-scFv remained stable with 99% of the radiolabeled conjugate remaining intact after 4 hours at 37°C in human serum. The radiolabeled 9C-scFv was also remarkably stable during histidine challenge as 98% of  $^{99m}\text{Tc}$ -labeled 9C-scFv remained intact (**Table 4.1**).

In order to confirm the specificity of  $^{99m}\text{Tc}$ -labeled 9C-scFv towards TF epitope, an in vitro cell binding assay was performed. As shown in **Fig. 4.6**, the  $^{99m}\text{Tc}$ -labeled 9C-scFv demonstrated higher binding signal ( $7247 \pm 152$  CPM) to MDA-MB-231 cells, while the signal for TF-negative B16F10 cells was much

lower ( $856 \pm 51$  CPM). These cell binding assays demonstrated the specificity of  $^{99m}\text{Tc}$ -labeled 9C-scFv towards the TF antigen.

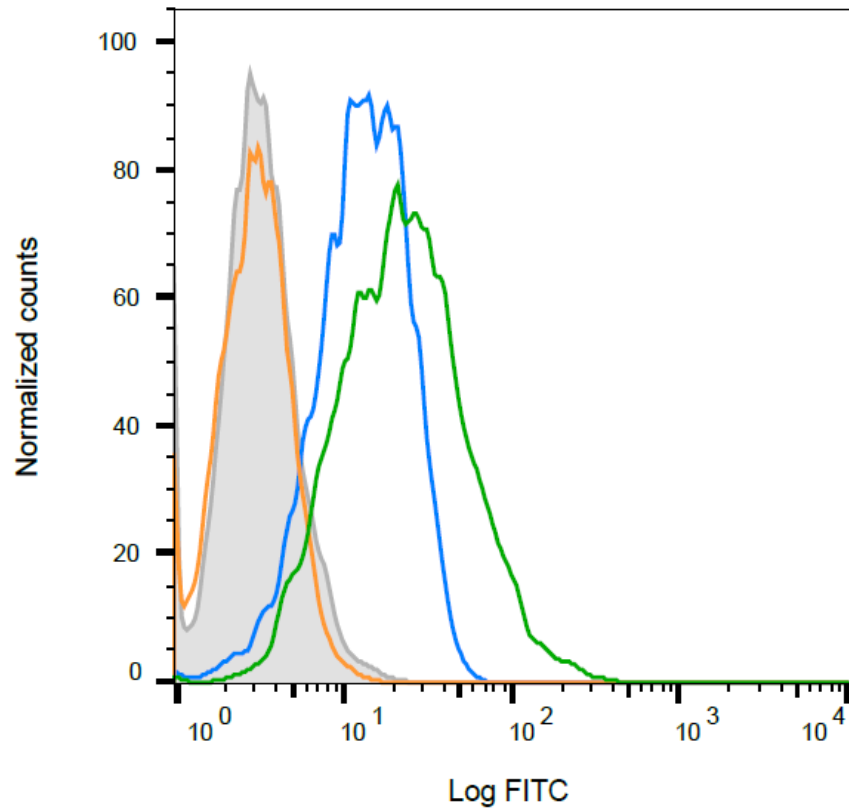


**Figure 4.5:** Flow cytometry analysis of 9C-scFv. The TF specific 9C-scFv was incubated with MDA-MB-231 ( ■ ) or B16F10 cells ( ■ ). Following 1 hour incubation on ice, cells were washed and incubated for additional 1 hour with an anti-FLAG-FITC conjugated secondary antibody. Binding was determined by counting 10,000 cells in a CyAn ADP flow cytometer. Peanut agglutinin ( ■ ) and unstained MDA-MB-231 cells ( ■ ) were used as negative control.

**Table 4.1:** Stability of  $^{99m}\text{Tc}$ -labeled 9C-scFv

Stability at 37°C	Human Serum (%)	5000 fold Histidine solution (%)
1 Hour	99.8	98.1
2 Hours	99.3	97.6
4 Hours	99.1	97.9

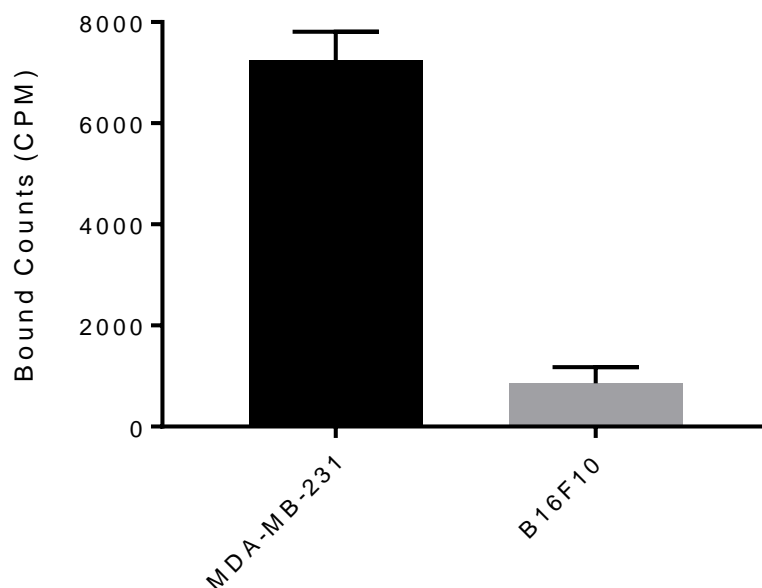


**Figure 4.6:** In vitro cell binding assay. The MDA-MB-231 human breast cancer and B16F10 mouse melanoma cells were incubated with 100,000 counts (cpm) of  $^{99m}\text{Tc}$ -9C labeled scFv for 1 hour. Following washing, bound scFv was detected by gamma counter. Bars represent the mean of 3 replicates with standard deviation.

## **In vivo SPECT Imaging**

The binding capability of the  $^{99m}\text{Tc}$ -labeled 9C-scFv was explored in mice bearing MDA-MB-231 tumors. Full-body SPECT/CT images were acquired 4 hours after the i.v. injection of  $^{99m}\text{Tc}$ -scFv via tail vein. The image revealed a moderate tumor uptake and significant accumulation in the liver and kidneys (**Fig. 4.7**).

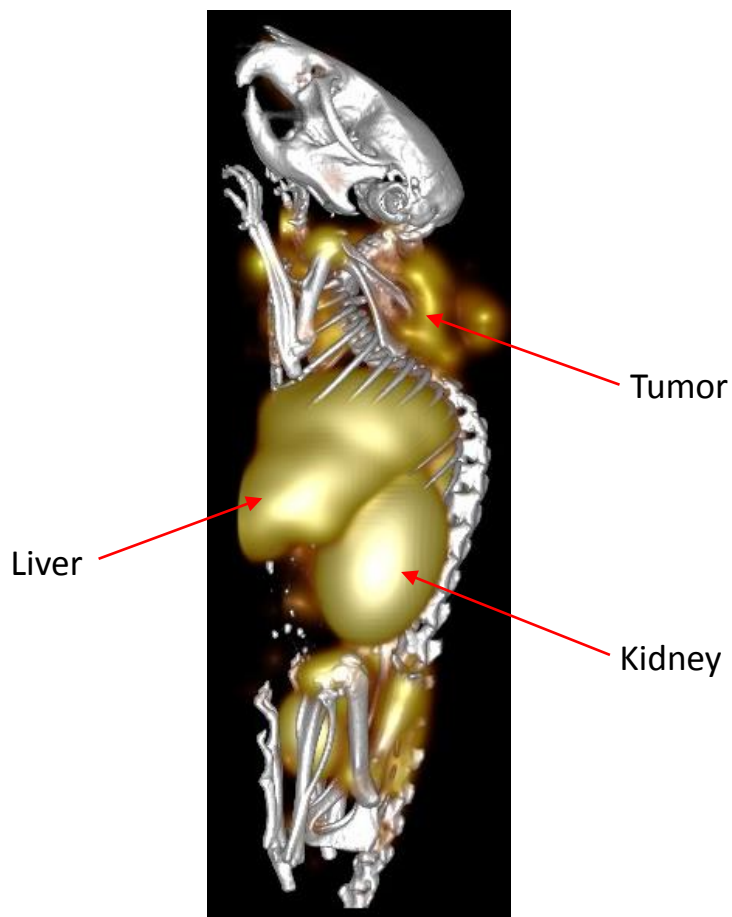


**Figure 4.7:** In vivo SPECT/CT imaging. A MDA-MB-231 tumor bearing mouse was injected with 300  $\mu\text{Ci}$  of  $^{99\text{m}}\text{Tc}$ -9C-scFv via tail vein injection. The SPECT/CT image was acquired 4 hours post injection.

## Discussion

In this project, we described the selection and isolation of Thomsen-Friedenreich (TF) specific scFv antibodies by phage display methodology. Two rounds of phage display selections were carried out using the McCafferty antibody library. In order to enrich the library towards the TF epitope, and not protein backbone, the library was exposed to two different TF presenting proteins during the selection process. Asialoglycophorin, which has 6 TF epitopes on its surface, was chosen for the first round as it displays TF in its natural conformation. The second round was carried out using TF-HSA, in which 20 TF molecules were chemically conjugated to human serum albumin. A total of 96 clones were randomly picked for the initial screening to identify TF-specific scFvs by phage ELISA. From these 96 clones, 5 clones were identified that displayed higher binding towards TF presenting targets (asialoglycophorin and asialofetuin) over their non-TF presenting counterparts (glycophorin and fetuin). Because asialofetuin, which has 3 TF epitopes, was not used during the selection process, the higher signal-to-background ratios for asialofetuin over fetuin indicated that the selected antibodies were indeed recognizing the TF antigen and not binding to protein backbone. The Sanger sequence analysis of these 5 clones revealed that only one clone (9C) had an intact scFv gene with both VH and VL domains present. The 9C-scFv clone was selected for large scale protein expression and further characterization.

The TF-specific 9C-scFv was expressed in E.coli and purified using a Ni-column. The binding specificity of the purified 9C-scFv was confirmed by ELISA

using asialoglycophorin and asialofetuin as targets. The signal-to-background ratios of  $> 2$  confirmed that 9C-scFv specifically recognized the TF epitope. The lower than expected signal-to-noise ratios in ELISA was likely due to monovalent scFv binding and the fact that TF is a very small epitope and there are only a few TF disaccharide molecules on the carrier protein molecule (6 per asialoglycophorin and 3 per asialofetuin molecule). The binding constant of 9C-scFv was measured by microscale thermophoresis analysis. The 9C-scFv bound to the asialoglycophorin with the binding affinity ( $K_d$ ) of  $570 \pm 40$  nM, while the  $K_d$  for asialofetuin was found to be  $860 \pm 70$  nM (**Fig. 4.4**). These values are consistent with previously published binding affinities for antibodies/peptides against carbohydrate antigens.(155,163,166) In vitro cell binding analysis by flow cytometry asserted that 9C-scFv recognized the TF antigen on the human breast cancer cell line MDA-MB-231, while it displayed minimal binding to the TF-negative B16F10 cells (**Fig. 4.5**)

The 9C-scFv was radiolabeled with  $^{99m}\text{Tc}$  by directly conjugating  $^{99m}\text{Tc}$  to the C-terminal 6xHis-tag. Previously published reports suggested that every other histidine molecule in 6xHis-tag is involved in coordinating the  $^{99m}\text{Tc}$ .(169-171) Using this direct labeling approach, the 9C-scFv was radiolabeled with a high labeling yield ( $> 93\%$ ) and with high serum stability ( $> 98\%$  after 4 hours). The in vitro cell binding analysis revealed that  $^{99m}\text{Tc}$ -labeled 9C-scFv bound to the TF displaying MDA-MB-231 cells significantly better than the B16F10, asserting that radiolabeling with  $^{99m}\text{Tc}$  did not affect the ability of the  $^{99m}\text{Tc}$ -labeled 9C-scFv to recognize and bind to the TF antigen (**Fig. 6**). The  $^{99m}\text{Tc}$ -

labeled 9C-scFv was administered in mice bearing MDA-MB-231 xenografts via tail vein and whole-body SPECT/CT images were acquired 4 hours post injection (**Fig. 4.7**). The SPECT images revealed that there was a moderate tumor uptake of  $^{99m}\text{Tc}$ -labeled 9C-scFv in vivo. However, images also showed a significant non-target accumulation in other body organs such as kidneys, liver, and stomach. The high kidney uptake can be attributed to the fact that scFv fragments clear out of body via kidneys.(51) The presence of positively charged histidine residues in the C-terminal tail of scFvs may also lead to non-specific binding of scFvs to the negatively charged kidney tubules.(173-175) Previously published reports also suggested that the N-terminus His-tag and its subsequent radiolabeling with  $^{99m}\text{Tc}$  have been associated with significantly high liver uptake.(175-178) Taken together, these results demonstrated that even though 9C-scFv bound specifically to the TF epitope in vitro, it did not result in high contrast in vivo SPECT/CT images. There are number of strategies that may be utilized to improve the pharmacokinetics of these scFv fragments. To remove the influence of His-tag in high liver and kidney retentions, scFvs can be expressed and purified without any tags or with other tags such as FLAG tag or enzymatic removal of tag post purification. Alternatively, as described in Chapter 3, we can conjugate 9C-scFv to the ultrasmall silica particles and assess the difference in the biodistribution profile of the resulting nano-immunoconjugates.

In conclusion, here we described the identification of a Thomsen-Friedenreich specific scFv fragment using phage display technology. The TF specific 9C-scFv clone was characterized in vitro for its Tf-specificity. The 9C-

scFv was radiolabeled with  $^{99m}\text{Tc}$  and investigated in vivo for its SPECT/CT imaging properties in mice bearing human breast cancer xenografts. Even though  $^{99m}\text{Tc}$ -labeled 9C-scFv showed moderate tumor accumulation, there was also a significant non-specific retention in other major body organs. More work needs to be performed to alter the pharmacokinetics of the TF-specific 9C-scFv to achieve high-contrast in vivo images.

## REFERENCES

1. Hussain, T.; Nguyen, Q. T., Molecular imaging for cancer diagnosis and surgery. *Advanced drug delivery reviews* 2014, 66, 90-100.
2. Weissleder, R., Molecular imaging in cancer. *Science* 2006, 312, 1168-1171.
3. Del Vecchio, S.; Zannetti, A.; Fonti, R.; Pace, L.; Salvatore, M., Nuclear imaging in cancer theranostics. *The Quarterly Journal of Nuclear Medicine and Molecular Imaging* 2007, 51, 152.
4. Kurdziel, K.; Ravizzini, G.; Croft, B.; Tatum, J.; Choyke, P.; Kobayashi, H., The evolving role of nuclear molecular imaging in cancer. *Expert opinion on medical diagnostics* 2008, 2, 829-842.
5. Mariani, G.; Bruselli, L.; Kuwert, T.; Kim, E. E.; Flotats, A.; Israel, O.; Dondi, M.; Watanabe, N., A review on the clinical uses of SPECT/CT. *European journal of nuclear medicine and molecular imaging* 2010, 37, 1959-1985.
6. Banerjee, S.; Pillai, M. R. A.; Ramamoorthy, N. In *Evolution of Tc-99m in diagnostic radiopharmaceuticals*, Seminars in nuclear medicine, Elsevier: 2001; pp 260-277.
7. Zolle, I., *Technetium-99m pharmaceuticals*. Springer: 2007.
8. Bailey, D. L.; Willowson, K. P., An evidence-based review of quantitative SPECT imaging and potential clinical applications. *J Nucl Med* 2013, 54, 83-89.

9. Reddy, S.; Robinson, M. K. In *Immuno-positron emission tomography in cancer models*, Seminars in nuclear medicine, Elsevier: 2010; pp 182-189.
10. Alauddin, M. M., Positron emission tomography (PET) imaging with <sup>18</sup>F-based radiotracers. *American journal of nuclear medicine and molecular imaging* 2012, 2, 55.
11. Gambhir, S. S., Molecular imaging of cancer with positron emission tomography. *Nature Reviews Cancer* 2002, 2, 683.
12. Vaquero, J. J.; Kinahan, P., Positron emission tomography: current challenges and opportunities for technological advances in clinical and preclinical imaging systems. *Annual review of biomedical engineering* 2015, 17, 385-414.
13. Wu, A. M.; Senter, P. D., Arming antibodies: prospects and challenges for immunoconjugates. *Nature biotechnology* 2005, 23, 1137.
14. Freise, A. C.; Wu, A. M., In vivo imaging with antibodies and engineered fragments. *Molecular immunology* 2015, 67, 142-152.
15. Wu, A. M., Engineered antibodies for molecular imaging of cancer. *Methods* 2014, 65, 139-147.
16. Gordon, L. I.; Witzig, T.; Molina, A.; Czuczman, M.; Emmanouilides, C.; Joyce, R.; Vo, K.; Theuer, C.; Pohlman, B.; Bartlett, N., <sup>90</sup>Yttrium-labeled ibritumomab tiuxetan radioimmunotherapy produces high response rates and durable remissions in patients with previously treated B-cell lymphoma. *Clinical lymphoma* 2004, 5, 98-101.
17. Kaminski, M. S.; Tuck, M.; Estes, J.; Kolstad, A.; Ross, C. W.; Zasadny,

- K.; Regan, D.; Kison, P.; Fisher, S.; Kroll, S.,  $^{131}\text{I}$ -tositumomab therapy as initial treatment for follicular lymphoma. *New England Journal of Medicine* 2005, 352, 441-449.
18. Boerman, O. C.; van Schaijk, F. G.; Oyen, W. J.; Corstens, F. H., Pretargeted radioimmunotherapy of cancer: progress step by step. *Journal of Nuclear Medicine* 2003, 44, 400.
  19. Bailly, C.; Bodet-Milin, C.; Rousseau, C.; Faivre-Chauvet, A.; Kraeber-Bodéré, F.; Barbet, J., Pretargeting for imaging and therapy in oncological nuclear medicine. *EJNMMI radiopharmacy and chemistry* 2017, 2, 6.
  20. Knight, J. C.; Cornelissen, B., Bioorthogonal chemistry: implications for pretargeted nuclear (PET/SPECT) imaging and therapy. *American journal of nuclear medicine and molecular imaging* 2014, 4, 96.
  21. Sletten, E. M.; Bertozzi, C. R., From mechanism to mouse: a tale of two bioorthogonal reactions. *Accounts of chemical research* 2011, 44, 666-676.
  22. Marik, J.; Sutcliffe, J. L., Click for PET: rapid preparation of [18F] fluoro-peptides using CuI catalyzed 1, 3-dipolar cycloaddition. *Tetrahedron Letters* 2006, 47, 6681-6684.
  23. Hausner, S. H.; Marik, J.; Gagnon, M. K. J.; Sutcliffe, J. L., In vivo positron emission tomography (PET) imaging with an  $\alpha\text{v}\beta\text{6}$  specific peptide radiolabeled using  $^{18}\text{F}$ -“click” chemistry: evaluation and comparison with the corresponding 4-[18F] fluorobenzoyl- and 2-[18F] fluoropropionyl-peptides. *Journal of medicinal chemistry* 2008, 51, 5901-5904.

24. Li, Z.-B.; Wu, Z.; Chen, K.; Chin, F. T.; Chen, X., Click chemistry for  $^{18}\text{F}$ -labeling of RGD peptides and microPET imaging of tumor integrin  $\alpha\text{v}\beta\text{3}$  expression. *Bioconjugate chemistry* 2007, 18, 1987-1994.
25. Lin, F. L.; Hoyt, H. M.; van Halbeek, H.; Bergman, R. G.; Bertozzi, C. R., Mechanistic investigation of the Staudinger ligation. *Journal of the American Chemical Society* 2005, 127, 2686-2695.
26. Vugts, D. J.; Vervoort, A.; Stigter-van Walsum, M.; Visser, G. W.; Robillard, M. S.; Versteegen, R. M.; Vulderson, R. C.; Herscheid, J. D.; van Dongen, G. A., Synthesis of phosphine and antibody-azide probes for in vivo Staudinger ligation in a pretargeted imaging and therapy approach. *Bioconjugate chemistry* 2011, 22, 2072-2081.
27. Rossin, R.; Robillard, M. S., Pretargeted imaging using bioorthogonal chemistry in mice. *Current opinion in chemical biology* 2014, 21, 161-169.
28. Lee, S. B.; Kim, H. L.; Jeong, H. J.; Lim, S. T.; Sohn, M. H.; Kim, D. W., Mesoporous silica nanoparticle pretargeting for PET imaging based on a rapid bioorthogonal reaction in a living body. *Angewandte Chemie* 2013, 125, 10743-10746.
29. Blackman, M. L.; Royzen, M.; Fox, J. M., Tetrazine ligation: fast bioconjugation based on inverse-electron-demand Diels- Alder reactivity. *Journal of the American Chemical Society* 2008, 130, 13518-13519.
30. Rossin, R.; Renart Verkerk, P.; van den Bosch, S. M.; Vulderson, R. C.; Verel, I.; Lub, J.; Robillard, M. S., In vivo chemistry for pretargeted tumor imaging in live mice. *Angewandte Chemie* 2010, 122, 3447-3450.

31. Zeglis, B. M.; Sevak, K. K.; Reiner, T.; Mohindra, P.; Carlin, S. D.; Zanzonico, P.; Weissleder, R.; Lewis, J. S., A pretargeted PET imaging strategy based on bioorthogonal Diels–Alder click chemistry. *Journal of nuclear medicine: official publication, Society of Nuclear Medicine* 2013, *54*, 1389.
32. Houghton, J. L.; Membreno, R.; Abdel-Atti, D.; Cunanan, K. M.; Carlin, S.; Scholz, W. W.; Zanzonico, P. B.; Lewis, J. S.; Zeglis, B. M., Establishment of the in vivo efficacy of pretargeted radioimmunotherapy utilizing inverse electron demand Diels-Alder click chemistry. *Molecular cancer therapeutics* 2017, *16*, 124-133.
33. Wang, C. H.; Willis, D. L.; Loveland, W. D., *Radiotracer methodology in the biological environmental, and physical sciences*. 1975.
34. Kim, Y.-S.; Brechbiel, M. W., An overview of targeted alpha therapy. *Tumor biology* 2012, *33*, 573-590.
35. Couturier, O.; Supiot, S.; Degraef-Mouglin, M.; Faivre-Chauvet, A.; Carlier, T.; Chatal, J.-F.; Davodeau, F.; Cherel, M., Cancer radioimmunotherapy with alpha-emitting nuclides. *European journal of nuclear medicine and molecular imaging* 2005, *32*, 601-614.
36. McDevitt, M. R.; Ma, D.; Lai, L. T.; Simon, J.; Borchardt, P.; Frank, R. K.; Wu, K.; Pellegrini, V.; Curcio, M. J.; Miederer, M., Tumor therapy with targeted atomic nanogenerators. *Science* 2001, *294*, 1537-1540.
37. Su, F.-M.; Beaumier, P.; Axworthy, D.; Atcher, R.; Fritzberg, A., Pretargeted radioimmunotherapy in tumored mice using an in vivo

- 212Pb/212Bi generator. *Nuclear medicine and biology* 2005, 32, 741-747.
38. Milenic, D. E.; Garmestani, K.; Brady, E. D.; Albert, P. S.; Ma, D.; Abdulla, A.; Brechbiel, M. W.,  $\alpha$ -Particle radioimmunotherapy of disseminated peritoneal disease using a  $^{212}\text{Pb}$ -labeled radioimmunoconjugate targeting HER2. *Cancer biotherapy & radiopharmaceuticals* 2005, 20, 557-568.
39. Miao, Y.; Hyilarides, M.; Fisher, D. R.; Shelton, T.; Moore, H.; Wester, D. W.; Fritzberg, A. R.; Winkelmann, C. T.; Hoffman, T.; Quinn, T. P., Melanoma therapy via peptide-targeted  $\alpha$ -radiation. *Clinical cancer research* 2005, 11, 5616-5621.
40. Tan, Z.; Chen, P.; Schneider, N.; Glover, S.; Cui, L.; Torgue, J.; Rixe, O.; Spitz, H. B.; Dong, Z., Significant systemic therapeutic effects of high-LET immunoradiation by  $^{212}\text{Pb}$ -trastuzumab against prostatic tumors of androgen-independent human prostate cancer in mice. *International journal of oncology* 2012, 40, 1881-1888.
41. Chappell, L. L.; Dadachova, E.; Milenic, D. E.; Garmestani, K.; Wu, C.; Brechbiel, M. W., Synthesis, characterization, and evaluation of a novel bifunctional chelating agent for the lead isotopes  $^{203}\text{Pb}$  and  $^{212}\text{Pb}$ . *Nuclear medicine and biology* 2000, 27, 93-100.
42. Milenic, D. E.; Garmestani, K.; Brady, E. D.; Albert, P. S.; Abdulla, A.; Flynn, J.; Brechbiel, M. W., Potentiation of high-LET radiation by gemcitabine: targeting HER2 with trastuzumab to treat disseminated peritoneal disease. *Clinical Cancer Research* 2007, 13, 1926-1935.
43. Milenic, D. E.; Garmestani, K.; Brady, E. D.; Baidoo, K. E.; Albert, P. S.;

- Wong, K. J.; Flynn, J.; Brechbiel, M. W., Multimodality therapy: potentiation of high linear energy transfer radiation with paclitaxel for the treatment of disseminated peritoneal disease. *Clinical Cancer Research* 2008, *14*, 5108-5115.
44. Meredith, R. F.; Torgue, J. J.; Rozgaja, T. A.; Banaga, E. P.; Bunch, P. W.; Alvarez, R. D.; Straughn Jr, J. M.; Dobelbower, M. C.; Lowy, A. M., Safety and outcome measures of first-in-human intraperitoneal  $\alpha$  radioimmunotherapy with  $^{212}\text{Pb}$ -TCMC-trastuzumab. *American journal of clinical oncology* 2018, *41*, 716.
45. Meredith, R.; Torgue, J.; Shen, S.; Fisher, D. R.; Banaga, E.; Bunch, P.; Morgan, D.; Fan, J.; Straughn Jr, J. M., Dose escalation and Dosimetry of first in human alpha radioimmunotherapy with  $^{212}\text{Pb}$ -TCMC-trastuzumab. *Journal of nuclear medicine: official publication, Society of Nuclear Medicine* 2014, *55*, 1636.
46. Köhler, G.; Milstein, C., Continuous cultures of fused cells secreting antibody of predefined specificity. *Nature* 1975, *256*, 495.
47. Schroeder Jr, H. W.; Cavacini, L., Structure and function of immunoglobulins. *Journal of Allergy and Clinical Immunology* 2010, *125*, S41-S52.
48. Strohl, W. R., Optimization of Fc-mediated effector functions of monoclonal antibodies. *Current opinion in biotechnology* 2009, *20*, 685-691.
49. Holliger, P.; Hudson, P. J., Engineered antibody fragments and the rise of

- single domains. *Nature biotechnology* 2005, 23, 1126.
50. Nelson, A. L. In *Antibody fragments: hope and hype*, MAbs, Taylor & Francis: 2010; pp 77-83.
  51. Monnier, P.; Vigouroux, R.; Tassew, N., In vivo applications of single chain Fv (variable domain)(scFv) fragments. *Antibodies* 2013, 2, 193-208.
  52. Reilly, R.; Maiti, P.; Kiarash, R.; Prashar, A.; Fast, D.; Entwistle, J.; Dan, M.; Narang, S.; Foote, S.; Kaplan, H., Rapid imaging of human melanoma xenografts using an scFv fragment of the human monoclonal antibody H11 labelled with <sup>111</sup>In. *Nuclear medicine communications* 2001, 22, 587-595.
  53. Kobayashi, K.; Sasaki, T.; Takenaka, F.; Yakushiji, H.; Fujii, Y.; Kishi, Y.; Kita, S.; Shen, L.; Kumon, H.; Matsuura, E., A novel PET imaging using <sup>64</sup>Cu-labeled monoclonal antibody against mesothelin commonly expressed on cancer cells. *Journal of immunology research* 2015, 2015.
  54. Ueda, M.; Hisada, H.; Temma, T.; Shimizu, Y.; Kimura, H.; Ono, M.; Nakamoto, Y.; Togashi, K.; Saji, H., Gallium-68-labeled anti-HER2 single-chain Fv fragment: development and in vivo monitoring of HER2 expression. *Molecular imaging and biology* 2015, 17, 102-110.
  55. Berndorff, D.; Borkowski, S.; Moosmayer, D.; Viti, F.; Muller-Tiemann, B.; Sieger, S.; Friebe, M.; Hilger, C. S.; Zardi, L.; Neri, D., Imaging of Tumor Angiogenesis Using <sup>99m</sup>Tc-Labeled Human Recombinant Anti-ED-B Fibronectin Antibody Fragments. *Journal of nuclear medicine* 2006, 47, 1707.

56. Smith, G. P., Filamentous fusion phage: novel expression vectors that display cloned antigens on the virion surface. *Science* 1985, 228, 1315-1317.
57. McCafferty, J.; Griffiths, A. D.; Winter, G.; Chiswell, D. J., Phage antibodies: filamentous phage displaying antibody variable domains. *nature* 1990, 348, 552.
58. Scarselli, E.; Esposito, G.; Traboni, C., Receptor phage: display of functional domains of the human high affinity IgE receptor on the M13 phage surface. *FEBS letters* 1993, 329, 223-226.
59. McCafferty, J.; Jackson, R. H.; Chiswell, D. J., Phage-enzymes: expression and affinity chromatography of functional alkaline phosphatase on the surface of bacteriophage. *Protein Engineering, Design and Selection* 1991, 4, 955-961.
60. Cramer, R.; Suter, M., Display of biologically active proteins on the surface of filamentous phages: a cDNA cloning system for selection of functional gene products linked to the genetic information responsible for their production. *Gene* 1993, 137, 69-75.
61. Barbas, C. F.; Kang, A. S.; Lerner, R. A.; Benkovic, S. J., Assembly of combinatorial antibody libraries on phage surfaces: the gene III site. *Proceedings of the National Academy of Sciences* 1991, 88, 7978-7982.
62. Clackson, T.; Hoogenboom, H. R.; Griffiths, A. D.; Winter, G., Making antibody fragments using phage display libraries. *Nature* 1991, 352, 624.
63. Griffiths, A. D.; Williams, S. C.; Hartley, O.; Tomlinson, I.; Waterhouse, P.;

- Crosby, W. L.; Kontermann, R.; Jones, P.; Low, N.; Allison, T. a., Isolation of high affinity human antibodies directly from large synthetic repertoires. *The EMBO journal* 1994, 13, 3245-3260.
64. Hoogenboom, H. R.; de Bruïne, A. P.; Hufton, S. E.; Hoet, R. M.; Arends, J.-W.; Roovers, R. C., Antibody phage display technology and its applications. *Immunotechnology* 1998, 4, 1-20.
65. Schofield, D. J.; Pope, A. R.; Clementel, V.; Buckell, J.; Chapple, S. D.; Clarke, K. F.; Conquer, J. S.; Crofts, A. M.; Crowther, S. R.; Dyson, M. R., Application of phage display to high throughput antibody generation and characterization. *Genome biology* 2007, 8, R254.
66. Goletz, S.; Christensen, P. A.; Kristensen, P.; Blohm, D.; Tomlinson, I.; Winter, G.; Karsten, U., Selection of large diversities of antiidiotypic antibody fragments by phage display<sup>1</sup>. *Journal of molecular biology* 2002, 315, 1087-1097.
67. Kristensen, P.; Winter, G., Proteolytic selection for protein folding using filamentous bacteriophages. *Folding and Design* 1998, 3, 321-328.
68. Vaughan, T. J.; Williams, A. J.; Pritchard, K.; Osbourn, J. K.; Pope, A. R.; Earnshaw, J. C.; McCafferty, J.; Hodits, R. A.; Wilton, J.; Johnson, K. S., Human antibodies with sub-nanomolar affinities isolated from a large non-immunized phage display library. *Nature biotechnology* 1996, 14, 309-314.
69. Sheets, M. D.; Amersdorfer, P.; Finnern, R.; Sargent, P.; Lindqvist, E.; Schier, R.; Hemingsen, G.; Wong, C.; Gerhart, J. C.; Marks, J. D., Efficient construction of a large nonimmune phage antibody library: the production

- of high-affinity human single-chain antibodies to protein antigens. *Proceedings of the National Academy of Sciences* 1998, 95, 6157-6162.
70. Pavoni, E.; Flego, M.; Dupuis, M. L.; Barca, S.; Petronzelli, F.; Anastasi, A. M.; D'Alessio, V.; Pelliccia, A.; Vaccaro, P.; Monteriù, G., Selection, affinity maturation, and characterization of a human scFv antibody against CEA protein. *BMC cancer* 2006, 6, 41.
71. Nagase, H.; Visse, R.; Murphy, G., Structure and function of matrix metalloproteinases and TIMPs. *Cardiovascular research* 2006, 69, 562-573.
72. Itoh, Y.; Nagase, H., Matrix metalloproteinases in cancer. *Essays in biochemistry* 2002, 38, 21-36.
73. Page-McCaw, A.; Ewald, A. J.; Werb, Z., Matrix metalloproteinases and the regulation of tissue remodelling. *Nature reviews Molecular cell biology* 2007, 8, 221.
74. Newby, A. C., Dual role of matrix metalloproteinases (matrixins) in intimal thickening and atherosclerotic plaque rupture. *Physiological reviews* 2005, 85, 1-31.
75. Shah, P. K., Inflammation, metalloproteinases, and increased proteolysis: an emerging pathophysiological paradigm in aortic aneurysm. *Circulation* 1997, 96, 2115-2117.
76. Burrage, P. S.; Mix, K. S.; Brinckerhoff, C. E., Matrix metalloproteinases: role in arthritis. *Front Biosci* 2006, 11, 529-543.
77. Gialeli, C.; Theocharis, A. D.; Karamanos, N. K., Roles of matrix

metalloproteinases in cancer progression and their pharmacological targeting. *The FEBS journal* 2011, 278, 16-27.

78. Jabłońska-Trypuć, A.; Matejczyk, M.; Rosochacki, S., Matrix metalloproteinases (MMPs), the main extracellular matrix (ECM) enzymes in collagen degradation, as a target for anticancer drugs. *Journal of enzyme inhibition and medicinal chemistry* 2016, 31, 177-183.
79. Yadav, L.; Puri, N.; Rastogi, V.; Satpute, P.; Ahmad, R.; Kaur, G., Matrix metalloproteinases and cancer-roles in threat and therapy. *Asian Pac J Cancer Prev* 2014, 15, 1085-1091.
80. Werb, Z.; Gordon, S., Elastase secretion by stimulated macrophages. Characterization and regulation. *Journal of Experimental Medicine* 1975, 142, 361-377.
81. Johnson, J. L.; Devel, L.; Czarny, B.; George, S. J.; Jackson, C. L.; Rogakos, V.; Beau, F.; Yiotakis, A.; Newby, A. C.; Dive, V., A selective matrix metalloproteinase-12 inhibitor retards atherosclerotic plaque development in apolipoprotein E–knockout mice. *Arteriosclerosis, thrombosis, and vascular biology* 2011, 31, 528-535.
82. Hunninghake, G. M.; Cho, M. H.; Tesfaigzi, Y.; Soto-Quiros, M. E.; Avila, L.; Lasky-Su, J.; Stidley, C.; Melén, E.; Söderhäll, C.; Hallberg, J., MMP12, lung function, and COPD in high-risk populations. *New England Journal of Medicine* 2009, 361, 2599-2608.
83. Wang, X.; Liang, J.; Koike, T.; Sun, H.; Ichikawa, T.; Kitajima, S.; Morimoto, M.; Shikama, H.; Watanabe, T.; Sasaguri, Y., Overexpression

- of human matrix metalloproteinase-12 enhances the development of inflammatory arthritis in transgenic rabbits. *The American journal of pathology* 2004, 165, 1375-1383.
84. Longo, G. M.; Buda, S. J.; Fiotta, N.; Xiong, W.; Griener, T.; Shapiro, S.; Baxter, B. T., MMP-12 has a role in abdominal aortic aneurysms in mice. *Surgery* 2005, 137, 457-462.
85. Ella, E.; Harel, Y.; Abraham, M.; Wald, H.; Benny, O.; Karsch-Bluman, A.; Vincent, D.; Laurent, D.; Amir, G.; Izhar, U., Matrix metalloproteinase 12 promotes tumor propagation in the lung. *The Journal of thoracic and cardiovascular surgery* 2018, 155, 2164-2175. e2161.
86. Lv, F.; Wang, J.; Wu, Y.; Chen, H.; Shen, X., Knockdown of MMP12 inhibits the growth and invasion of lung adenocarcinoma cells. *International journal of immunopathology and pharmacology* 2015, 28, 77-84.
87. Heller, T.; Hennecke, M.; Baumann, U.; Gessner, J. E.; zu Vilsendorf, A. M.; Baensch, M.; Boulay, F.; Kola, A.; Klos, A.; Bautsch, W., Selection of a C5a receptor antagonist from phage libraries attenuating the inflammatory response in immune complex disease and ischemia/reperfusion injury. *The Journal of Immunology* 1999, 163, 985-994.
88. Choudhry, V.; Zhang, M.-Y.; Sidorov, I. A.; Louis, J. M.; Harris, I.; Dimitrov, A. S.; Bouma, P.; Cham, F.; Choudhary, A.; Rybak, S. M., Cross-reactive HIV-1 neutralizing monoclonal antibodies selected by screening of an immune human phage library against an envelope glycoprotein (gp140)

- isolated from a patient (R2) with broadly HIV-1 neutralizing antibodies. *Virology* 2007, 363, 79-90.
89. Jung, S.; Honegger, A.; PluÈckthun, A., Selection for improved protein stability by phage display<sup>1</sup>. *Journal of molecular biology* 1999, 294, 163-180.
  90. Frenzel, A.; Schirrmann, T.; Hust, M. In *Phage display-derived human antibodies in clinical development and therapy*, MAbs, Taylor & Francis: 2016; pp 1177-1194.
  91. Turner, S. Humira: the highs and lows of the world's best-selling drug. <https://www.pharmaceutical-technology.com/features/humira-abbvie-drug/> (accessed November 12, 2018).
  92. Sharkey, R. M.; Goldenberg, D. M., Cancer radioimmunotherapy. *Immunotherapy* 2011, 3, 349-370.
  93. Larson, S. M.; Carrasquillo, J. A.; Cheung, N.-K. V.; Press, O. W., Radioimmunotherapy of human tumours. *Nature Reviews Cancer* 2015, 15, 347.
  94. Wang, W.; Wang, E.; Balthasar, J., Monoclonal antibody pharmacokinetics and pharmacodynamics. *Clinical Pharmacology & Therapeutics* 2008, 84, 548-558.
  95. Pouget, J.-P.; Navarro-Teulon, I.; Bardiès, M.; Chouin, N.; Cartron, G.; Pèleguin, A.; Azria, D., Clinical radioimmunotherapy—the role of radiobiology. *Nature reviews Clinical oncology* 2011, 8, 720.
  96. Boswell, C. A.; Brechbiel, M. W., Development of radioimmunotherapeutic

- and diagnostic antibodies: an inside-out view. *Nuclear medicine and biology* 2007, *34*, 757-778.
97. Patra, M.; Zarschler, K.; Pietzsch, H.-J.; Stephan, H.; Gasser, G., New insights into the pretargeting approach to image and treat tumours. *Chemical Society Reviews* 2016, *45*, 6415-6431.
98. Goldenberg, D. M.; Sharkey, R. M.; Paganelli, G.; Barbet, J.; Chatal, J.-F., Antibody pretargeting advances cancer radioimmunodetection and radioimmunotherapy. *Journal of Clinical Oncology* 2006, *24*, 816.
99. Stickney, D. R.; Anderson, L. D.; Slater, J. B.; Ahlem, C. N.; Kirk, G. A.; Schweighardt, S. A.; Frincke, J. M., Bifunctional antibody: a binary radiopharmaceutical delivery system for imaging colorectal carcinoma. *Cancer research* 1991, *51*, 6650-6655.
100. Kalofonos, H.; Rusckowski, M.; Siebecker, D.; Sivolapenko, G.; Snook, D.; Lavender, J.; Epenetos, A.; Hnatowich, D., Imaging of tumor in patients with indium-111-labeled biotin and streptavidin-conjugated antibodies: preliminary communication. *Journal of nuclear medicine: official publication, Society of Nuclear Medicine* 1990, *31*, 1791-1796.
101. Weiden, P. L.; Breitz, H. B.; Press, O.; Appelbaum, J. W.; Bryan, J. K.; Gaffigan, S.; Stone, D.; Axworthy, D.; Fisher, D.; Reno, J., Pretargeted radioimmunotherapy (PRIT™) for treatment of non-Hodgkin's lymphoma (NHL): initial phase I/II study results. *Cancer biotherapy & radiopharmaceuticals* 2000, *15*, 15-29.
102. Liu, G.; Dou, S.; Liu, Y.; Wang, Y.; Rusckowski, M.; Hnatowich, D. J., 90Y

- labeled phosphorodiamidate morpholino oligomer for pretargeting radiotherapy. *Bioconjugate chemistry* 2011, 22, 2539-2545.
103. Bagshawe, K. D., Antibody-directed enzyme prodrug therapy (ADEPT) for cancer. *Expert review of anticancer therapy* 2006, 6, 1421-1431.
104. Sletten, E. M.; Bertozzi, C. R., Bioorthogonal chemistry: fishing for selectivity in a sea of functionality. *Angewandte Chemie International Edition* 2009, 48, 6974-6998.
105. Rossin, R.; Lappchen, T.; van den Bosch, S. M.; Laforest, R.; Robillard, M. S., Diels-Alder reaction for tumor pretargeting: in vivo chemistry can boost tumor radiation dose compared with directly labeled antibody. *J Nucl Med* 2013, 54, 1989-1995.
106. Rossin, R.; van den Bosch, S. M.; ten Hoeve, W.; Carvelli, M.; Versteegen, R. M.; Lub, J.; Robillard, M. S., Highly reactive trans-cyclooctene tags with improved stability for Diels–Alder chemistry in living systems. *Bioconjugate chemistry* 2013, 24, 1210-1217.
107. Rossin, R.; van Duijnhoven, S. M.; Lappchen, T.; van den Bosch, S. M.; Robillard, M. S., Trans-Cyclooctene tag with improved properties for tumor pretargeting with the Diels–Alder reaction. *Molecular pharmaceuticals* 2014, 11, 3090-3096.
108. Houghton, J. L.; Zeglis, B. M.; Abdel-Atti, D.; Sawada, R.; Scholz, W. W.; Lewis, J. S., Pretargeted immuno-PET of pancreatic cancer: overcoming circulating antigen and internalized antibody to reduce radiation doses. *Journal of nuclear medicine: official publication, Society of Nuclear*

*Medicine* 2016, 57, 453.

109. Gulston, M.; de Lara, C.; Jenner, T.; Davis, E.; O'Neill, P., Processing of clustered DNA damage generates additional double-strand breaks in mammalian cells post-irradiation. *Nucleic acids research* 2004, 32, 1602-1609.
110. Yong, K. J.; Milenic, D. E.; Baidoo, K. E.; Brechbiel, M. W., <sup>212</sup>Pb-Radioimmunotherapy induces G2 cell cycle arrest and delays DNA damage repair in tumor xenografts in a model for disseminated intraperitoneal disease. *Molecular cancer therapeutics* 2012, molcanther. 0671.2011.
111. Yong, K.; Brechbiel, M. W., Towards translation of <sup>212</sup>Pb as a clinical therapeutic; getting the lead in! *Dalton Transactions* 2011, 40, 6068-6076.
112. Milenic, D. E.; Garmestani, K.; Brady, E. D.; Albert, P. S.; Ma, D.; Abdulla, A.; Brechbiel, M. W.,  $\alpha$ -Particle radioimmunotherapy of disseminated peritoneal disease using a <sup>212</sup>Pb-labeled radioimmunoconjugate targeting HER2. *Cancer biotherapy & radiopharmaceuticals* 2005, 20, 557-568.
113. Horak, E.; Hartmann, F.; Garmestani, K.; Wu, C.; Brechbiel, M.; Gansow, O. A.; Landolfi, N. F.; Waldmann, T. A., Radioimmunotherapy targeting of HER2/neu oncoprotein on ovarian tumor using lead-212-DOTA-AEI. *Journal of Nuclear Medicine* 1997, 38, 1944-1950.
114. Price, E. W.; Orvig, C., Matching chelators to radiometals for radiopharmaceuticals. *Chemical Society Reviews* 2014, 43, 260-290.
115. Mirzadeh, S.; Kumar, K.; Gansow, O. A., The chemical fate of <sup>212</sup>Pb-DOTA formed by  $\beta$ -decay of <sup>212</sup>Pb (DOTA) 2. *Radiochimica Acta* 1993, 60, 1-10.

116. Beatty, B. G.; Kuhn, J. A.; Edmond Hui, T.; Fisher, D. R.; Williams, L. E.; David Beatty, J., Application of the cross-organ beta dose method for tissue dosimetry in tumor-bearing mice treated with a  $^{90}\text{Y}$ -labeled immunoconjugate. *Cancer* 1994, 73, 958-965.
117. Howell, R. W.; Goddu, S. M.; Narra, V. R.; Fisher, D. R.; Schenter, R. E.; Rao, D. V., Radiotoxicity of gadolinium-148 and radium-223 in mouse testes: relative biological effectiveness of alpha-particle emitters in vivo. *Radiation research* 1997, 147, 342-348.
118. Shen, S.; Forero, A.; LoBuglio, A. F.; Breitz, H.; Khazaeli, M.; Fisher, D. R.; Wang, W.; Meredith, R. F., Patient-specific dosimetry of pretargeted radioimmunotherapy using CC49 fusion protein in patients with gastrointestinal malignancies. *Journal of Nuclear Medicine* 2005, 46, 642-651.
119. Pagel, J. M.; Kenoyer, A. L.; Bäck, T.; Hamlin, D. K.; Wilbur, D. S.; Fisher, D. R.; Park, S. I.; Frayo, S.; Axtman, A.; Orgun, N., Anti-CD45 pretargeted radioimmunotherapy using bismuth-213: high rates of complete remission and long-term survival in a mouse myeloid leukemia xenograft model. *Blood* 2011, blood-2011-2004-347039.
120. Orozco, J. J.; Bäck, T.; Kenoyer, A.; Balkin, E. R.; Hamlin, D. K.; Wilbur, D. S.; Fisher, D. R.; Frayo, S. L.; Hylarides, M. D.; Green, D. J., Anti-CD45 radioimmunotherapy using  $^{211}\text{At}$  with bone marrow transplantation prolongs survival in a disseminated murine leukemia model. *Blood* 2013, blood-2012-2011-467035.

121. American Cancer Society. *Cancer Facts & Figures 2018*. ; American Cancer Society: 2018.
122. Werb, Z.; Gordon, S., Elastase secretion by stimulated macrophages. Characterization and regulation. *Journal of Experimental Medicine* 1975, *142*, 361-377.
123. Chen, Y. E., MMP-12, an old enzyme plays a new role in the pathogenesis of rheumatoid arthritis? *The American journal of pathology* 2004, *165*, 1069-1070.
124. Gronski, T. J.; Martin, R. L.; Kobayashi, D. K.; Walsh, B. C.; Holman, M. C.; Huber, M.; Van Wart, H. E.; Shapiro, S. D., Hydrolysis of a broad spectrum of extracellular matrix proteins by human macrophage elastase. *Journal of Biological Chemistry* 1997, *272*, 12189-12194.
125. ASHWORTH, J. L.; MURPHY, G.; SHERRATT, M. J.; SHAPIRO, S. D.; SHUTTLEWORTH, C. A.; KIELTY, C. M., Fibrillin degradation by matrix metalloproteinases: implications for connective tissue remodelling. *Biochemical Journal* 1999, *340*, 171-181.
126. Ohbayashi, H., Matrix metalloproteinases in lung diseases. *Current Protein and Peptide Science* 2002, *3*, 409-421.
127. Johnson, J. L.; Devel, L.; Czarny, B.; George, S. J.; Jackson, C. L.; Rogakos, V.; Beau, F.; Yiotakis, A.; Newby, A. C.; Dive, V., A selective matrix metalloproteinase-12 inhibitor retards atherosclerotic plaque development in apolipoprotein E-knockout mice. *Arteriosclerosis, thrombosis, and vascular biology* 2011, *31*, 528-535.

128. Razavian, M.; Bordenave, T.; Georgiadis, D.; Beau, F.; Zhang, J.; Golestani, R.; Toczek, J.; Jung, J.-J.; Ye, Y.; Kim, H.-Y., Optical imaging of MMP-12 active form in inflammation and aneurysm. *Scientific reports* 2016, 6, 38345.
129. Lim, N. H.; Meinjohanns, E.; Bou-Gharios, G.; Gompels, L. L.; Nuti, E.; Rossello, A.; Devel, L.; Dive, V.; Meldal, M.; Nagase, H., In vivo imaging of matrix metalloproteinase 12 and matrix metalloproteinase 13 activities in the mouse model of collagen-induced arthritis. *Arthritis & Rheumatology* 2014, 66, 589-598.
130. Bordenave, T.; Helle, M.; Beau, F.; Georgiadis, D.; Tepshi, L.; Bernes, M.; Ye, Y.; Levenez, L.; Poquet, E.; Nozach, H., Synthesis and in vitro and in vivo evaluation of MMP-12 selective optical probes. *Bioconjugate chemistry* 2016, 27, 2407-2417.
131. Shah, S. A.; Spinale, F. G.; Ikonomidis, J. S.; Stroud, R. E.; Chang, E. I.; Reed, C. E., Differential matrix metalloproteinase levels in adenocarcinoma and squamous cell carcinoma of the lung. *The Journal of thoracic and cardiovascular surgery* 2010, 139, 984-990.
132. Kerkela, E.; Ala-aho, R.; Jeskanen, L.; Rechardt, O.; Grénman, R.; Shapiro, S. D.; Kähäri, V.-M.; Saarialho-Kere, U., Expression of human macrophage metalloelastase (MMP-12) by tumor cells in skin cancer. *Journal of Investigative Dermatology* 2000, 114, 1113-1119.
133. Kerkelä, E.; Ala-aho, R.; Klemi, P.; Grénman, S.; Shapiro, S. D.; Kähäri, V. M.; Saarialho-Kere, U., Metalloelastase (MMP-12) expression by tumour

- cells in squamous cell carcinoma of the vulva correlates with invasiveness, while that by macrophages predicts better outcome. *The Journal of pathology* 2002, 198, 258-269.
134. Hofmann, H.-S.; Hansen, G.; Richter, G.; Taege, C.; Simm, A.; Silber, R.-E.; Burdach, S., Matrix metalloproteinase-12 expression correlates with local recurrence and metastatic disease in non-small cell lung cancer patients. *Clinical Cancer Research* 2005, 11, 1086-1092.
135. Cho, N. H.; Hong, K. P.; Hong, S. H.; Kang, S.; Chung, K. Y.; Cho, S. H., MMP expression profiling in recurred stage IB lung cancer. *Oncogene* 2004, 23, 845.
136. Qu, P.; Du, H.; Wang, X.; Yan, C., Matrix metalloproteinase 12 overexpression in lung epithelial cells plays a key role in emphysema to lung bronchioalveolar adenocarcinoma transition. *Cancer research* 2009, 69, 7252-7261.
137. Yu, M. K.; Park, J.; Jon, S., Targeting strategies for multifunctional nanoparticles in cancer imaging and therapy. *Theranostics* 2012, 2, 3.
138. Byrne, J. D.; Betancourt, T.; Brannon-Peppas, L., Active targeting schemes for nanoparticle systems in cancer therapeutics. *Advanced drug delivery reviews* 2008, 60, 1615-1626.
139. Yao, V. J.; D'angelo, S.; Butler, K. S.; Theron, C.; Smith, T. L.; Marchiò, S.; Gelovani, J. G.; Sidman, R. L.; Dobroff, A. S.; Brinker, C. J., Ligand-targeted theranostic nanomedicines against cancer. *Journal of Controlled Release* 2016, 240, 267-286.

140. Bahrami, B.; Hojjat-Farsangi, M.; Mohammadi, H.; Anvari, E.; Ghalamfarsa, G.; Yousefi, M.; Jadidi-Niaragh, F., Nanoparticles and targeted drug delivery in cancer therapy. *Immunology letters* 2017, *190*, 64-83.
141. Ma, K.; Mendoza, C.; Hanson, M.; Werner-Zwanziger, U.; Zwanziger, J.; Wiesner, U., Control of ultrasmall sub-10 nm ligand-functionalized fluorescent core-shell silica nanoparticle growth in water. *Chemistry of Materials* 2015, *27*, 4119-4133.
142. Ma, K.; Wiesner, U., Modular and Orthogonal Post-Pegylation Surface Modifications by Insertion Enabling Penta-Functional Ultrasmall Organic-Silica Hybrid Nanoparticles. *Chemistry of Materials* 2017, *29*, 6840-6855.
143. Chen, F.; Ma, K.; Madajewski, B.; Zhuang, L.; Zhang, L.; Rickert, K.; Marelli, M.; Yoo, B.; Turker, M. Z.; Overholtzer, M., Ultrasmall targeted nanoparticles with engineered antibody fragments for imaging detection of HER2-overexpressing breast cancer. *Nature communications* 2018, *9*, 4141.
144. Chen, F.; Zhang, X.; Ma, K.; Madajewski, B.; Benezra, M.; Zhang, L.; Phillips, E.; Turker, M. Z.; Gallazzi, F.; Penate-Medina, O., Melanocortin-1 receptor-targeting ultrasmall silica nanoparticles for dual-modality human melanoma imaging. *ACS applied materials & interfaces* 2018, *10*, 4379-4393.
145. Benezra, M.; Penate-Medina, O.; Zanzonico, P. B.; Schaer, D.; Ow, H.; Burns, A.; DeStanchina, E.; Longo, V.; Herz, E.; Iyer, S., Multimodal silica

- nanoparticles are effective cancer-targeted probes in a model of human melanoma. *The Journal of clinical investigation* 2011, 121, 2768-2780.
146. Bradbury, M. S.; Phillips, E.; Montero, P. H.; Cheal, S. M.; Stambuk, H.; Durack, J. C.; Sofocleous, C. T.; Meester, R. J.; Wiesner, U.; Patel, S., Clinically-translated silica nanoparticles as dual-modality cancer-targeted probes for image-guided surgery and interventions. *Integrative Biology* 2013, 5, 74-86.
147. Phillips, E.; Penate-Medina, O.; Zanzonico, P. B.; Carvajal, R. D.; Mohan, P.; Ye, Y.; Humm, J.; Gönen, M.; Kalaigian, H.; Schöder, H., Clinical translation of an ultrasmall inorganic optical-PET imaging nanoparticle probe. *Science translational medicine* 2014, 6, 260ra149-260ra149.
148. David, L.; Nesland, J.; Clausen, H.; Carneiro, F.; Sobrinho-Simoes, M., Simple mucin-type carbohydrate antigens (Tn, sialosyl-Tn and T) in gastric mucosa, carcinomas and metastases. *APMIS. Supplementum* 1992, 27, 162-172.
149. Baldus, S. E.; Zirbes, T. K.; Hanisch, F. G.; Kunze, D.; Shafizadeh, S. T.; Nolden, S.; Mönig, S. P.; Schneider, P. M.; Karsten, U.; Thiele, J., Thomsen-Friedenreich antigen presents as a prognostic factor in colorectal carcinoma: A clinicopathologic study of 264 patients. *Cancer* 2000, 88, 1536-1543.
150. Yu, L.-G., The oncofetal Thomsen–Friedenreich carbohydrate antigen in cancer progression. *Glycoconjugate journal* 2007, 24, 411-420.
151. Almogren, A.; Abdullah, J.; Ghapure, K.; Ferguson, K.; Glinsky, V. V.;

- Rittenhouse-Olson, K., Anti-Thomsen-Friedenreich-Ag (anti-TF-Ag) potential for cancer therapy. *Front Biosci (Schol Ed)* 2012, 4, 840-863.
152. Cazet, A.; Julien, S.; Bobowski, M.; Burchell, J.; Delannoy, P., Tumour-associated carbohydrate antigens in breast cancer. *Breast cancer research* 2010, 12, 204.
153. Glinsky, V. V.; Glinsky, G. V.; Rittenhouse-Olson, K.; Huflejt, M. E.; Glinskii, O. V.; Deutscher, S. L.; Quinn, T. P., The role of Thomsen-Friedenreich antigen in adhesion of human breast and prostate cancer cells to the endothelium. *Cancer research* 2001, 61, 4851-4857.
154. Glinsky, V. V.; Glinsky, G. V.; Glinskii, O. V.; Huxley, V. H.; Turk, J. R.; Mossine, V. V.; Deutscher, S. L.; Pienta, K. J.; Quinn, T. P., Intravascular metastatic cancer cell homotypic aggregation at the sites of primary attachment to the endothelium. *Cancer research* 2003, 63, 3805-3811.
155. Peletskaya, E. N.; Glinsky, V. V.; Glinsky, G. V.; Deutscher, S. L.; Quinn, T. P., Characterization of peptides that bind the tumor-associated Thomsen-Friedenreich antigen selected from bacteriophage display libraries<sup>1</sup>. *Journal of molecular biology* 1997, 270, 374-384.
156. Glinsky, V. V.; Huflejt, M. E.; Glinsky, G. V.; Deutscher, S. L.; Quinn, T. P., Effects of Thomsen-Friedenreich antigen-specific peptide P-30 on  $\beta$ -galactoside-mediated homotypic aggregation and adhesion to the endothelium of MDA-MB-435 human breast carcinoma cells. *Cancer research* 2000, 60, 2584-2588.
157. Landon, L. A.; Peletskaya, E. N.; Glinsky, V. V.; Karasseva, N.; Quinn, T.

- P.; Deutscher, S. L., Combinatorial evolution of high-affinity peptides that bind to the Thomsen-Friedenreich carcinoma antigen. *Journal of protein chemistry* 2003, 22, 193-204.
158. Kumar, S. R.; Gallazzi, F. A.; Quinn, T. P.; Deutscher, S. L., <sup>64</sup>Cu-labeled peptide for PET of breast carcinomas expressing the thomsen-friedenreich carbohydrate antigen. *Journal of Nuclear Medicine* 2011, 52, 1819.
159. Karsten, U.; BUTSCHAK, G.; Cao, Y.; GOLETZ, S.; HANISCH, F.-G., A New Monoclonal Antibody (A78-G/A7) to the Thomsen—Friedenreich Pan-Tumor Antigen. *Hybridoma* 1995, 14, 37-44.
160. Butschak, G.; Karsten, U., Isolation and characterization of Thomsen-Friedenreich-specific antibodies from human serum. *Tumor biology* 2002, 23, 113-122.
161. Dahlenborg, K.; Hultman, L.; Carlsson, R.; Jansson, B., Human monoclonal antibodies specific for the tumour associated Thomsen-Friedenreich antigen. *International journal of cancer* 1997, 70, 63-71.
162. Jain, R. K., Delivery of novel therapeutic agents in tumors: physiological barriers and strategies. *JNCI: Journal of the National Cancer Institute* 1989, 81, 570-576.
163. Rittenhouse-Diakun, K.; Xia, Z.; Pickhardt, D.; Morey, S.; Baek, M.-G.; Roy, R., Development and Characterization of Monoclonal Antibody to T-Antigen:(Gal $\beta$ 1—3GalNAc- $\alpha$ -O). *Hybridoma* 1998, 17, 165-173.
164. Heimburg, J.; Yan, J.; Morey, S.; Glinskii, O. V.; Huxley, V. H.; Wild, L.; Klick, R.; Roy, R.; Glinsky, V. V.; Rittenhouse-Olson, K., Inhibition of

- Spontaneous Breast Cancer Metastasis by Anti—Thomsen-Friedenreich Antigen Monoclonal Antibody JAA-F11. *Neoplasia* 2006, 8, 939-948.
165. Rittenhouse-Olson, K., Therapeutic use of anti-TF-Antigen antibody. Google Patents: 2008.
166. Matsumoto-Takasaki, A.; Horie, J.; Sakai, K.; Furui, Y.; Sato, R.; Kawakami, H.; Toma, K.; Takayanagi, A.; Shimizu, N.; Fujita-Yamaguchi, Y., Isolation and characterization of anti-T-antigen single chain antibodies from a phage library. *Bioscience trends* 2009, 3.
167. Yuasa, N.; Koyama, T.; Subedi, G. P.; Yamaguchi, Y.; Matsushita, M.; Fujita-Yamaguchi, Y., Expression and structural characterization of anti-T-antigen single-chain antibodies (scFvs) and analysis of their binding to T-antigen by surface plasmon resonance and NMR spectroscopy. *The Journal of Biochemistry* 2013, 154, 521-529.
168. Ravn, P.; Danielczyk, A.; Jensen, K. B.; Kristensen, P.; Christensen, P. A.; Larsen, M.; Karsten, U.; Goletz, S., Multivalent scFv display of phagemid repertoires for the selection of carbohydrate-specific antibodies and its application to the Thomsen–Friedenreich antigen. *Journal of molecular biology* 2004, 343, 985-996.
169. Waibel, R.; Alberto, R.; Willuda, J.; Finnern, R.; Schibli, R.; Stichelberger, A.; Egli, A.; Abram, U.; Mach, J.-P.; Plückthun, A., Stable one-step technetium-99m labeling of His-tagged recombinant proteins with a novel Tc (I)–carbonyl complex. *Nature biotechnology* 1999, 17, 897.
170. Badar, A.; Williams, J.; de Rosales, R. T.; Tavaré, R.; Kampmeier, F.;

- Blower, P. J.; Mullen, G. E., Optimising the radiolabelling properties of technetium tricarbonyl and His-tagged proteins. *EJNMMI research* 2014, 4, 14.
171. Novak-Hofer, I.; Waibel, R.; Zimmermann, K.; Grünberg, J.; Chester, K. A.; Murray, A.; Lo, B. K.; Perkins, A. C.; Schubiger, P. A., Radiometal labeling of antibodies and antibody fragments for imaging and therapy. In *Antibody Engineering*, Springer: 2004; pp 481-494.
172. Schneider, D. W.; Heitner, T.; Alicke, B.; Light, D. R.; McLean, K.; Satozawa, N.; Parry, G.; Yoo, J.; Lewis, J. S.; Parry, R., In Vivo Biodistribution, PET Imaging, and Tumor Accumulation of  $^{86}\text{Y}$ - and  $^{111}\text{In}$ -Antimindin/RG-1, Engineered Antibody Fragments in LNCaP Tumor-Bearing Nude Mice. *Journal of nuclear medicine: official publication, Society of Nuclear Medicine* 2009, 50, 435.
173. D'huyvetter, M.; Vincke, C.; Xavier, C.; Aerts, A.; Impens, N.; Baatout, S.; De Raeve, H.; Muyldermans, S.; Caveliers, V.; Devoogdt, N., Targeted radionuclide therapy with A  $^{177}\text{Lu}$ -labeled anti-HER2 nanobody. *Theranostics* 2014, 4, 708.
174. Chatalic, K.; Veldhoven-Zweistra, J.; Bolkestein, M.; Hoeben, S.; Koning, G. A.; Boerman, O. C.; de Jong, M.; van Weerden, W. M., A novel  $^{111}\text{In}$ -labeled anti-prostate-specific membrane antigen nanobody for targeted SPECT/CT imaging of prostate cancer. *J Nucl Med* 2015, 56, 1094-1099.
175. Hofström, C.; Altai, M.; Honarvar, H.; Strand, J.; Malmberg, J.; Hosseinimehr, S. J.; Orlova, A.; Gräslund, T. r.; Tolmachev, V., HAHAAA,

- HEHEHE, HIHIHI, or HKHKHK: influence of position and composition of histidine containing tags on biodistribution of [<sup>99m</sup>Tc (CO)<sub>3</sub>]<sup>+</sup>-labeled affibody molecules. *Journal of medicinal chemistry* 2013, 56, 4966-4974.
176. Tolmachev, V.; Hofström, C.; Malmberg, J.; Ahlgren, S.; Hosseinimehr, S. J.; Sandström, M.; Abrahmsén, L.; Orlova, A.; Gräslund, T. r., HEHEHE-tagged affibody molecule may be purified by IMAC, is conveniently labeled with [<sup>99m</sup>Tc (CO)<sub>3</sub>]<sup>+</sup>, and shows improved biodistribution with reduced hepatic radioactivity accumulation. *Bioconjugate chemistry* 2010, 21, 2013-2022.
177. Elvas, F.; Vangestel, C.; Ropic, S.; Verhaeghe, J.; Gray, B.; Pak, K.; Stroobants, S.; Staelens, S., Characterization of [<sup>99m</sup>Tc] duramycin as a SPECT imaging agent for early assessment of tumor apoptosis. *Molecular Imaging and Biology* 2015, 17, 838-847.
178. Huang, L.; Gainkam, L. O. T.; Caveliers, V.; Vanhove, C.; Keyaerts, M.; De Baetselier, P.; Bossuyt, A.; Revets, H.; Lahoutte, T., SPECT imaging with <sup>99m</sup>Tc-labeled EGFR-specific nanobody for in vivo monitoring of EGFR expression. *Molecular imaging and biology* 2008, 10, 167-175.
179. Behr, T. M.; Sharkey, R. M.; Juweid, M. E.; Blumenthal, R. D.; Dunn, R. M.; Griffiths, G. L.; Bair, H.-J.; Wolf, F. G.; Becker, W. S.; Goldenberg, D. M., Reduction of the renal uptake of radiolabeled monoclonal antibody fragments by cationic amino acids and their derivatives. *Cancer research* 1995, 55, 3825-3834.
180. Barone, R.; Pauwels, S.; De Camps, J.; Krenning, E. P.; Kvols, L. K.;

Smith, M. C.; Bouterfa, H.; Devuyst, O.; Jamar, F., Metabolic effects of amino acid solutions infused for renal protection during therapy with radiolabelled somatostatin analogues. *Nephrology Dialysis Transplantation* 2004, 19, 2275-2281.

181. Pinsky, P. F.; Bellinger, C. R.; Miller Jr, D. P., False-positive screens and lung cancer risk in the National Lung Screening Trial: Implications for shared decision-making. *Journal of medical screening* 2018, 25, 110-112.

## **VITA**

Manankumar Shah was born on April 27, 1988 in Vadodara, India. He is the son of Anilkumar and Darshnaben Shah. He graduated from high school from Bright English Medium High School in 2005. Manankumar attended Sardar Patel University in Vallabh Vidhyanagar in Gujarat province, India and received Bachelor of Pharmacy degree in 2009. Manankumar moved to the United States of America in 2009 to pursue Master of Science (M.S.) in Pharmaceutical Chemistry from New Jersey Institute of Technology, New Jersey. He graduated with M.S. degree in 2011 and worked in industry for two years before starting the Ph.D. program at University of Missouri in 2013. He joined the group of Dr. Thomas Quinn in Biochemistry department in May 2014 and is expected to complete his Ph.D. in Biochemistry in December 2018.